Master's thesis

NTNU
Norwegian University of Science and Technology
Faculty of Natural Sciences
Department of Materials Science and Engineering

Moa Madeleine Fagermo

The Use Of Aluminium in Sustainable Concrete Structures

Master's thesis in Materials Science and Engineering, MTMT

Supervisor: Hans Jørgen Roven

July 2020

NTNU
Norwegian University of
Science and Technology

Moa Madeleine Fagermo

The Use Of Aluminium in Sustainable Concrete Structures

Master's thesis in Materials Science and Engineering, MTMT
Supervisor: Hans Jørgen Roven
July 2020

Norwegian University of Science and Technology
Faculty of Natural Sciences
Department of Materials Science and Engineering

NTNU
Norwegian University of
Science and Technology

Preface

This master's thesis is written at NTNU, Department of Material Science and Engineering, during spring 2020. The thesis is a part of the norwegian research project DARE2C, which is led by Hydro with Norcem, Veidekke, SINTEF and NTNU as partners. Hans Jørgen Roven has been the main supervisor. I hereby declare that this project has been done independently and in accordance with regulations at NTNU.

Moa Madeleine Fagermo
NTNU, Trondheim
July 2020

Acknowledgements

I would like to thank my supervisor Hans Jørgen Roven, and my co-supervisors Trond Furu and Oddvin Reiso, for the guidance and support during this thesis. A special thanks to Harald Justnes, Pål Skaret, Berit Kramer, and the team at SINTEF for their assistance in experimental work. Also, I want to express my gratitude to John Reboli Olsen that helped me dissaemble an engine that, in the end, was not needed.

Finally, I would like thank my boyfriend, family, and friends for the endless support and love they have given me the past five years.

Abstract

This master's thesis is a part of the Norwegian research project DARE2C. By replacing steel reinforcement with aluminium reinforcement, DARE2C wants to develop a new, more durable, and environmentally friendly concrete. This thesis focuses on the bond strength and chemical stability of four different aluminium alloys in concrete: 6082, 5052, Al-9Si-2Cu, and Al-9Si-0.3Mg. In addition, the possibility of using recycled automotive aluminium as reinforcement is investigated.

Chemical stability was investigated through hydrogen gas measurements. The evolution of hydrogen gas indicates corrosion of the aluminium reinforcement. It was found that all of the alloys initially reacted with the concrete, but achieved stability after some time. Heat-treated Al-9Si-0.3Mg resulted in the least hydrogen evolution and 5052 in the most.

Heat-treated 6082 and 5052 had the poorest bond strength and the heat-treated Al-Si-alloys had the best. Visual inspection of the split concrete samples after bond testing revealed pores in the hardened concrete of T6-6082 and 5052. It was assumed that the pores harmed the bond strength and was caused by hydrogen evolution. Two other possible reasons for the difference in bond strength were suggested; (1) difference in coefficient of thermal expansion, and (2) the formation of an expansive reaction product between T6-6082 and concrete.

The bond strength of aluminium was lower than the bond strength of standard steel reinforcement. The best bond strength was achieved by Ø20mm T6-Al-9Si-2Cu with 9.3 MPa, while Ø20mm steel had 13.7 MPa. However, the quality of the Al reinforcement ribs was poorer than the steel ribs, and improving the Al ribs might increase the bond strength to the same level as steel reinforcement.

Based on the bond strength and hydrogen gas results for Al-9Si-2Cu and Al-9Si-0.3Mg, it was concluded that the use of recycled automotive aluminium as reinforcement is promising. However, due to the unpredictable nature of secondary Al-alloys, more research is needed.

Sammendrag

Denne masteroppgaven er en del av det norske forskningsprosjektet DARE2C som er finansiert av Norges forskningsråd. Ved å erstatte stålarmering med aluminiumarmering, ønsker DARE2C å utvikle en ny, mer holbar og miljøvennlig betong. Denne oppgaven fokuserer på den kjemiske stabiliteten og heften av fire aluminiumslegeringer i betong: 6082, 5052, Al-9Si-2Cu, og Al-9Si-0.3Mg. I tillegg utforskes mulighetene for å bruke resirkulert aluminium fra bilindustrien som armering.

Kjemisk stabilitet ble undersøkt gjennom målinger av hydrogengass. Utvikling av hydrogengass er et tegn på at aluminium korroderer. Alle aluminiumslegeringene reagerte med betongen, men oppnådde stabilitet etterhvert. Varmebehandlet Al-9Si-0.3Mg hadde minst hydrogenutvikling og 5052 hadde mest.

Varmebehandlet 6082 og 5052 hadde den dårligste heften og de varmebehandlede Al-Si-legeringene hadde den beste. Betongprøvene ble splittet etter hefttesting, noe som avslørte porer i den herdede betongen til T6-6082 og 5052. Det ble antatt at porene skadet heften og var forårsaket av hydrogenutvikling. To andre mulige grunner for forskjellen i heft ble foreslått; (1) forskjell i termisk utvidelseskoeffisient, og (2) dannelsen av et reaksjonsprodukt mellom T6-6082 og betong.

Heften mellom aluminium og betong var lavere enn heften mellom standard stålarmering og betong. Den beste heften ble oppnådd av Ø20mm T6-Al-9Si-2Cu med 9.3 MPa, mens Ø20mm stål hadde 13.7 MPa. Rillene i aluminiumarmeringen, var mye dårligere enn de i stålarmeringen. Dermed, hvis rillene forbedres kan det være at heften nærmer seg samme heft som stålarmering oppnår.

Basert på heftstyrken og utviklingen av hydrogengass hos Al-9Si-2Cu og Al-9Si-0.3Mg, ble det konkludert med at bruken av resirkulert aluminium fra bilindustrien som armering er lovende. Det er viktig å påpeke at sekundær aluminium er uforutsigbar, og derfor bør flere undersøkelser gjennomføres.

Abbrevations

ASR	Alkali-Silica Reaction
ASTM	American Society for Testing and Materials
DARE2C	Durable Aluminium Reinforced Environmentally-friendly Concrete Construction
EDS	Energy-dispersive X-ray Spectroscopy
GP-zone	Guinier-Preston zone
HV	Vickers Hardness
LOM	Light Optical Microscopy
LVDT	Linear Variable Differential Transformer
NTNU	Norwegian University of Science and Technology
OPC	Ordinary Portland Cement
Rebar	Reinforcement bar for concrete
SCM	Supplementary Cementing Materials
SE	Secondary Electrons
SEM	Scanning Electron Microscopy
SSHT	Solid-Solution Heat Treatment
SSSS	Super Saturated Solid Solution
TEM	Transmission Electron Microscopy
UTS	Ultimate Tensile Strength
wt%	Weight percent
XPS	X-ray Photoelectron Spectroscopy
XRD	X-Ray Diffraction
Ø10	Diameter of 10
Ø20	Diameter of 20

Contents

List of Figures

List of Tables

1 Introduction

Annually, 4.4 billion tons of concrete is produced [1]. The world is dependent on it as a construction material, and the demand continues to increase. Concrete is strong in compression, but weak in tension. Because of this, it is often reinforced with steel. Reinforced concrete is resistant to water, fire, and cyclic loading. As a construction material, it is preferable to steel and wood due to its formability, availability, and low cost.

Concrete production has considerable environmental downsides. Cement production alone is responsible for 8% of the global greenhouse gas emissions. In addition, a huge amount of fresh water is needed for the curing process. Water scarcity is one of the greatest challenges of our time, and this will only get worse as developing countries builds concrete infrastructure.

In recent years, the durability of reinforced concrete has become an issue. Constructions deteriorate much earlier than predicted and large sums of money are spent on repairs. Deterioration is often related to corrosion of the steel reinforcement. The corrosion products of steel cause an expansion of 600% and consequent cracking and spalling.

Changing the reinforcement material to a more corrosion resistant metal is a possible way to increase the durability and sustainability of concrete. This is the goal of the Norwegian research project DARE2C (Durable Aluminium Reinforced Environmentally-friendly Concrete Construction) and they aim to use aluminium as reinforcement. There is just one issue; concrete is very basic and aluminium corrodes in basic environments.

Is there a solution to this corrosion issue? Yes. The DARE2C solution is to replace more than half of the Portland cement with red clay. In this new concrete mix, aluminium appears to be stable. Also, seawater can be used as a hydration agent instead of fresh water. However, primary aluminium production leads to large greenhouse gas emissions. Recycling aluminium cuts the GHG emissions by 95% and should ideally be applied instead. Now, the next question is then: how can we obtain a sufficient amount of recyclable aluminium?

There are numerous sources of aluminium scrap, but one large untapped source is automotive aluminium. Due to climate change, more consumers are turning to environmentally friendly solutions. In Norway, the number of electric cars quintupled between 2015 and 2019 [2]. This entails scrapping of fossil-fueled cars. Aluminium is used in the car body, rims, and large parts of the engine. All of this could be recycled and used as reinforcement. Especially large components, such as the engine block, are suited for recycling.

1.1 Aim of Work

This master's thesis is a part of the DARE2C research project. The aim of the experimental work is twofold: (1) To investigate the performance and durability of aluminium reinforcement and (2) to evaluate the possibility of recycled automotive aluminium as reinforcement.

2 Theory

In this section a summary of relevant theory and literature is presented to give the reader an insight in the background of this master's thesis. Section 2.5.3 and 2.9.1 are based on the authors previous work [3].

2.1 Aluminium Alloys

Aluminium is the second most widely used metal in the world. This is largely due to its low density, high corrosion resistance, high weight-to-strength ratio, and large occurrence. Aluminium alloys are divided into two categories; wrought alloys and cast alloys. These are presented in sections 2.1.1 and 2.1.2.

2.1.1 Wrought Alloys

Wrought alloys are aluminium alloys that are shaped through mechanical processing such as rolling, extrusion, and drawing [4]. These alloys gain their strength by work hardening, solution hardening, and precipitation hardening [5]. The international designation system for aluminium alloys designates four numbers to an alloy. The first number describes the major alloying element, the second number a variation of the alloy, and the third and fourth gives the specific alloy in the system. In this thesis, four alloys from three different alloy systems were used. These alloys are further described in the following sections.

4xxx: Al-Si

The 4xxx aluminium series is alloyed with silicon (up to 12%). The addition of silicon to aluminium is known to increase fluidity. This makes Al-Si alloys popular as cast alloys and they are mostly used for such purposes. Silicon also lowers the coefficient of thermal expansion which decreases shrinkage during solidification [5]. There are no intermetallic compounds between aluminium and silicon. Si is present as primary silicon particles and Si-particles in an aluminium matrix. In wrought form, aluminium-silicon alloys are mainly used as welding rod and for brazing [6]. The Al-Si phase diagram is given in Figure (2.1.1).

The presence of iron and/or sodium is significant for the mechanical properties and microstructure of Al-Si alloys. Adding sodium shifts the eutectic point to ~ 14% and lowers the melting point. Na also works as a grain refiner and leads to smaller, more dispersed silicon particles, resulting in improved mechanical properties. Iron is almost insoluble in Al-Si alloys and occurs as a β-FeSi phase. As long as the concentration of Fe is kept small (< 0.6 wt%), it does not affect the mechanical properties greatly. At higher concentrations, large brittle phases are precipitated during solidification which is detrimental to strength and ductility. The addition of other alloying elements also affects the mechanical properties and structure of the alloy, however, Fe and Na are the most important ones [6].

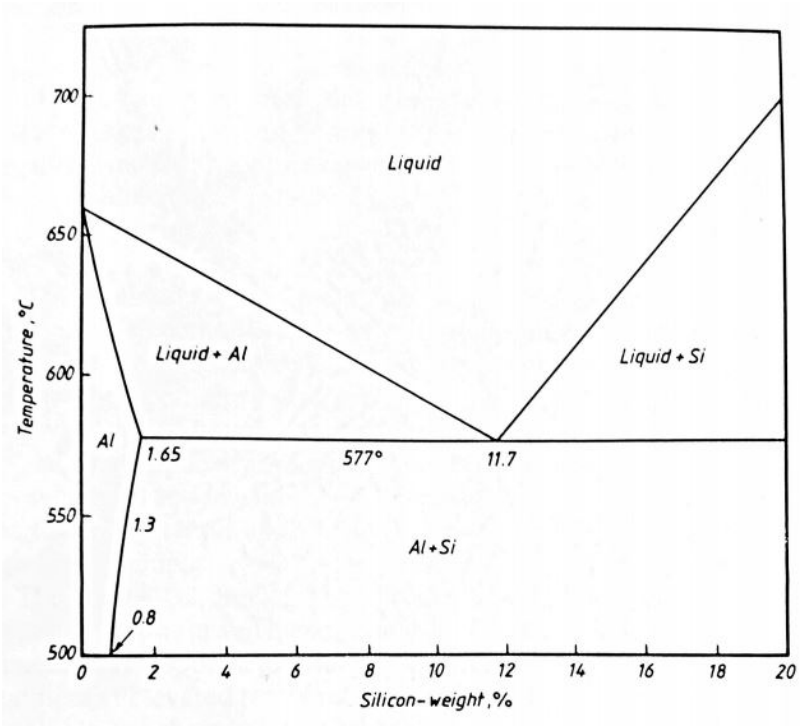

Fig. 2.1.1. Aluminium - silicon phase diagram. The eutectic point is at 11.7 % silicon and the melting temperature is 577°C. From reference [6].

5xxx: Al-Mg

Aluminium alloys with magnesium as their main alloying element are a part of the 5xxx-series. These alloys are known for their high corrosion resistance and weldability, making them desirable in marine and off-shore applications. The high corrosion resistance is caused by a protective Al_2O_3-layer in which magnesium participates. Al-Mg alloys are considered non-heat treatable and obtain their strength from solid solution hardening and strain hardening. The Al-Mg binary phase diagram is given in Figure (2.1.2). As can be seen from this diagram, the solid solubility of Mg in Al increases with temperature and reaches ~ 17 wt% at 450°C. Magnesium has a larger atomic radii than aluminium and, as a solute atom in the Al lattice, restricts the movement of dislocations. This leads to a considerable increase in hardness and strength [7].

At high Mg-concentrations, β-particles precipitate at the grain boundaries. In addition to brittleness, this introduces a potential difference between the grain and grain boundaries. As a result, the material becomes susceptible to inter-granular corrosion and stress corrosion cracking. For this reason, commercial alloys typically contain up to 5% Mg [5, 8]. The best corrosion resistance conditions are when the β-phase is distributed as discrete particles. The addition of Mn and/or Cr is effective in reducing the grain boundary potential which improves the corrosion resistance. However, this is at the expense of some ductility and formability. In wrought Al-Mg alloys, sodium should be avoided. This is an impurity that forms isolated pores that cause embrittlement and cracks [6].

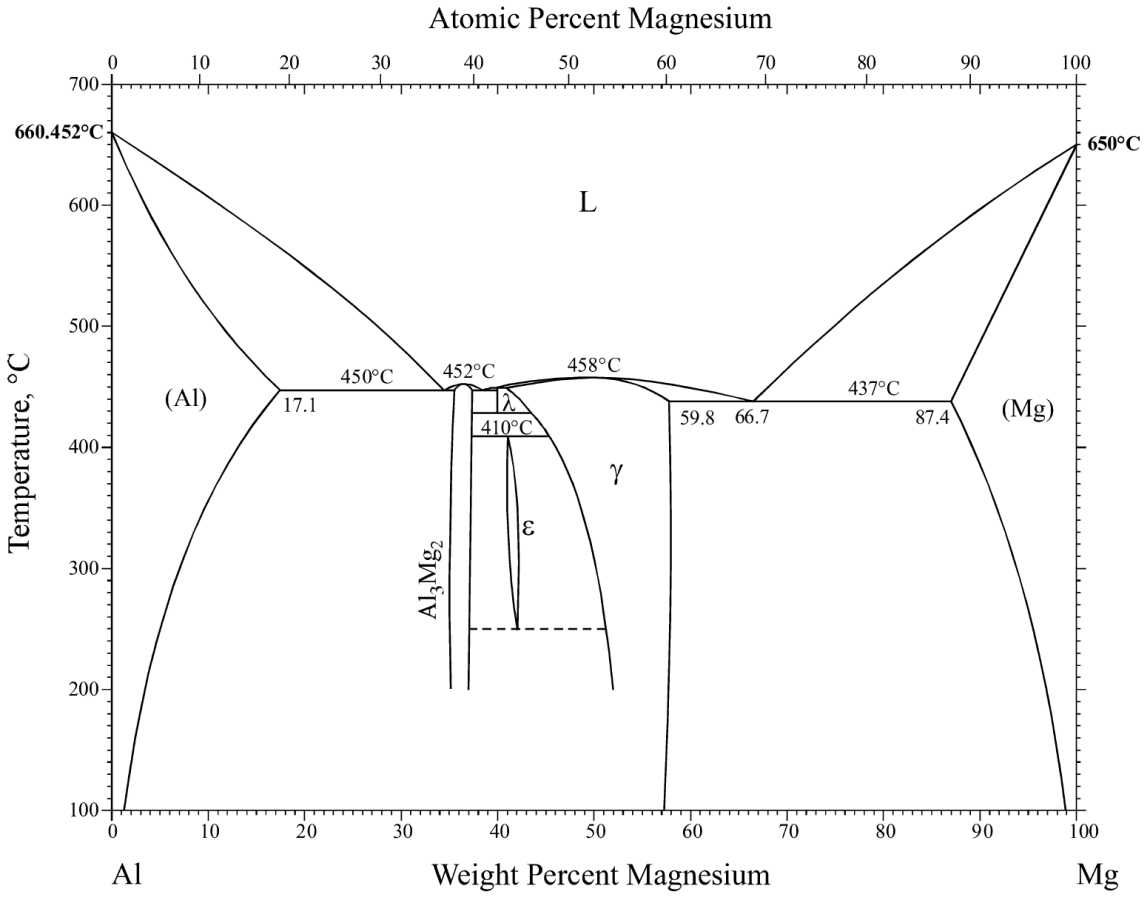

Fig. 2.1.2. Aluminium - magnesium phase diagram. From reference [9].

6xxx: Al-Mg-Si

The 6xxx-series has high corrosion resistance, medium strength, is highly formable, heat treatable, and weldable [10]. It is also one of the most commonly used aluminium alloys, particularly as extruded products. Half of all produced aluminium profiles in the world are from the 6xxx-series [5]. The main alloying elements are Mg and Si, which form Mg_2Si, the major strength contributing phase. Mn and Cr are added in small amounts as grain refinement agents. Cu can be added to increase strength, but more than 0.5 wt% decreases the corrosion resistance [5]. Overall, the Al-Mg-Si-system has low alloy content and because of this, good electrical conductivity.

Al-Mg-Si-alloys gain their strength from the precipitation of Mg_2Si. The pseudo-binary Al-Mg_2Si phase diagram is given in Figure (2.1.3). The maximum solubility of Mg_2Si is ~1.85 wt% and the eutectic point is at 595°C. Excess Si can be added to promote the precipitation of this phase, however, too much Si can cause embrittlement. The precipitation mechanism and sequence will be further discussed in section 2.5.3.

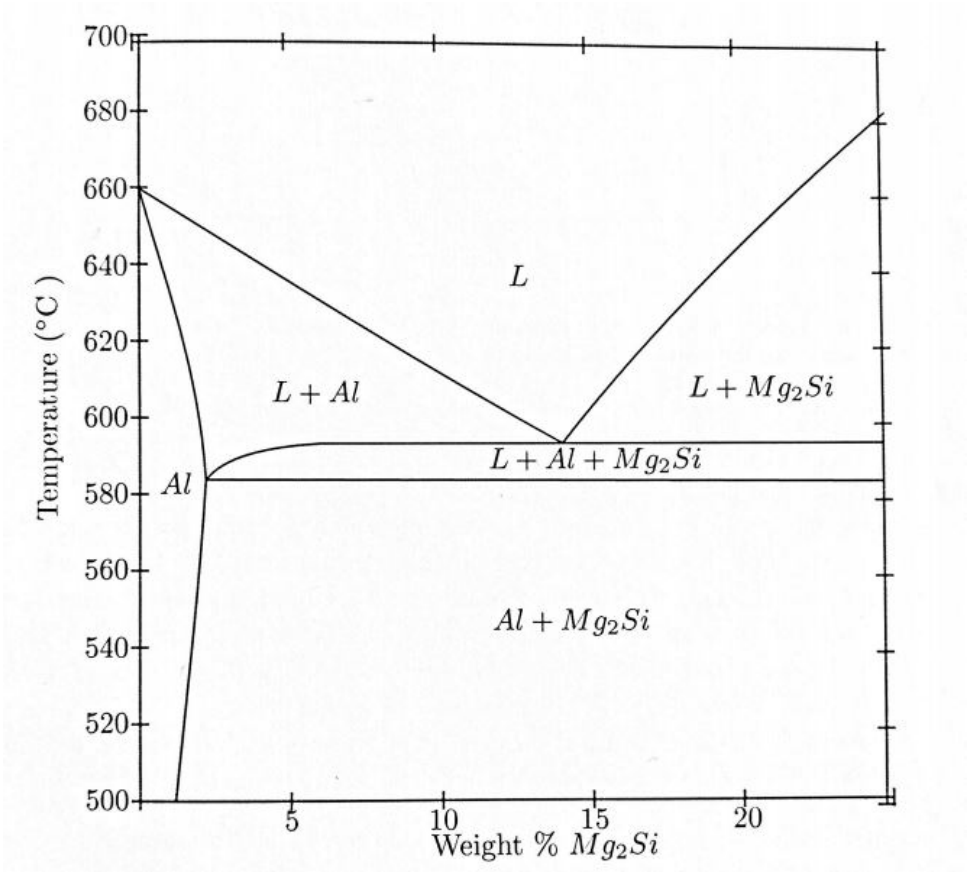

Fig. 2.1.3. Aluminium - Mg_2Si phase diagram. From reference [10].

2.1.2 Cast Alloys

As the name suggests, aluminium cast alloys are shaped by casting. The most commonly used processes are permanent mold casting, sand casting, and die casting. Cast alloys obtain their strength by heat treatment and alloying elements, and because of this they are often highly alloyed [5]. The designation system for cast alloys is similar to that of wrought alloys, but the last digit (decimal) is either a 0 or 1, describing casting or ingot. Automotive aluminium alloys are often cast alloys and a typical automotive alloy is described below.

3xx.x: Al-Si-Cu-Mg

Al-Si-Cu-Mg-alloys are a part of the 3xx.x-series. Silicon is the most important alloying element in cast alloy systems. As mentioned, silicon increases the fluidity of aluminium and decreases shrinkage during solidification. These are properties that are very beneficial for the casting process. Copper is known to increase the strength of Al-Si-alloys, and the combination of low fluidity and strength makes Al-Si-Cu-alloys especially desirable. Magnesium also contributes to strength through the precipitation of Mg_2Si. The precipitation mechanism and sequence in Al-Si-Cu-Mg alloys are further discussed in section 2.5.3.

Alloys with silicon content > 10% lower the thermal expansion coefficient to a level that is highly beneficial for high-temperature applications. Hypereutectic alloys (>12.6 wt% Si, see Figure (2.1.1)) precipitates primary Si-crystals which are good for wear resistance. These properties make these alloys excellent for automotive use. However, with increasing Si content the alloys display less ductility and less machinability. Because of this, hypoeutectic alloys are most often used as they show a better combination of strength/ductility.

2.1.3 Recycling and Sustainability

The world we live in has a limited amount of resources and it is, therefore, important to spend them wisely for the sake of our generation and coming generations. Sustainability is a concept founded on this idea and is often described as follows:

> Sustainable development is development that meets the needs of the present without compromising the ability of future generations to meet their own needs. (Brundtland, 1987)

Sustainability is divided into three groups; economic, environmental, and social. This section focuses on the environmental sustainability of aluminium.

Emission of greenhouse gases (GHG) is one of the big concerns regarding the environment. These gases (mainly carbon dioxide (CO_2), water vapour (H_2O), methane (CH_4), and nitrous oxide (N_2O)) cause what is referred to as the *greenhouse effect*. This is a natural process that causes the earth's temperature to rise. Since the industrial revolution, human activities have caused this process to rapidly accelerate. In 2013 the Intergovernmental Panel on Climate Change (IPCC) released the fifth assessment report [11]. This report assessed the causes of sea-level rise and estimated the cumulative CO_2-emissions since pre-industrial times up to now. It found that the earth's temperature had increased by 0.85 °C in this time. IPCC strongly recommended that the increase was kept below 2°C to avoid serious ecological and economical threats. However, there is some evidence that we may have reached or passed a "point of no return", i.e. a point where we already have cause irreversible changes in major ecosystems and planetary climate systems.

Primary aluminium is produced by electrolysis of alumina. The raw material for aluminium production is bauxite which consists of aluminium oxide, water, and other impurities. Bauxite undergoes an alumina refining process, often referred to as the Bayer's process, to remove water and impurities. In this process, bauxite is crushed, heated, and mixed with NaOH. The resulting mixture is filtered and cooled so that alumina crystallizes. To remove all water residue, the filtered mixture is then heated in a rotary kiln (~ 1200 °C). After the Bayer's process, alumina is converted to aluminium metal through the Hall–Héroult process [12]. Here, alumina is dissolved in a cryolite bath (Na_3AlF_6) in a steel container with a carbon cathode and anode. As an electric current is applied to the electrolyte, liquid aluminium is formed at the cathode, and CO_2-gas is formed at the anode. The simplified total reaction is given in equation (2.1.1).

$$2Al_2O_3 + 3C \rightarrow 4Al + 3CO_2 \tag{2.1.1}$$

The entire primary aluminium manufacturing process from the mining of bauxite to the casting of ingots releases approximately 6.7 ton CO_2 per ton aluminium [13]. Depending on the production method (blast furnace or electric arc furnace), steel manufacturing releases 0.7 - 1.8 ton CO_2 per ton steel. A pie chart of aluminium GHG-emission from 2015 is given in Figure (2.1.4). The electrolysis process is indirectly responsible for more than a third of the emissions; smelters consume a lot of electrical energy. The environmental impact of aluminium will heavily depend on the energy source (hydro power/ fossil fuel power) and the amount of ton CO_2 per ton Al will vary between smelting plants.

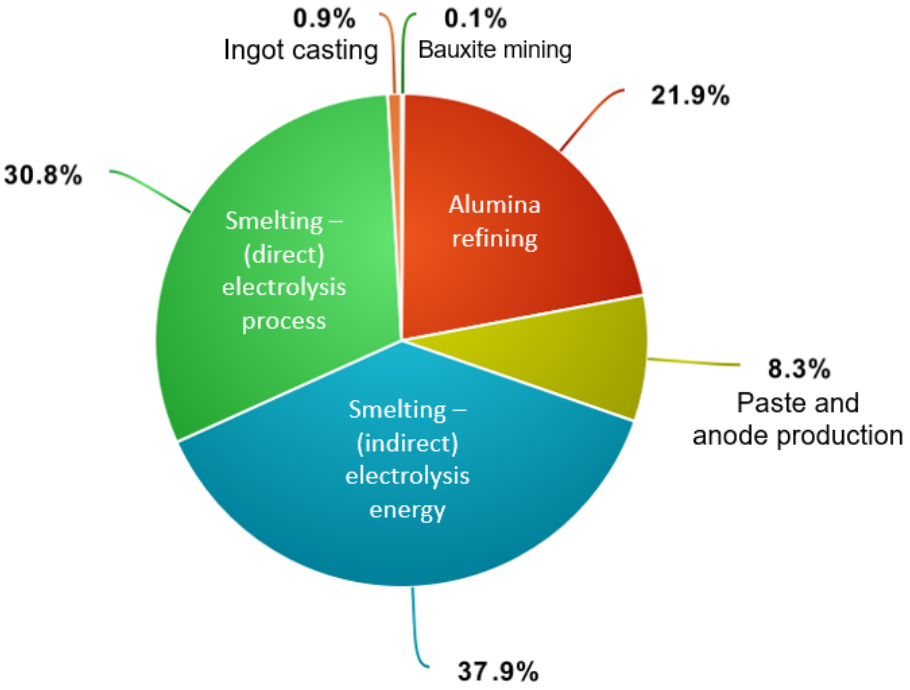

Fig. 2.1.4. Aluminium GHG emissions, 2015. The data was obtained from reference [14] and the figure was made by present author.

One of the greatest perks of aluminium is that it is infinitely recyclable (theoretically). Recycling of aluminium, also called secondary aluminium production, only requires 5% of the energy needed to produce primary aluminium and only emits 5% as much GHG. This results in a significant reduction in GHG-emissions. It is also more sustainable since it does not spend any more raw material. Even though aluminium oxide is one of the most common minerals in the earth's crust, there is still a limit to our aluminium deposits. In 2009, 32 % of aluminium products came from recycled aluminium scrap [15].

Aluminium scrap can be obtained from various sources. Recycling large pieces of scrap with similar composition will lead to more predictable properties. Automotive aluminium

is therefore a great source of recyclable material. In the period 2015-2019 more than 680 000 cars were scrapped in Norway and during the same period, the number of electric cars increased by more than 500% [2]. It is fair to assume that there is a connection between the two numbers and that the number of scrapped fossil-fueled cars will continue to increase. Finding a purpose for all this material is one of the motivations for this thesis.

Most commonly, aluminium is recycled through ram extrusion [16]. In this process, the metal is first sorted by alloying content before the different categories are melted into billets. The billets are then extruded into the desired shape. There will be some unrecoverable material loss due to oxidation during the melting step. Ram extrusion requires large amounts of energy due to high temperatures during melting and extrusion. In recent years, the interest in solid-state recycling of aluminium has increased. Solid-state recycling is a process where recycling occurs below the solidus temperature of the metal. Consequently, it demands less energy. A study by J.R. Duflou et al. (2015) investigated the environmental impact of different aluminium recycling methods [17]. It was found that solid-state recycling through screw extrusion had the smallest impact. The results of the study are summarized in Figure (2.1.5). The impact is measured in mPt which is a measurement of annual environmental load.

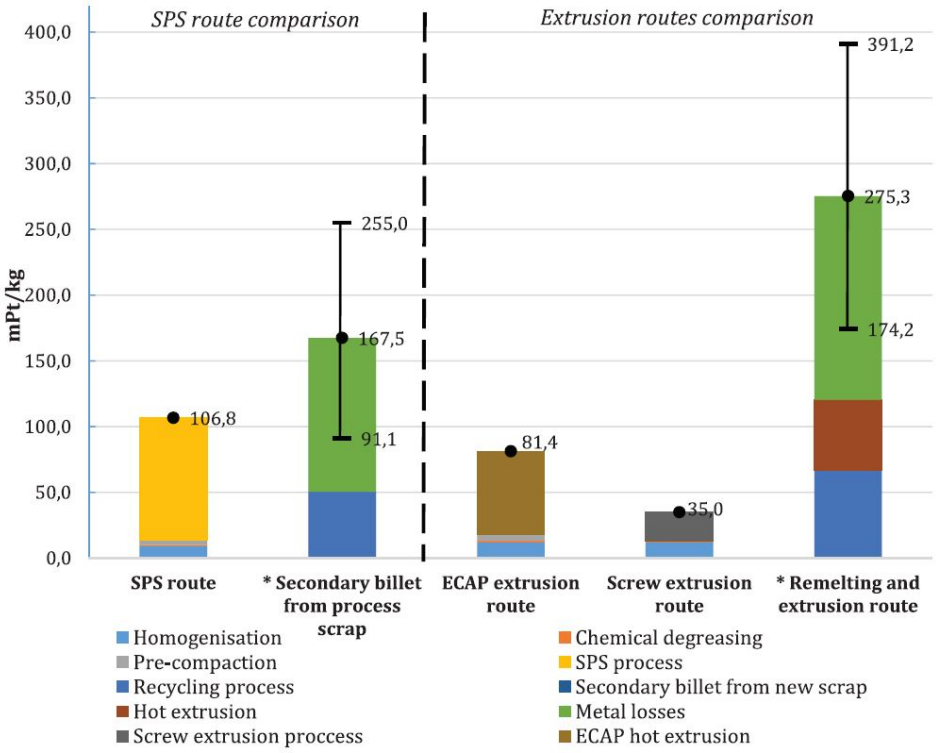

Fig. 2.1.5. Comparison of environmental impact contribution of different recycling routes. Figure from reference [17].

2.2 Concrete

2.2.1 Constituents

Concrete is a composite material consisting of aggregate, cement, and admixtures. Typically, concrete contains 80% aggregate, 12% cement, and 8% mixing water (by mass). It is mostly used as a construction material and is preferable to steel and wood due to its resistance to water, its formability, availability, and the inexpensive nature of the main components (aggregate, water, and cement). Other properties such as fire resistance and resistance to cyclic load make it especially better than steel [18]. The properties of aggregate, cement, and admixtures are further described below.

Aggregate is a granular material and the matrix of the material. Aggregate is bonded by a cement paste. Sand, gravel, and crushed stone are examples of different types of aggregate. These are classified as *fine* or *coarse* aggregate. Fine aggregate contains particles finer than 4.75 mm, while coarse aggregate contains particles larger than 4.75 mm (up to about 50 mm). There are no complex chemical reactions between aggregate and water, and it has historically been referred to as an inert filler. In recent years, this has been questioned as it turns out aggregate has a significant influence on important mechanical properties such as E-modulus and freeze-thaw resistance [18].

Cement is a fine and pulverized material that, on its own, is not a binding component. Cement can be either hydraulic or non-hydraulic. Hydraulic cement develops binding properties and becomes water-resistant due to chemical reactions between the dry ingredients and water. In this group, the most common cement type, Portland cement, is found. The manufacturing and chemistry of hydraulic cement will be closer described in the consecutive section. Non-hydraulic cement is not a common type of cement and will therefore not be discussed further.

Admixtures are added to the concrete mix to give it certain properties that aggregate and cement can not provide. These are added as powders or fluids. Examples of admixtures are air-entraining agents, superplasticizers, and corrosion inhibitors. Two special groups of admixtures are *mineral admixtures* and *supplementary cementing materials (SCM)*. These have pozzolanic properties. Pozzolanic materials react with the calcium hydroxide in cement and, with water, obtain cementitious properties [19]. Such materials can be used to improve the properties of the hardened concrete (mineral admixtures) and/or work as a replacement for Portland cement (SCMs). Silica fume, fly ash, and furnace slag are three important pozzolanic materials.

2.2.2 Manufacturing and Chemistry of Cement

To understand the reactions between cement and aluminium reinforcement, one must understand the basic chemistry of cement. The main focus will be on the chemistry of Portland cement, as it is the most common cement and the one used in this thesis. The manufacturing process of cement is summarized in Figure (2.2.1).

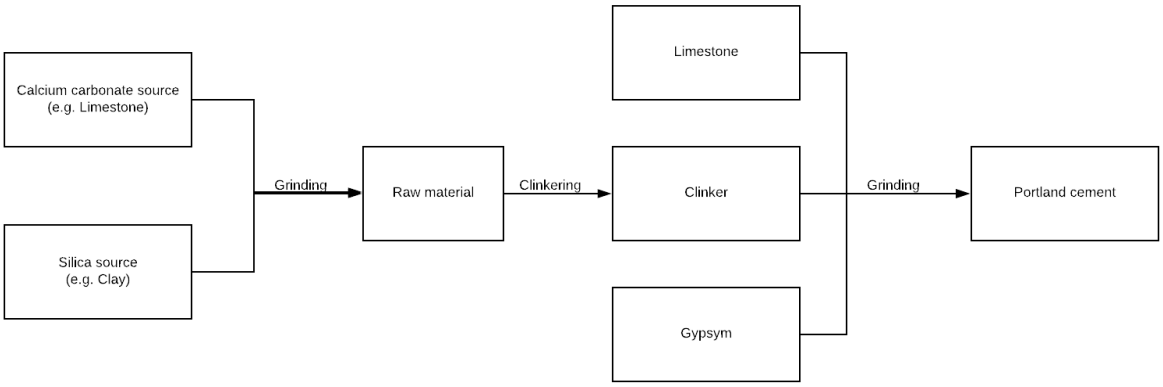

Fig. 2.2.1. Schematic chart of the Portland cement manufacturing process. Based on reference [18] and [20].

The primary components in Portland cement are calcium silicates [18]. Therefore, the raw material needs to contain calcium and silica. Materials such as limestone, chalk, and marl are naturally occurring sources of calcium carbonate, where limestone is the most used one. Different types of clays are often used as silica sources instead of, e.g, quartz which does not react well with limestone. Clay also contains alumina, iron oxide, and alkalies. This raw material, as well as other ingredients such as iron ore and fly ash, are ground together by ball milling or roll milling [20]. This step is to ensure homogeneous distribution of the material before heat treatment. The material is ground down to a particle size of < 75 μm.

In a rotary kiln, the ground raw material is heated to approximately 1400 °C. The elements form clinker, which is a substance in the form of grey balls. These are approximately the size of marbles. The reactions in the kiln can be summarized as described by equations (2.2.1) to (2.2.3).

$$\text{Limestone} \rightarrow CaO + CO_2 \tag{2.2.1}$$

$$\text{Clay} \rightarrow SiO_2 + Al_2O_3 + Fe_2O_3 \tag{2.2.2}$$

$$\text{Clay + limestone} \rightarrow \begin{cases} 3CaO \cdot SiO_2 \\ 2CaO \cdot SiO_2 \\ 3CaO \cdot Al_2O_3 \\ 4CaO \cdot Al_2O_3 \cdot Fe_2O_3 \end{cases} \tag{2.2.3}$$

The final manufacturing step of Portland cement is to pulverize the clinker to an average particle size of 10-15 μm [18]. In this step, limestone and gypsum are added as well. Gypsum is added to slow down the $3CaO \cdot Al_2O_3$-reaction. Without gypsum, the cement would set almost immediately after water is added.

Ordinary Portland Cement (OPC) consists of different oxides that are all abbreviated for simplicity. The oxides, compounds, and their abbreviations are given in Table (2.2.1). The

different compounds in OPC react differently during the hydration process. Hydration of aluminates and silicates are the two most important. As mentioned, gypsum is added to slow down the reaction rate of C_3A. This is because aluminates react quickly and the solidification and stiffening of the cement are largely determined by the hydration of aluminates. The hydration of silicates dominates the hardening process of cement, i.e. the strength development [18].

Tab. 2.2.1. Oxide and compounds in Portland cement. From reference [18].

Oxide	Abbreviation	Compound	Abbreviation
CaO	C	$3CaO{\cdot}SiO_2$	C_3S
SiO_2	S	$2CaO{\cdot}SiO_2$	C_2S
Al_2O_3	A	$3Cao{\cdot}Al_2O_3$	C_3A
Fe_2O_3	F	$4CaO{\cdot}Al_2O_3{\cdot}Fe_2O_3$	C_4AF
MgO	M	$4CaO{\cdot}3Al_2O_3{\cdot}SO_3$	$C_4A_3\overline{S}$
SO_3	$\overline{S}$	$3Cao{\cdot}2SiO_2{\cdot}3H_2O$	$C_3S_2H_3$
H_2O	H	$CaSO_4{\cdot}2H_2O$	$C\overline{S}H_2$

2.2.3 Durability

The UK reports that they spend £40 billion per year on the repair and maintenance of infrastructure, while the US estimates that they need $3 trillion over 5 years to upgrade their infrastructure to an acceptable state [21]. Finding new and more durable concrete designs and solutions is therefore important to lower costs and, as will be discussed later, improve the sustainability of concrete. The integrity of a concrete structure can be damaged by different sources of deterioration. Some common sources are:

- Alkali-Aggregate reaction
- Sulphate attack
- Corrosion of reinforcement
- Frost action

Deterioration can also be caused by overloading the structure, earthquake, fire, and other natural disasters.

Most aggregate is inert and does not react with cement paste. However, some aggregate contains active silica which is not stable at high pH. Silica reacts with hydroxide in concrete and forms Si-OH. This compound acts as a base and reacts with alkali (Na, Ca, K), creating a gel. The gel causes expansive pressure that could lead to cracks in concrete. This is referred to as an alkali-aggregate reaction or alkali-silica reaction (ASR). For ASR to occur sufficient humidity, reactive silica, and sufficient alkali is required [22].

The ASR effect can be mitigated by the addition of supplementary cementing materials (SCMs) [23]. By replacing OPC with SCMs, the alkali content can be lowered until it no longer is a threat to the integrity of the concrete structure. As well as lowering the alkali content, the addition of SCMs also results in less expansive alkali-silicate products [18]. ASR could also be

mitigated by using non-reactive aggregate, but due to the shortage of quality aggregate, the addition of SCMs is more preferable.

Expansive pressure that leads to cracking can also be caused by the formation of ettringite during a sulphate attack. Sulphate attack in concrete occurs in two different forms; (1) external attack or (2) internal attack. In an external attack, sulphates from the surroundings (soil, sulphate in water, etc) permeate the concrete and forms ettringite. The internal attack is also referred to as delayed ettringite formation (DEF). This is caused by the decomposition of ettringite at high temperature (>70°C) and the reformation after cooling [24].

Concrete is strong under compressive stress, but not under tensile stress. Because of this, steel reinforcement is added. In some conditions, the reinforcement can corrode. The corrosion products cause an expansion of up to 6x, leading to crack formation in the cement. The cracking causes spalling of the concrete and the steel bar will eventually be exposed, as shown in Figure (2.2.2). Also, corrosion of the reinforcement entails a decrease in steel cross-section, i.e. a decrease in tensile strength.

Fig. 2.2.2. Exposed corroded steel reinforcement. Image was taken on Pier 2 in Narvik, 2018.

At high pH-values, the corrosion rate of steel is low. This is due to a protective oxide layer that is formed as iron reacts with OH^--ions. If the oxide layer is broken, active corrosion will initiate. This is referred to as depassivation and is mainly caused by one of two reasons; (1) acidification of the water in the cement paste or (2) breakdown due to aggressive ions.

Hardened concrete contains pores that are, to a varying degree, filled with water. The pore water usually holds the same pH as the rest of the cement paste, but it can be acidified through *carbonation*. Carbonation is the process where CO_2 in the air is absorbed into the concrete and dissolved in the pore water. CO_2 is acidic and causes the pH in the concrete to decrease. The pH of sound concrete is 13-14 and the pH of carbonated concrete can be as low as 8. At such low pH-values, the passive oxide layer on the steel reinforcement breaks down and active corrosion initiates [25].

Concrete is often used in structures close to or submerged in seawater, i.e. in the presence of chloride ions. Chloride ions attack the protective oxide film on the reinforcement bars and lead to the depassivation of the reinforcement. As the oxide film is destroyed by the chloride ions, two reactions occur. Equation (2.2.4) describes the chloride attack of the exposed steel beams, and equation (2.2.5) describes the reconstruction of the oxide film. If the concentration of chlorides is larger than the concentration of hydroxides, active corrosion will take place.

$$Fe + 2Cl^- \rightarrow Fe^{2+} + 2Cl^- + 2e^- \tag{2.2.4}$$

$$Fe + 2OH^- \rightarrow Fe(OH)_2 + 2e^- \tag{2.2.5}$$

$$\tag{2.2.6}$$

The ingress of chlorides is dependent on the exposure conditions. In wet concrete, the chlorides move by diffusion, which is a rather slow process. If the concrete is dry, capillary forces play a part as well as diffusion. The movement caused by capillary forces is much quicker than diffusion. Therefore, an environment with chlorides and many wetting/drying-cycles is the most detrimental to concrete.

Deterioration due to frost action is caused by the expansion of water as it freezes. The most common form of frost damage is *cracking and spalling*, which is caused by repeated freezing/thaw cycles. Other forms are *scaling* and *D-cracking*. Concrete is susceptible to frost action if the capillary saturation level is > 91.7%. Water expands 9% as it freezes creating hydraulic pressure that forces water into smaller pores and causing cracking. The hydraulic pressure (and cracking) can be minimized by air entrainment. Air entrainment is a process in which small air bubbles are introduced in the cement matrix. These air bubbles work as a pressure relief when water freezes [24]. Figure (2.2.3) illustrates the formation of ice in capillary voids vs. air voids.

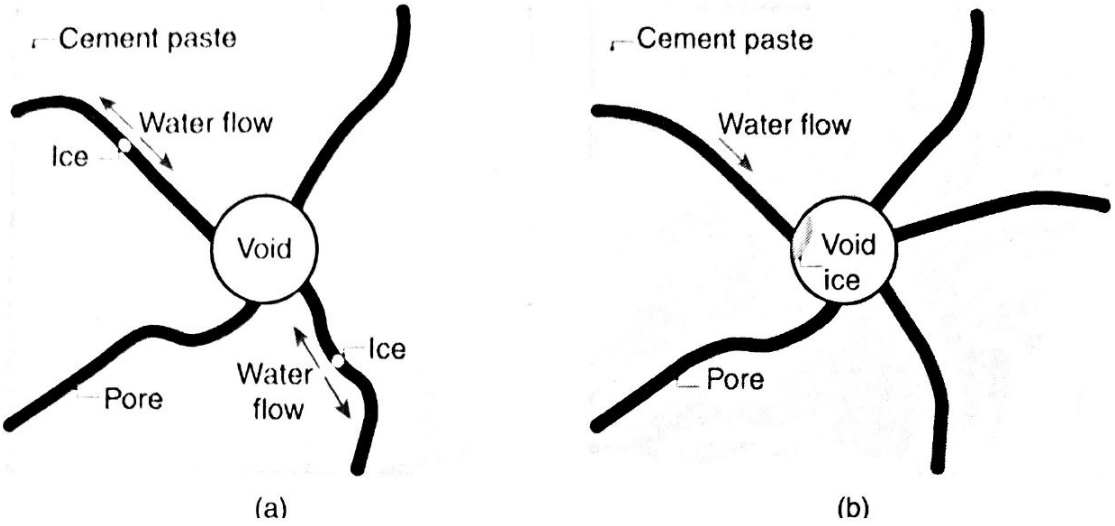

Fig. 2.2.3. Diagram of ice forming in (a) capillary voids and (b) air voids. Image from reference [18].

2.2.4 Sustainability

Concrete is, by far, the most widely used construction material in the world. The demand for concrete is ever increasing and will only continue to increase. The possible environmental impact of concrete is huge and decreasing it should be in focus.

As was discussed in Section 2.1.3, the emission of greenhouse gases is one of the biggest environmental concerns. In concrete manufacturing, GHG-emissions from cement production are the largest portion of the total GHG-emissions. In 2016, cement production alone was responsible for 8% of the CO_2-emissions worldwide which is equivalent of 2.2 billion tonnes CO_2[26]. Reducing the cement amount in a concrete mix will significantly reduce the GHG-emissions. Cement can be replaced by different supplementary cementitious materials (SCMs).

Manufacturing of concrete does not only emit large amounts of CO_2, but it also demands large quantities of water. 70% of the world's surface is water, but only 3% of this is fresh water. The chloride ions in seawater make seawater useless as a hydration agent for cement, due to the threat chloride ions pose to steel reinforcement. This means that freshwater, our only source of drinking water, has to be used as a hydration agent. Water scarcity was named one of the greatest challenges of our time by the World Economic Forum in 2019 [27]. It is predicted that 2/3 of the worlds population will live in a water-stressed contry by 2025.

How durable a concrete structure determines how big of an impact it will have on the environment. Naturally, a structure that lasts 50 years will have less of an environmental impact than a structure that only lasts 10 years. Durability has always been a focus for researchers, scientists, and engineers, but in recent years the importance of durability has become more and more evident as relatively new structures deteriorate much earlier than expected [18]. Corrosion of

reinforcing steel, and consequent cracking, is the most common and most dangerous form of deterioration. In some cases, concrete structures can be build without reinforcement, but for most applications reinforcement is needed to carry tensile loads. Therefore, we must look at the reinforcement material and ask; how can we make the reinforcement more corrosion resistant?

Certain types of steel are corrosion resistant (i.e. stainless steel), however, these are expensive and the costs are too great to use them in large constructions. Aluminium is a possible reinforcement material, as will be discussed further in Section 2.4.

2.3 Corrosion of Aluminium

Aluminium has good corrosion resistance in slightly acidic and neutral environments ($4 < pH < 9$), as can be read from Figure (2.3.1). This is caused by the near insoluble aluminium oxide layer that forms when Al is exposed to oxygen. If this layer is damaged, it will immediately reseal itself and the corrosion resistance is maintained. Outside of the pH-range 4-9, in alkaline and highly acidic environments, the aluminium oxide layer is dissolved and the aluminium is left exposed to further corrosion attacks.

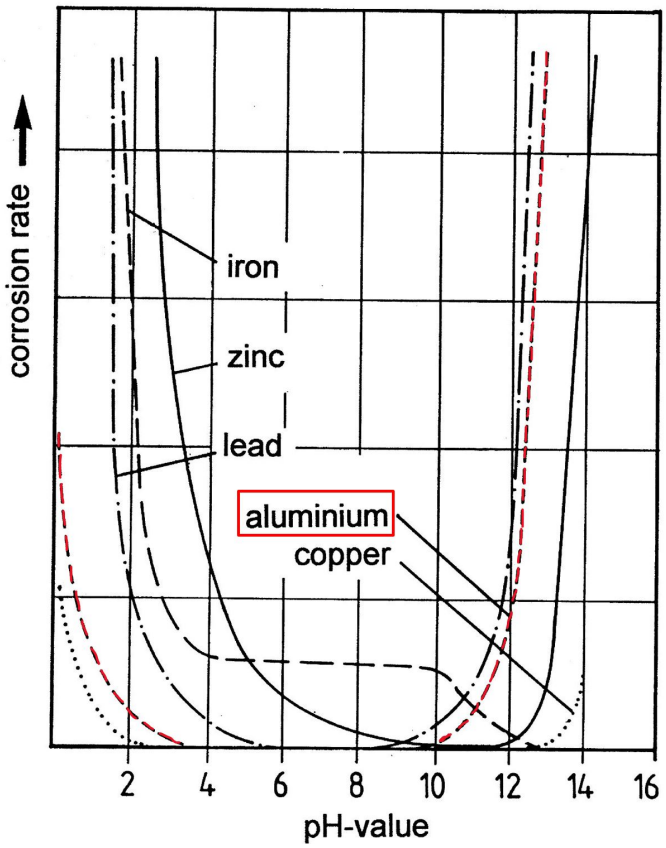

Fig. 2.3.1. Corrosion rate of metals with increasing pH. Aluminium is highlighted. Figure from reference [28].

As well as being dependent on the pH, the corrosion resistance of aluminium is dependent on the composition of the alloy. Alloys containing magnesium are known to have higher corrosion resistance. This is because magnesium participates in the protective Al_2O_3 layer, forming a thicker and more stable oxide layer [5]. Some alloys, on the other hand, cause lower corrosion resistance. This is especially true of alloys containing Cu and/or Pb. These alloys are susceptible to microgalvanic corrosion. Galvanic corrosion occurs when a metal is in electrochemical contact with a metal which is less/more noble. The difference in nobility creates a galvanic coupling where the less noble metal corrodes. In seawater and corrosive environments, Cu/Pb is more noble than Al. Microgalvanic corrosion is believed to be the mechanism behind corrosion phenomena such as intergranular corrosion, pitting corrosion, and filiform corrosion [29].

2.3.1 Aluminium in Contact with Cement

Hardened ordinary Portland cement (OPC) has a pH of around 13. Regarding corrosion, this is an ideal environment for steel, but not for aluminium. The aluminium oxide layer reacts with OH^--ions in the cement as described in equation (2.3.1) and the exposed aluminium further corrodes as described in equation (2.3.2).

$$Al_2O_3 + 2OH^- + 3H_2O \rightarrow 2Al(OH)_4^- \tag{2.3.1}$$

$$Al + 2OH^- + 2H_2O \rightarrow Al(OH)_4^- + H_2 \tag{2.3.2}$$

As can be seen from the latter equation, hydrogen gas is released as a consequence of aluminium corroding. The evolution of hydrogen gas creates a porous region around the metal. Further, strätlingite is formed as $Al(OH)_4^-$ reacts with silicates and calcium hydroxide. Ultimately, $Al(OH)_4^-$ decomposes and releases OH^- which leads to more corrosion. The corrosion process of aluminium in cement is schematically illustrated in Figure (2.3.2).

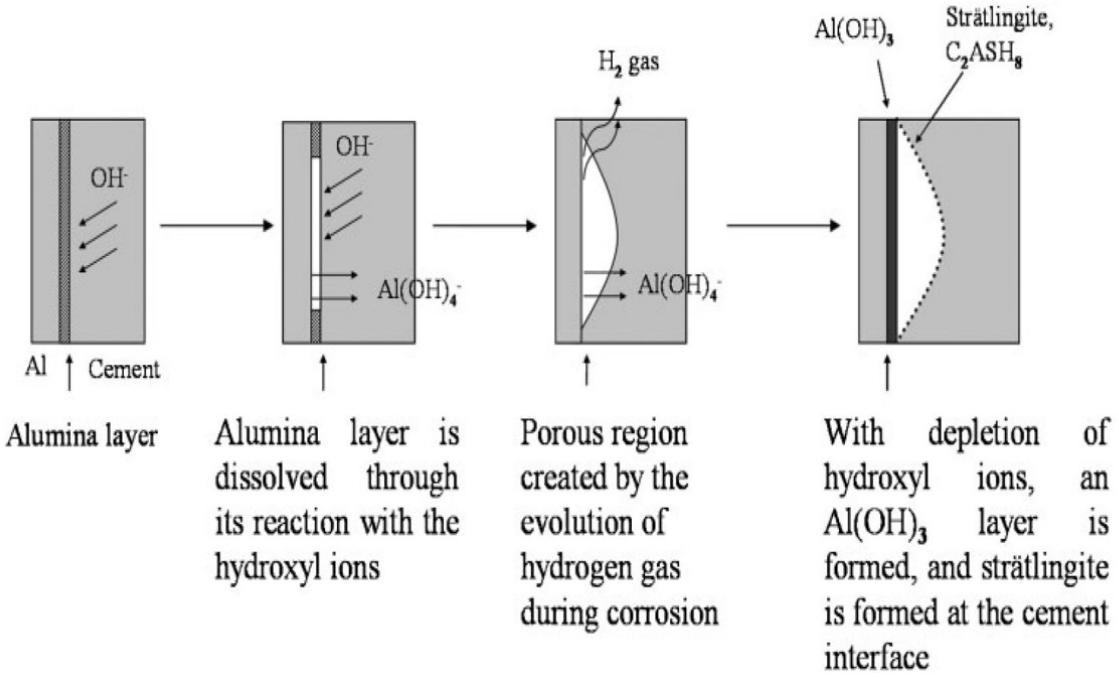

Fig. 2.3.2. Schematic illustration of mechanism of aluminium corrosion in cement. Figure from reference [28].

2.4 Development of Novel Cement Compatible with Aluminium

The norwegian research project DARE2C (Durable Aluminum Reinforced Environmentally-friendly Concrete Construction) aims to develop a reinforced concrete that is more sustainable by using aluminium as reinforcement. Originally, the project wanted to decrease the pH of concrete as a way of creating an environment where aluminium is stable. > 50% of Portland cement was therefore replaced with red clay. The pH did not decrease significantly, however, aluminium appeared to be stable in the environment [30]. Figure (2.4.1) shows the interfacial zone between two different concrete mixes and aluminium reinforcement. As can be seen from this figure, the mix with 100% Portland cement results in more pores and corrosion product (white substance). The pores were caused by H_2-gas which is a by-product of Al-corrosion [30]. According to the leading researcher in the project, Harald Justnes, the stability of the aluminium is a result of fewer active OH^--ions in the hardened concrete. Instead of attacking the metal, the hydroxide groups are bound in other compounds. Later studies also concluded that with the new concrete mix, aluminium could be used as reinforcement [31, 32, 33].

(a) Reference concrete mix with 100% Portland cement.

(b) DARE2C mix with 50% calcined clay.

Fig. 2.4.1. Comparison of two concrete mixes reinforced with aluminium. Images from reference [30].

There are multiple reasons why the DARE2C solution is more sustainable. The first one is the reduction in GHG-emissions. Since >50% of Portland cement is replaced by an SCM, CO_2-emissions due to cement production are smaller. In addition, by using recycled aluminium as reinforcement, the emissions from metal production will be lower. Replacing OPC with SCMs will also have the following effects:

- Less risk of aggregate-alkali reaction
- Less risk of sulphate attack

Consequently, the durability increases.

As mentioned in Section 2.2.3, carbonation is a process where CO_2 is absorbed into the concrete structure. The DARE2C concrete mix results in a more open structure and therefore more CO_2 will be absorbed. When concrete is reinforced with steel, carbonation should be avoided. However, with aluminium reinforcement, carbonation is not a threat to the structural integrity of the rebars. More CO_2 absorption reduces the carbon footprint of concrete.

Aluminium is generally more corrosion resistant than common carbon steel. By lowering the corrosion of the reinforcement, the lifetime of a concrete structure will be significantly increased. Improved corrosion resistance will also decrease the need for large cover thickness, meaning that less concrete (and cement) is needed.

Unlike steel, chlorides do not harm the passive oxide layer on aluminium. Multiple aluminium alloys are commonly used in marine applications due to this resistance to aggressive chloride ions. Using aluminium as reinforcement could, therefore, help solve the challenge

of water scarcity. Not only will aluminium reinforcement increase the durability of concrete structures, but the industry will be able to use seawater as a hydration agent.

2.5 Microstructural Evolution

This section briefly introduces the concepts of microstructural evolution in the processing of metals and the precipitation behavior of three different aluminium alloys. The section 2.5.3 is based on previous work by the author [3].

2.5.1 Recovery and Recrystallization

During mechanical processing such as extrusion and rolling, the free energy of crystalline materials is raised because of the presence of dislocations and interfaces. The increase in free energy causes the material to become thermodynamically unstable. At low temperatures, the energy will be lowered by slow atomistic operations. However, by annealing the material at high temperatures, the energy necessary for the restoration process, *recovery*, to initiate is supplied. In this process, the energy is lowered by rearranging and annihilating dislocations [34].

As long as annealing continues, recovery will be replaced by *recrystallization*. During recrystallization, the old deformed grains will be replaced by new dislocation-free grains. The new grains will grow until all old grains are consumed. The recovery and recrystallization process is illustrated in Figure (2.5.1)

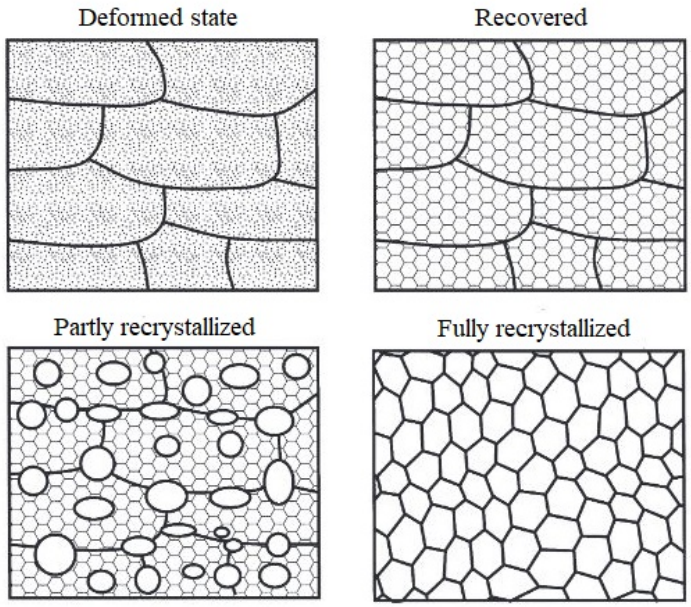

Fig. 2.5.1. Schematic diagram of recovery and recrystallization process. Figure adapted from reference [34].

2.5.2 Grain and Particle Coarsening

After the recrystallization process is complete, the microstructure will still be thermodynamically unstable. This is because grain boundaries are unstable as well. Grain boundaries are annihilated by *grain growth*. For significant grain growth to occur, the temperature has to be sufficiently high. Grain growth is also dependent on particle distribution. Particles exert pressure on the grain boundaries which slows down grain growth.

Controlling the grain size is important for multiple reasons. The Hall-Petch equation provides a relation between the yield strength and grain size. The relation is inversely proportional, meaning that the yield strength decreases as the grain size increases. The Hall-Petch relation is given in equation (2.5.1).

$$\sigma_y = \sigma_0 + k_y d^{-1/2} \tag{2.5.1}$$

where σ_y is the yield strength, d is the average grain diameter, and σ_0 and k_y are material constants.

Particle growth, also known as particle coarsening, will also occur at high temperatures. Unlike grain growth, particle growth is also limited by diffusion. The diffusion coefficient of a species can be described by equation (2.5.2). The particle size will heavily influence the mechanical properties of a metal. For example, large brittle particles will create a brittle material.

$$D = D_0 exp\left(-\frac{Q_d}{RT}\right) \tag{2.5.2}$$

Where D_0 is the temperature-independent preexponential, Q_d is the activation energy, R is the gas constant, and T is absolute temperature [35].

2.5.3 Precipitation Hardening

Precipitation hardening is an important hardening mechanism in aluminium. In this process, the mechanical properties are improved by the formation of small particles of a second phase in the metal matrix. The particles, called precipitates, are introduced through heat treatment. Two heat treatments are necessary to achieve precipitation hardening: (1) solid solution heat treatment and (2) precipitation heat treatment (aging). In the former, the alloy is heated into a single-phase region and kept until all other phases are completely dissolved. The alloy is then rapidly cooled or quenched so a single-phase solid solution supersaturated with atoms is achieved. In this state, the alloy is soft and weak. The alloy is then precipitation heat treated. First, it is heated to a two-phase region. At this temperature, the diffusion rate is sufficient enough for precipitate phases to form. The composition and amount of precipitates are dependent on the composition of the alloy. As the annealing continues over time, the strength/hardness will reach a peak, known as the peak-age condition. After this stage, the

strength/hardness will decrease again, called over-aging. A schematic of the heat treatments is given in Figure (2.5.2).

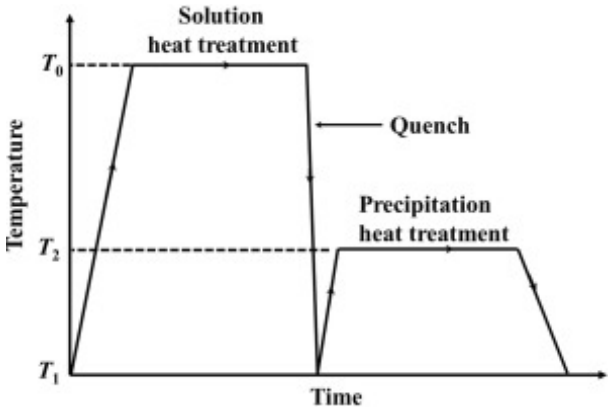

Fig. 2.5.2. Schematic temperature-time plot of solution and precipitation heat treatment. Figure from reference [35].

Precipitation in Wrought Al-Mg-Si Alloys

Al-Mg-Si wrought alloys have medium strength and are therefore routinely heat treated to T6 condition (peak-age condition). The precipitation mechanism in Al-Mg-Si-alloys have been widely studied and multiple precipitation sequences have been suggested. However, it is generally agreed that the sequence is as follows:

$$\text{SSSS} \rightarrow \text{Mg/Si atom clusters} \rightarrow \text{Guinier-Preston(GP) zones} \rightarrow \beta'' \rightarrow \beta' \rightarrow \beta(Mg_2Si) \quad (2.5.3)$$

Guinier-Preston zones are thin phases that occupy space in the Al-lattice. The movement of dislocations are hindered by the stress field caused by these phases, resulting in an increase of strength.

There are some controversy regarding the sequence. One of them being the initial precipitation sequence following the supersaturated solid solution (SSSS). In a study conducted by G. A. Edwards et.al., it was suggested that SSSS is followed by the formation of three atom clusters: (1) Si, (2) Mg, and (3) Mg/Si co-clusters. The clusters are not formed simultaneously. It is believed that Si and Mg clusters are formed first, followed by the formation of Mg/Si co-clusters [36].

At peak-aged condition, rod-shaped β''-precipitates are predominant in the microstructure, indicating that this phase is the main strength contributor in Al-Mg-Si-alloys [36]. Figure (2.5.3) shows a TEM micrograph of Al6061 after 4h of artificial aging at 175°C. This is near the peak-aged condition for this alloy and the rod-shapes precipitates are β''.

Some studies claim that the structure of the β''-phase is two units of Mg_5Si_6 in a C-centred monoclinic atomic cell [37, 38]. However, atom probe tomography experiments conducted by H.S. Hasting et.al. suggest that the precipitates also contain Al [39]. The study proposes

the replacement of Si atoms with Al, and the formation of an $Mg_5Al_2Si_4$-structure. It was concluded that the composition of the β''-precipitates could be both $Mg_5Al_2Si_4$ and Mg_5Si_6 since it is reasonable to believe that the β'' structure can have multiple compositions.

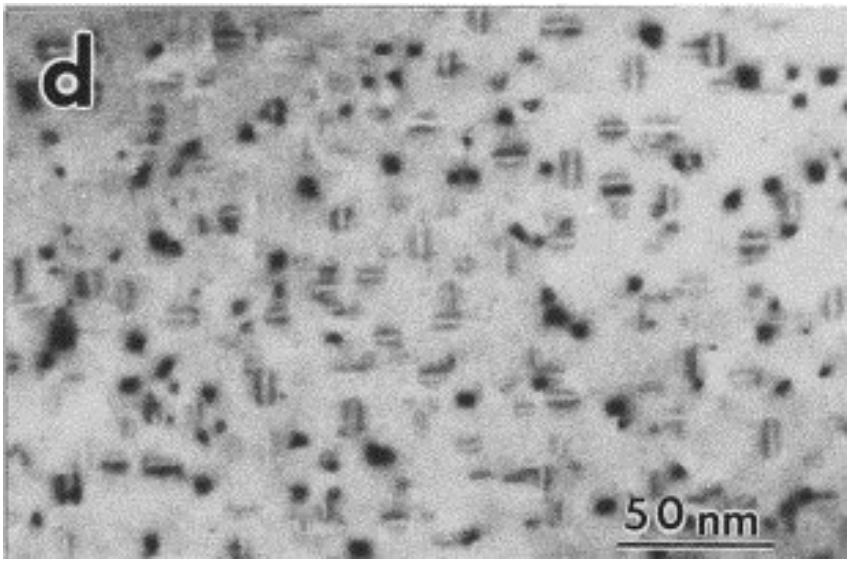

Fig. 2.5.3. TEM micrograph of Al6061 after 4 h of artificial aging at 175°C. Rod-shaped β''-precipitates are predominant in the microstructure. Figure from reference [36].

Precipitation in Al-Si Alloys

Precipitation in Al-Si alloys is, in this section, divided into Al-Si-Mg and Al-Si-Mg-Cu. In Al-Si-Mg alloys, Mg is added to promote precipitation hardening behavior. The precipitation sequence in these alloys are similar to the one described in equation (2.5.3) [40].

Adding copper to Al-Si-Mg alloys is known to significantly increase the strength. The phases present at peak-strength will be dependent on the thermal history and composition of the alloy. Examples of phases that are often present in this condition are $\theta'(Al_2Cu)$, β'' (Mg_2Si), and Q" ($Al_5Mg_8Si_6Cu_2$) [41]. The precipitation sequences for θ'' and β'' are given in equation (2.5.4) and (2.5.3), respectively.

$$SSSS \rightarrow GP \rightarrow \theta'' \rightarrow \theta' \rightarrow \theta(Al_2Cu) \tag{2.5.4}$$

Y.J. Li et al. (2006) reported that θ'-Al_2Cu does not precipitate if wt% Cu is less than 1.0 - 1.5 [42]. Instead, it influences the strength by increasing the density of precipitated β''. Another study by G. Wang et al. (2007) agreed that θ'-Al_2Cu will only precipitate if wt% Cu > 1 [43].

The amount of iron present in both Al-Si-Mg and Al-Si-Mg-Cu alloys is critical. If Fe is present, intermetallic and Fe-rich phases will also precipitate during heat treatment. The composition of these are dependent on the Fe- and Mg-content. In alloys with Mg > 0.4 wt%, π-AlFeMgSi precpipitates, while in alloys with ≤ 0.4wt% a mixture of the π - phase and

β-Al_5FeSi precipitates. Both of these phases are strong and will contribute to strength in the alloy. In addition, the iron β-phase serves as a nucleation site for $CuAl_2$. However, iron precipitates are brittle and decreases the ductility of the alloy [40, 44]. A.M. Samuel et. al (2000) reported that if iron content is higher than 1.5wt%, the alloy should be scrapped or diluted with an alloy with lower Fe-content [45]. This can be seen as a threshold value where the disadvantages of Fe exceeds the benefits.

2.6 Thermomechanical Processes

2.6.1 Extrusion

Extrusion, also called ram extrusion, is a thermomechanical process where a fixed cross-sectional profile is created by forcing material through a die. It is a commonly used method of producing long profiles, both solid and hollow. The die decides the geometry of the cross-section and numerous complex cross-sections are available. The most common extrusion method is known as *forward extrusion* or *direct extrusion*. In this process, the ram moves in the same direction as the material being extruded. Other common extrusion processes include backward (indirect) extrusion, in which the ram moves in the opposite direction of the material, and impact extrusion [46]. The three extrusion methods are illustrated in Figure (2.6.1).

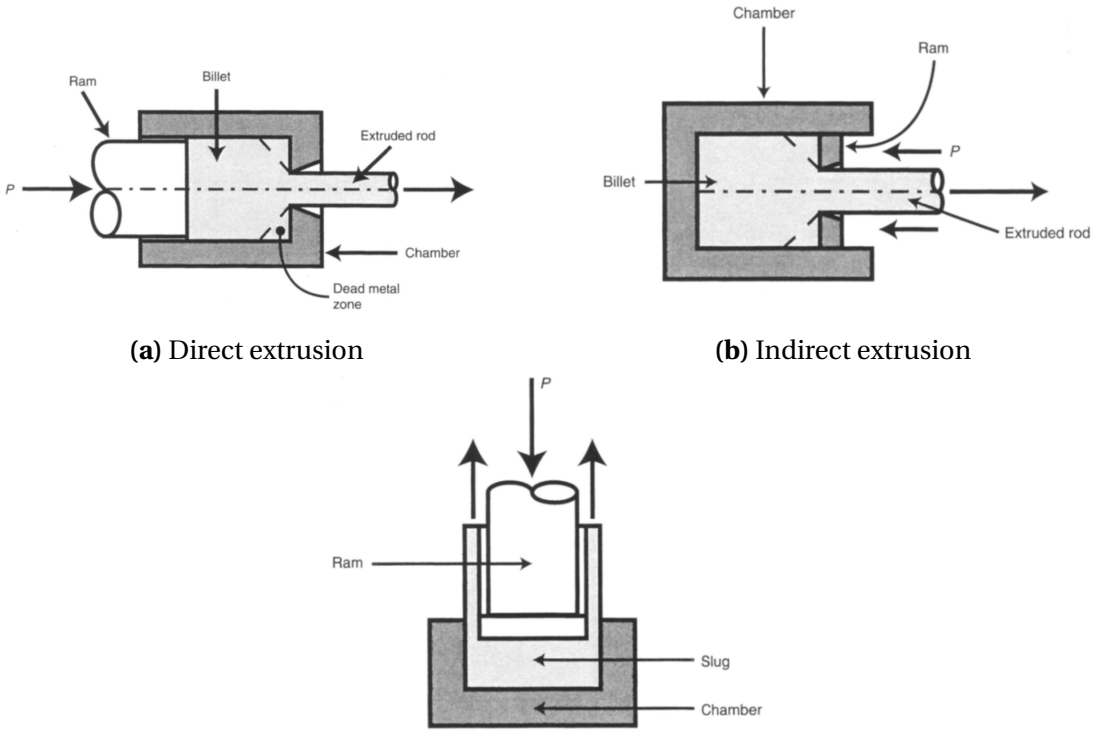

(a) Direct extrusion

(b) Indirect extrusion

(c) Impact extrusion

Fig. 2.6.1. Schematic illustration of different extrusion processes. Images from reference [46].

Before extrusion, the material is usually melted and cast into a billet. The billet is cut into appropriate lengths and homogenized. Homogenizing is a heat treatment that affects the heterogeneity of the cast microstructure. During homogenization, second-phase particles are dissolved and microsegregation is reduced. This improves the extrudability and workability of the alloy [47]. Extrusion is often performed at elevated temperatures, known as hot extrusion. Meaning that the billet temperature is high, generally >60% of the melting temperature of the metal [48]. Hot extrusion significantly decreases the deformation resistance and flow stress. When extruding Al-Mg-Si alloys, the billet is often overheated. This is done to dissolve Mg_2Si-particles and increase the extrudability. Overheating of billets also leads to higher possible extrusion speeds, better mechanical properties, and surface finish [49].

A great deal of deformation heat is generated as a billet is extruded. The heat is heavily influenced by the extrusion ratio and extrusion speed. The extrusion ratio is defined as the relationship between the initial cross-section and the cross-section of the finished product. This relation is given in equation (2.6.1). A high extrusion ratio entails more deformation and thus heat generation. This is not necessarily an issue as long as the extrusion speed is controlled. If the extrusion speed is high, the heat generated will not be able to dissipate quickly enough and local melting can occur. On the other hand, to slow speed reduces productivity and could lead to an increase in needed ram pressure due to the cooling of the billet.

$$R = \frac{\text{Cross-sectional area of billet}}{\text{Cross-sectional area of finished product}} = \frac{A_i}{A_f} \tag{2.6.1}$$

Plastic deformation in extrusion will always be largest at the edges, as illustrated in Figure (2.6.2). Because of this, a thin layer on the surface achieves a finer recrystallized grain size. The thickness of the recrystallized layer depends on the extrusion ratio, ram speed, and billet temperature. The surface of the extruded profile will also have a higher cooling rate than the center. Consequently, the center has a high temperature longer than the edges which may lead to grain growth.

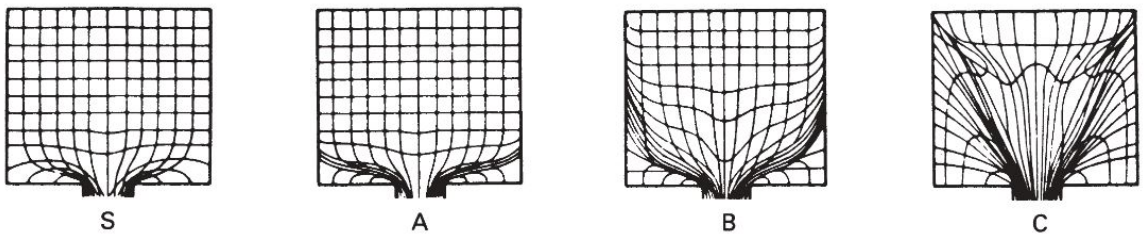

Fig. 2.6.2. Different flow patterns in metal extrusion. S: Homogeneous material with no friction. A: Homogeneous material with friction at die interface. B: Homogeneous material with friction at die interface and container. C: Inhomogeneous material or nonuniform temperature distribution in billet. Figure from reference [50].

2.7 Metal Forming

2.7.1 Rolling

Rolling is a metal forming process where a reduction in thickness is caused by compressive stresses exerted by rolls [35]. The process can be performed at elevated temperatures, known as *hot rolling*, or at room temperature, known as *cold rolling*. In cold rolling, the grains will be deformed as the cross-section is reduced. Unlike in hot rolling, the grains will not recrystallize [51]. This is illustrated in Figure (2.7.1). There are many different forms of rolling, and in this thesis two high rolling is used. This process is illustrated in Figure (2.7.2).

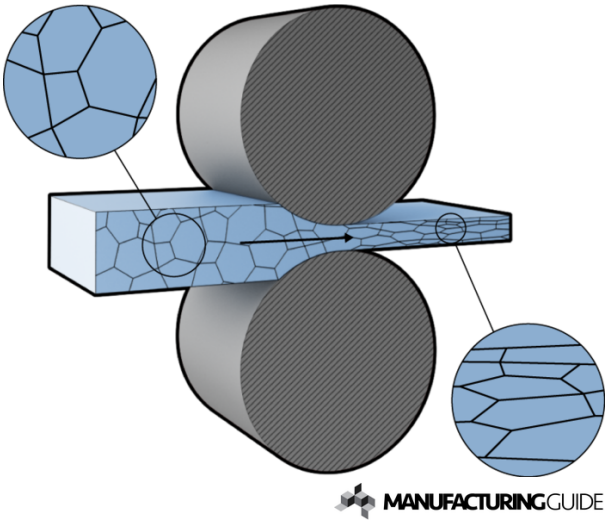

Fig. 2.7.1. Grain deformation during cold rolling. Image from reference [52].

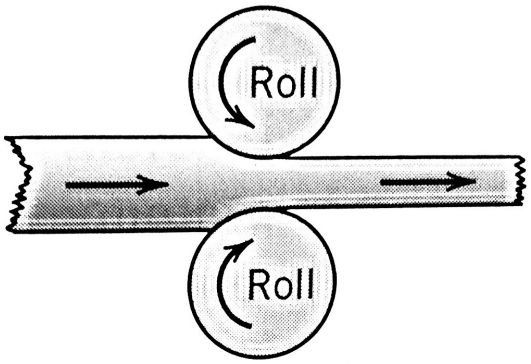

Fig. 2.7.2. Schematic illustration of two high rolling. Image from reference [35].

Rolling leads to a considerable amount of strain and strain hardening. Strain hardening, often referred to as work hardening, is caused by an increase in dislocation density. The amount of hardening will be dependent on the cross-sectional reduction and is often expressed as % cold work (%CW). % cold working is expressed in Equation (2.7.1)[35].

$$\%CW = \frac{A_0 - A_d}{A_0} \cdot 100 \tag{2.7.1}$$

where A_0 is the initial area and A_d is the area after rolling.

2.7.2 Rolling of Steel Reinforcement

Due to the high hardness and strength of steel, rebars needs to be hot rolled. The most common production routes of steel reinforcement can be summarized as follows [53]:

Steelmaking → Ladle refining → Continuous casting → **Hot rolling** →
Cold processing → Decoiling → Fabrication → Manufacture of welded fabric

Before hot rolling, the rebars are heated to 1100 °C - 1200 °C. The bars are rolled through a rolling mill consisting of several rolling steps. In each step, the cross-section is reduced and the shape/geometry changed. The temperature and reduction in cross-section has to be high enough to weld up any defects (cracks, porosity, segregation) introduced in the casting step.

2.8 Mechanical Properties and Geometry of Steel Reinforcement

The geometry of the rebars after rolling is different for different applications and are defined by government standards. In Norway the geometry is described in *NS-EN 10080:2005 - steel for the reinforcement of concrete - weldable reinforcing steel* [54]. In general, the reinforcement should have two or more rows of transverse ribs uniformly distributed. An example of rib geometry is given in Figure (2.8.1). Other requirements are as follows:

- Rib height, rib spacing, and rib inclination must be within the range of Table (2.8.1).
- Transverse ribs shall have a crescent shape and shall merge smoothly into the core of the product.
- The projection of the transverse ribs shall extend over at least 75% of the circumference of the product.
- The transverse rib flank inclination (α) shall be ≥ 45°and the transition from the rib to the core of the product shall have a curved edge.
- If longitudinal ribs are present, their height should not exceed 0.15 d.

Tab. 2.8.1. Ranges for rib parameters [54]. d = nominal diameter of bar.

Rib height, h	Rib spacing, c	Rib inclination, β
0.03 d to 0.15	0.4 d to 1.2 d	35°to 75°

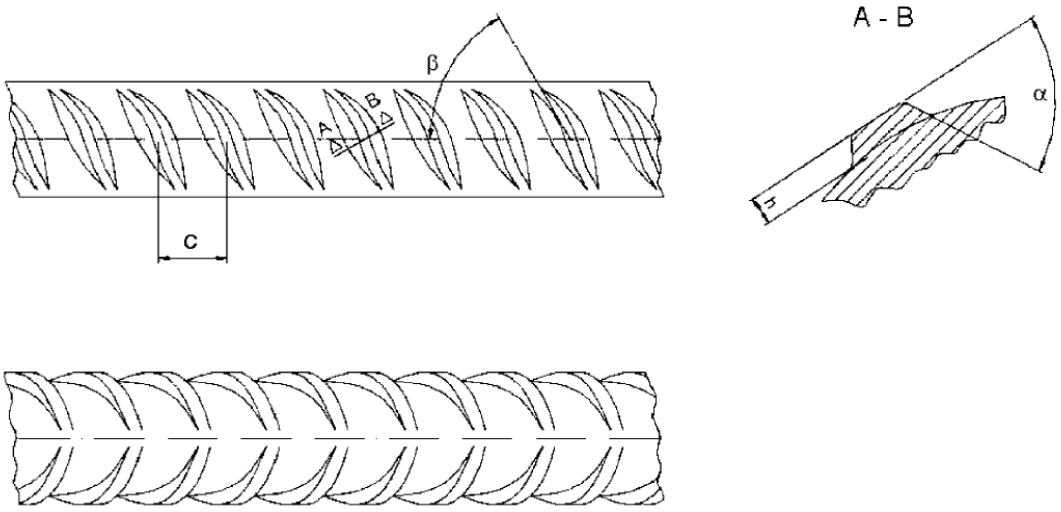

Fig. 2.8.1. Example of rib geometry. Figure from reference [54].

The required mechanical properties of steel reinforcement are defined by *NS-3576:2005 - steel for the reinforcement of concrete - dimensions and properties.* These are summarized in Table (2.8.2) and Table (2.8.3). There are no documented standard requirements for the use of aluminium as reinforcement.

Tab. 2.8.2. Tensile requirements of steel reinforcement by Norsk Standard [55].

Yield strength, σ_y	500 MPa
Tensile strength, σ_{UTS}	600 MPa

Tab. 2.8.3. Ductility requirements of steel reinforcement by Norsk Standard [55].

Bar diameter	Total Elongation
6 mm - 14 mm	7.5 %
16 mm - 40 mm	8.0 %

2.9 Properties

2.9.1 Tensile Strength

To ensure that a material can withstand the forces and loads they are subjected to during service, different standardized laboratory tests have been designed. One of the most common tests is the tension test [35]. From a tension test parameters such as ultimate tensile strength, σ_{UTS}, and yield strength, σ_Y, can be retrieved.

In an engineering tension test, a machined specimen is subjected to continuous uniaxial force. The elongation of the specimen is measured by an extensometer and the elongation is set to a constant rate [35, 56]. As well as the elongation, the instantaneous applied load is measured. The results are usually presented in an engineering stress-strain curve. Engineering stress is defined by the instantaneous load applied, F, and the original cross-section, A_0:

$$\sigma = \frac{F}{A_0} \tag{2.9.1}$$

The engineering strain is defined as the ratio between change in length, Δl and the original length, l_0:

$$\epsilon = \frac{\Delta l}{l_0} = \frac{l - l_0}{l_0} \tag{2.9.2}$$

A standard engineering stress-strain curve can be observed in Figure (2.9.1). The curve can be divided into two areas: elastic and plastic. The elastic area is the linear part of the curve and is described by Hook's law. Hook's law is given in equation (2.9.3) In this area the deformation is reversible. Plastic deformation is non-reversible deformation and is represented as the non-linear part of the stress-strain curve. The shape of the curve is dependent on the ductility of the specimen. A ductile specimen will show more plastic deformation than a brittle specimen. A brittle specimen will often fracture with little to no plastic deformation.

$$\sigma = \epsilon E \tag{2.9.3}$$

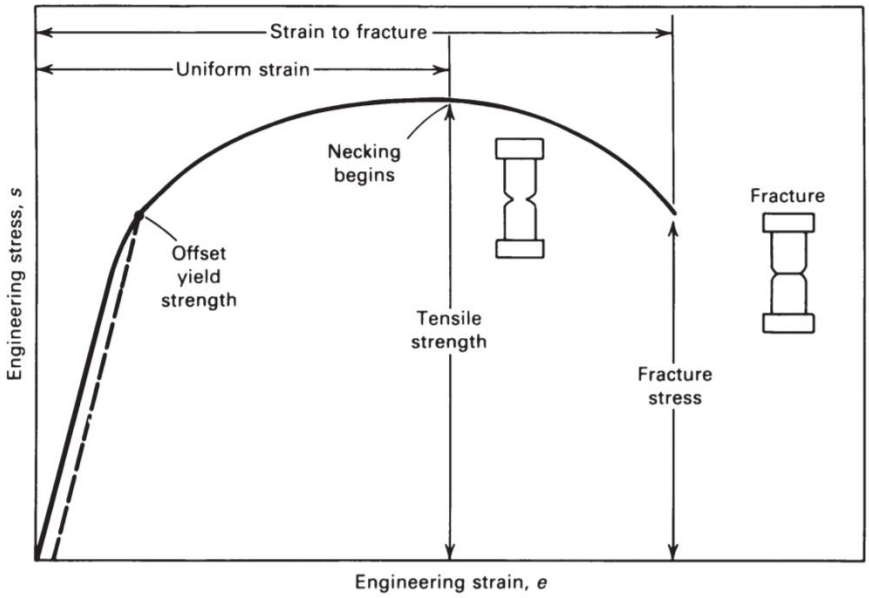

Fig. 2.9.1. Example of an engineering stress - strain curve. Image from reference [56].

2.9.2 Coefficient of Linear Thermal Expansion

Thermal expansion is reversible dimensional change caused by change in temperature [57]. The thermal expansion of a material is described by the coefficient of thermal expansion (CTE/α). In Table (2.9.1), CTE for pure aluminium, carbon steel, and concrete is given. For aluminium, the CTE will depend on the alloying elements. Figure (2.9.2) illustrates the effect of different elements.

Tab. 2.9.1. Coefficient of linear thermal expansion of different materials. Data from reference [35].

Material	Coefficient of Thermal Expansion $[(°C)^{-1}]$
Commercially pure Al (99.0 - 99.95 wt%)	23.6
Carbon steel	11.3 - 12.3
Concrete	10.0 - 13.6

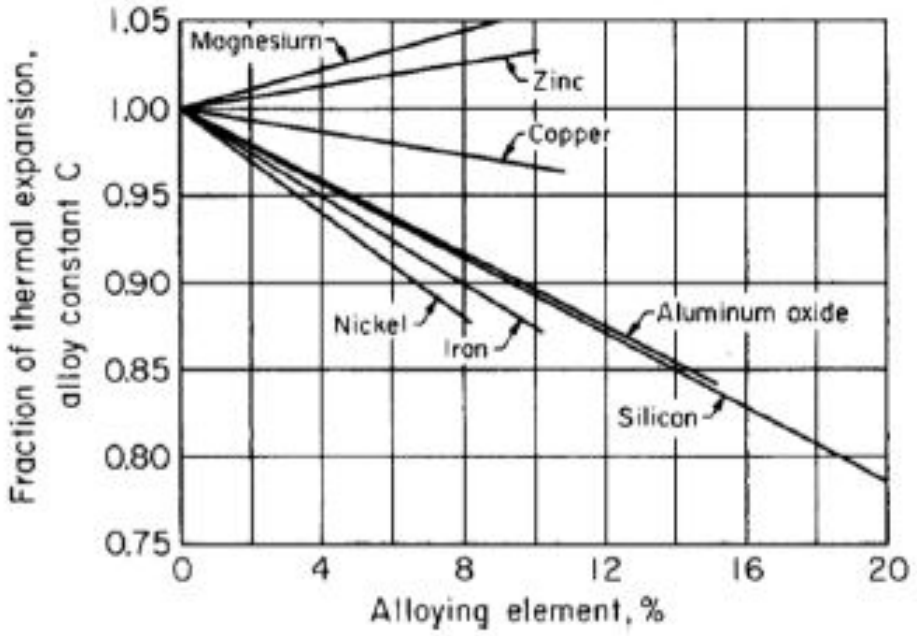

Fig. 2.9.2. Effect of alloying elements on the thermal expansion of aluminium. Fraction of thermal expansion is based on 99.996 wt% Al. Figure from reference [57].

2.9.3 Bond Strength of Concrete

Concrete is strong in compression, but weak and brittle in tension. Oppositely, steel is ductile and strong in tension. Because of this, concrete and steel are combined to create a composite material that has high tensile and compressive strength. However, for this to be considered a composite material, load has to be transferred between the concrete and steel. This is referred to as the bond strength [58].

A test for bond strength of concrete is defined by NS-EN 10080, Annex D: *Bond test for ribbed and indented reinforcing steel - Pull-out test.* In the test, a reinforcement bar or wire is incorporated in concrete. At one end of the bar tensile force is applied. The applied force is increased until either the bond or reinforcement fails. The force and relative displacement between steel and concrete are measured up to failure [54]. The principle of the test is illustrated in Figure (2.9.3).

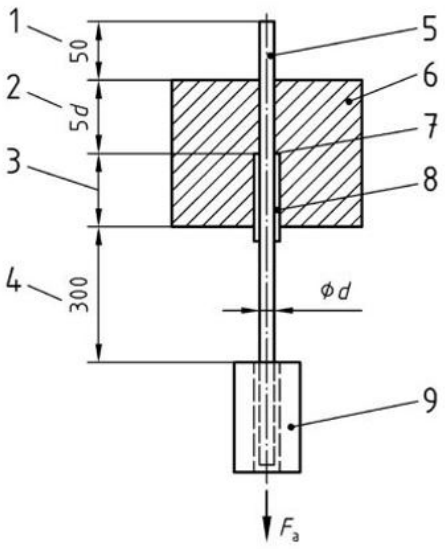

Key
1 part of the bar up to the point of application of the displacement measuring device
2 bond length
3 free pre-length 5*d*, min. 200 mm –5*d*
4 part of the bar to the point of application of the tension force
5 reinforcing bar
6 concrete
7 plugging
8 plastic sleeve
9 grip of the testing machine

Fig. 2.9.3. Illustration of bond test for reinforcing steel. Dimensions in millimetres. From reference [54].

The loading rate of the test is dependent on the bar/wire diameter. This is to ensure that the increase in bond stress is constant. Loading rate is determined by equation (2.9.4), where diameter (d) is given in mm. The test results are usually presented in a bond stress vs. slip curve. Bond stress is dependent on diameter, concrete properties, and the tension forces measured. Equation (2.9.5) provides the formula for transforming measured tension forces, F_a, to bond stress, τ_{dm}.

$$v_p = 0.56 \cdot d^2 \text{[N/S]} \tag{2.9.4}$$

$$\tau_{dm} = \frac{1}{5\pi} \frac{F_a}{d^2} \frac{f_{cm}}{f_c} \tag{2.9.5}$$

where f_{cm} is the target value of strength class and f_c is the average concrete strength of the test specimens.

3 Experimental

In this section the material used and the procedures followed are explained to show the reader how the results later presented, were found. A flow chart over the work is given in Figure (3.0.1).

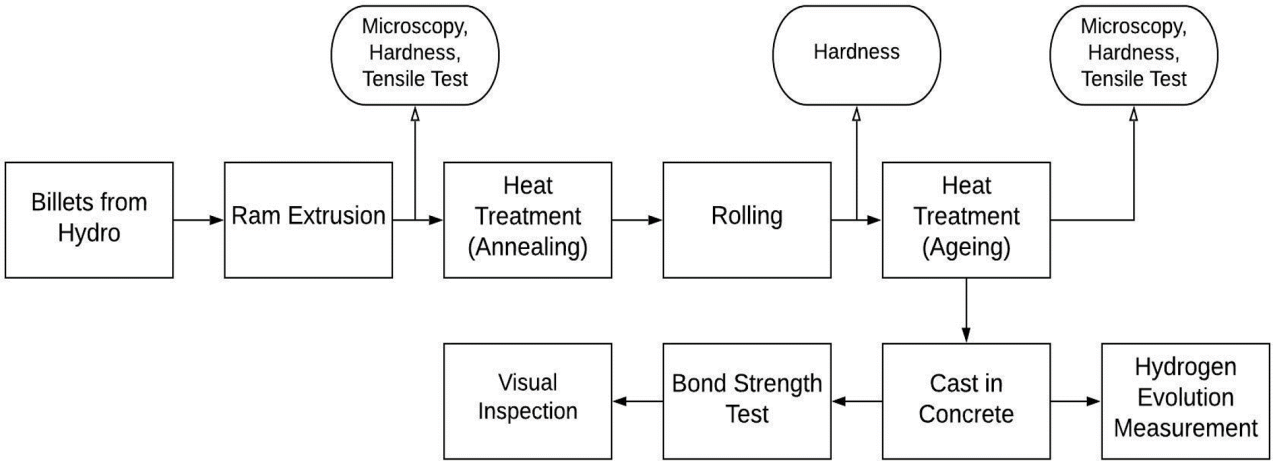

Fig. 3.0.1. Flow chart illustrating experimental work.

3.1 Material

Four different commercial aluminium alloys were used in this thesis. These were supplied by Hydro Aluminium AS and cast into billets and homogenized at Hydro Sunndalsøra. 6082 was homogenized at 575°C for 2 hours and 15 minutes. 5052, Al-9Si-2Cu, and Al-9Si-0.3Mg were homogenized 500°C for 3 hours. The billets were 20 cm long and had a diameter of 95 mm. A billet is shown in Figure (3.1.1). The composition of the different alloys were analysed by Hydro and are presented in the subsequent sections.

Fig. 3.1.1. Billet as it arrived from Hydro Aluminium AS.

A description of left-over material and the placement of it can be found in Appendix B.

6082

Alloy 6082 has medium strength and is usually heat-treated. It has high toughness, high yield strength and tensile strength. Because of this, it is often used in structural application. The composition of the alloy is given in Table (3.1.1).

Tab. 3.1.1. Composition of 6082-billet from Hydro.

Alloying element	Weight percent [wt]	Alloying element	Weight percent [wt]
Si	1.0818	Fe	0.2576
Cu	0.0029	Mn	0.5557
Mg	0.6451	Zn	0.0096
Ti	0.0229	Cr	0.1588
Ni	0.0054	Pb	-
Sn	0.0008	Na	-
Ca	0.0003	B	0.0023
Bi	0.0002	Zr	0.0016
V	0.0103	Be	-
Co	0.0002	Cd	-
Sb	-	Ga	0.0124
P	0.001	Li	-
Ag	0.0002	Hg	0.0002
Al	97.231		

5052

Alloy 5052 has a good combination of strength, formability, and corrosion resistance. It is often used in marine and transport applications. The composition is given in Table (3.1.2).

Tab. 3.1.2. Composition of 5052-billet from Hydro.

Alloying element	Weight percent [wt]	Alloying element	Weight percent [wt]
Si	0.1853	Fe	0.2618
Cu	0.0255	Mn	0.3159
Mg	2.0817	Zn	0.0095
Ti	0.0188	Cr	0.0024
Ni	0.0036	Pb	0.0013
Sn	0.0005	Na	-
Ca	0.0008	B	0.0017
Bi	-	Zr	0.0019
V	0.0082	Be	-
Co	0.0002	Cd	-
Sb	-	Ga	0.0085
P	0.0010	Li	-
Sr	-	Al	97.071

Al-9Si-2Cu

The Al-9Si-2Cu billet is a part of the 4xxx-alloying system. The composition of the alloy is given in Table (3.1.3). This alloy was used as a way of exploring the possibility of recycling old engine blocks into reinforcement in concrete. Engine blocks are made of cast alloys with high Si and Cu content. In addition, they are often secondary alloys with high alloying content and impurities.

Tab. 3.1.3. Composition of Al-9Si-2Cu billet from Hydro.

Alloying element	Weight percent [wt%]	Alloying element	Weight percent [wt%]
Si	9.1818	Fe	0.4094
Cu	2.1494	Mn	0.1128
Mg	0.2795	Zn	0.2169
Ti	0.0205	Cr	0.1171
Ni	0.0037	Pb	0.0012
Sn	0.0031	Na	-
Ca	0.0009	B	0.0023
Bi	-	Zr	0.0016
V	0.0086	Be	-
Co	0.0005	Cd	0.0006
Sb	0.0012	Ga	0.01
P	0.0009	Li	-
Sr	0.0001	Al	87.478

Al-9Si-0.3Mg

The Al-9Si-0.3Mg alloy is also a part of the 4xxx-alloying system. The composition of the alloy is given in Table (3.1.4). The alloy was designed to be similar to a wheel/rim alloy. Wheel scrap is also recyclable material that could be used as reinforcement in concrete.

Tab. 3.1.4. Composition of Al-9Si-0.3Mg billet from Hydro.

Alloying element	Weight percent [wt]	Alloying element	Weight percent [wt]
Si	9.2503	Fe	0.1305
Cu	0.0034	Mn	0.0020
Mg	0.3003	Zn	0.0082
Ti	0.0206	Cr	0.1171
Ni	0.0035	Pb	0.0075
Sn	0.0006	Na	-
Ca	0.0008	B	0.0016
Bi	-	Zr	0.0016
V	0.0084	Be	-
Co	0.0002	Cd	0.0006
Sb	0.0004	Ga	0.0097
P	0.0009	Li	-
Sr	-	Al	90.255

Recycled Engine Block

In addition to the commercial alloys above, an old engine block was going to be recycled through melt spinning and screw extrusion. Due to unforeseen circumstances, this could not be done. However, a lot of preparation work was conducted and this work is described in Appendix A.

Steel Reinforcement

In the final bond strength tests, standard steel reinforcement was used as a reference. It was assumed that these follow the standards described in Section 2.8. Figure (3.1.2) and Figure (3.1.3) shows reinforcement bars with Ø10mm and Ø20mm, respectively. The rebars were not characterized beyond the bond strength tests.

Fig. 3.1.2. Standard reinforcement bar with Ø10mm used in bond strength test.

Fig. 3.1.3. Standard reinforcement bar with Ø20mm used in bond strength test.

3.2 Grain Structure Characterization

The properties of a material are strongly dependent on the grain structure. Properties such as hardness and tensile strength can be explained by particle distribution, grain size, and grain size distribution. Grain structure characterization is therefore a significant part of this thesis. The characterization was conducted in the same way throughout the thesis and the procedure is presented below.

Small cross-sections (~ 1-2 cm thick) of ram-extruded profiles and rolled profiles were cut in two directions; transverse and longitudinal on the extrusion direction. This is illustrated in Figure (3.2.1). All sample cutting was done manually in a Struers Labotom-5 with a 30A25 silicon carbide cut-off wheel.

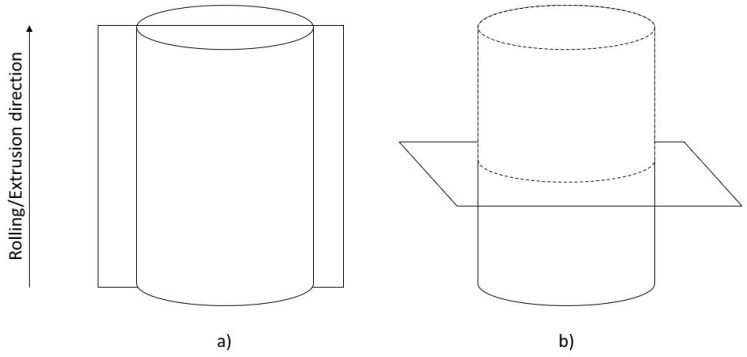

Fig. 3.2.1. Illustration of cutting direction relative to the extrusion/rolling direction. Showing a) longitudinal cross-section and b) transverse cross-section. Image from reference [3].

After cutting, the samples were cast in ClaroCit in a polymer casting mold (25 mm in diameter). ClaroCit is similar to epoxy, but it is less transparent and cures fast (20-30 min). The Clarocit powder/liquid ratio was approximately 5:3. Polishing and grinding of the samples were then executed in an automatic Struers Tegramin 30 polishing/grinding machine. The grinding and polishing procedure was based on Struers standard polishing process for Al-Si casting alloys [59]. A detailed overview of the procedure is given in Table (3.2.1).

Tab. 3.2.1. Grinding and polishing procedure.

Process	Grit/grain size	Grind/polish material	Time [s]	Cleaning procedure
Grinding	FEPA#220	SiC	Until plane	Water
Grinding	9 μm	Diapro Largo 9	240	Water and cotton swab
Polishing	3 μm	Diapro Mol 3	180	Water and cotton swab
Polishing	1 μm	Diapro Nap R1	120	Water and cotton swab
Polishing	0.04 μm	OP-U Non Dry	60	Water, cotton swab, and ethanol

3.2.1 Light Optical Microscopy (LOM)

Examinations in light optical microscopy were conducted in a Zeiss Axioscope, shown in Figure (3.2.2). The aluminium samples were examined in both bright field illumination and polarized light with a λ-plate (incline of 7°). To conduct a polarized light examination, the samples have to be anodized first. In this thesis, the samples were anodized in a Struers Lectropol-5 with 5% tetrafluorobotic acid (HBF_4) and a voltage of 20V for 120 seconds. The surface area that was anodized varied from 1 cm^2 (10 mm profiles) to 3 cm^2 (20 mm profiles).

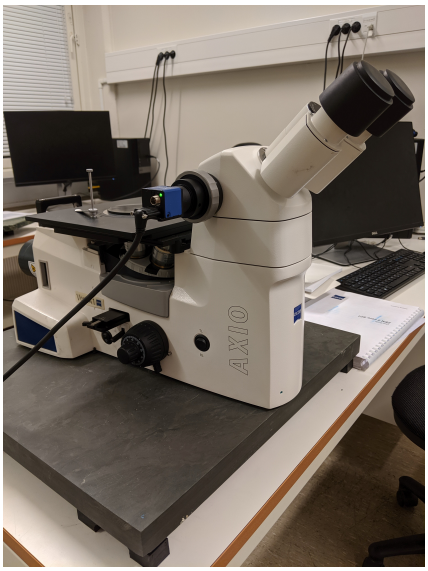

Fig. 3.2.2. Zeiss Axioscope used for light optical microscopy.

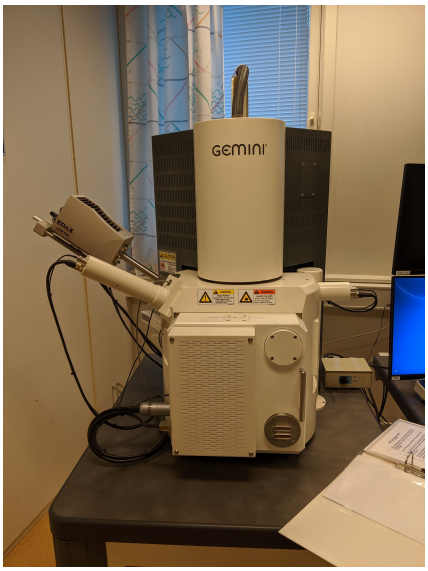

Fig. 3.2.3. Zeiss Supra 55VP used for SEM examinations. EDS attachment can be seen on the left, labeled as "EDAX".

3.2.2 Scanning Electron Microscopy (SEM)

Since the aluminium samples were cast in ClaroCit, they had to be wrapped in Al-foil and dried at 60°C overnight. Al-foil ensures that the electron beam from the SEM is reflected and thus minimizes charging. The drying process is to remove all residue moisture. Residue moisture in the ClaroCit could lead to heat generation as the chamber is evacuated. Scanning electron imaging and Energy-Dispersive X-ray Spectroscopy (EDS) were conducted in a Zeiss Supra 55 VP, shown in Figure (3.2.3). The SEM setting are summarized in Table (3.2.2).

Tab. 3.2.2. Settings used for SEM

Voltage [kV]	Aperture size [μm]	High current
17	120	Yes

3.3 Mechanical Property Measurements

3.3.1 Hardness

The hardness of the ram-extruded profiles was measured shortly after they were removed from the freezer (see Section 3.4). Samples with length = 1 cm of each profile were cut (transverse cross-section) and cast in ClaroCit. To ensure a plane surface the samples were polished as described in Table (3.2.1). The measurements were done with a Zwick Roell ZHV30 Vickers hardness tester in a rhombus pattern, as illustrated in Figure (3.3.1). The force was set to 1 kg and dwell time 10 s.

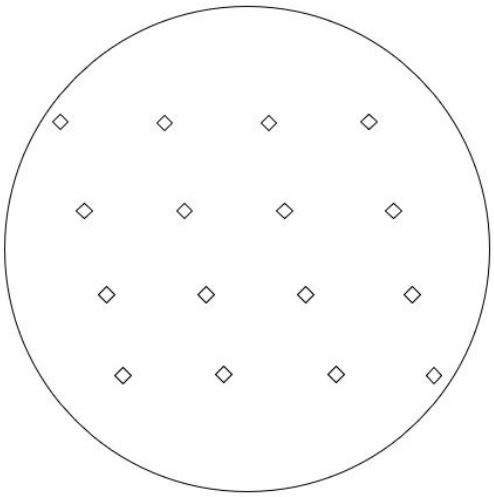

Fig. 3.3.1. Sketch of hardness measurement pattern.

The hardness of the rolled profiles was also mapped. It was measured in the same way as for the ram-extruded profiles, but the hardness of the longitudinal cross-section was measured as well.

3.3.2 Tensile Strength

The tensile properties of the ram-extruded and heat-treated profiles were measured in a MTS 810 with a laser extensometer (max. load 100 kN). Round test specimens were machined by Finmekanisk verksted at NTNU, Trondheim. The geometry and measurements are given in Figure (3.3.2). The elongation rate was set to 2 mm/min. The heat-treated tensile specimens were heat-treated after machining. The heat treatment is presented in Section 3.6.

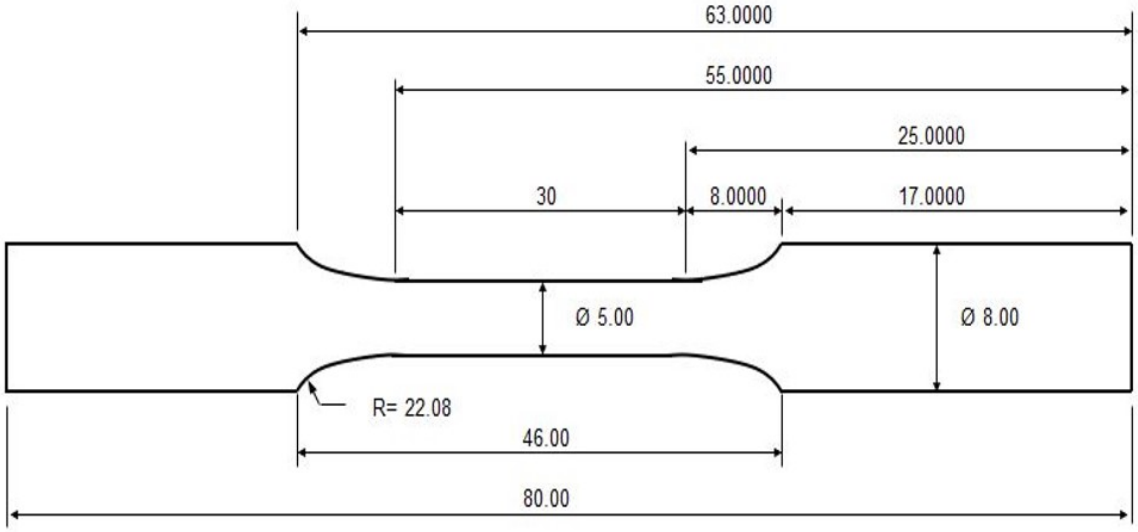

(a) Ø10mm

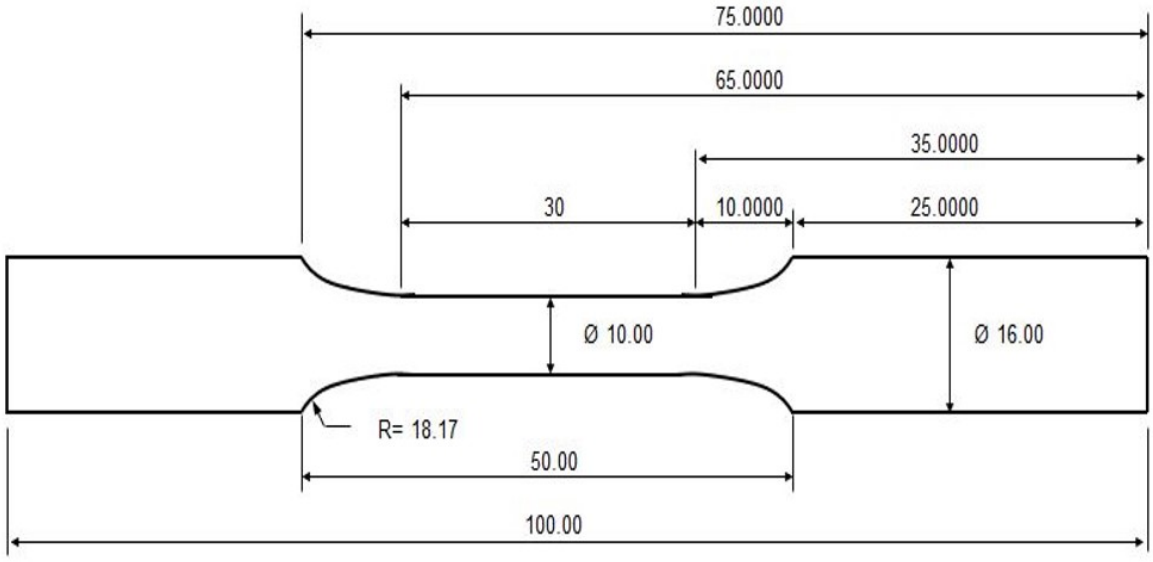

(b) Ø20mm

Fig. 3.3.2. Geometry and measurements of tensile test specimens.

3.4 Extrusion

The aluminium reinforcement bars were produced via ram extrusion. It was decided to use this process because it is a well-established, quick, and relatively easy production method. Profiles with two different circular cross-sections were extruded, one with a diameter of 10.5 mm (hereby referred to as Ø10mm) and one with a diameter of 20 mm.

The extrusion took place in the SINTEF laboratories at Verkstedhallen in Trondheim and was conducted by Hydro in collaboration with SINTEF and NTNU. The process was executed with a vertical 800 tons press extruder that reached over two floors. The part of the extruder located on the first floor is shown in Figure (3.4.1a). In this image, the ram and die holder can be observed. Since two different cross-sections were to be extruded, two different water cooling set-ups had to be used. These are shown in Figure (3.4.1b) and (3.4.1c). They are also schematically illustrated in Figure (3.4.2).

Prior to extrusion, all of the billets were homogenized and pre-heated to 430 °C. As mentioned in Section 2.6.1, this improves the workability and extrudability. The 6082 billets were over-heated as well. This was done by heating the billet to 560 °C and then cooling it to 500 °C. The extrusion parameters are given in Table (3.4.1). The complete extrusion logs can be found in Appendix C. After extrusion, the profiles were put in a freezer to maintain the as-extruded microstructure.

Tab. 3.4.1. Extrusion parameters.

Alloy	Ram temperature [C]	Initial cross-section [mm^2]	Final cross-section [mm^2]	Extrusion ratio	Ram speed [mm/s]	Ram force (max/min) [kN]
Ø10mm						
6082	180	7088.2	86.6	81.8	6.1	3996/2897
5052	96	7088.2	86.6	81.8	2.9	5708/3663
Al-9Si-0.3Mg	184	7088.2	86.6	81.8	2.9	3701/2696
Al-9Si-2Cu	186	7088.2	86.6	81.8	1.4	4582/3260
Ø20mm						
6082	50	7088.2	314.2	22.6	2.9	3086/2175
5052	100	7088.2	314.2	22.6	2.9	4923/2836
Al-9Si-0.3Mg	96	7088.2	314.2	22.6	3.3	2917/2045
Al-9Si-2Cu	115	7088.2	314.2	22.6	4.9	4275/2547

(a) Extruder at the first floor.

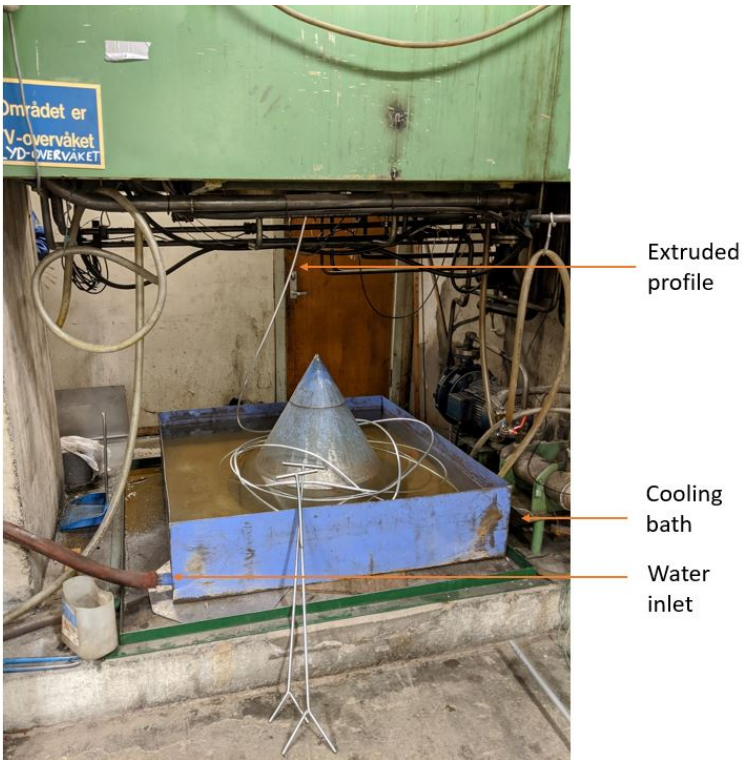

(b) Extruder in basement showing setup for Ø10 mm profiles.

Fig. 3.4.1. Images of vertical extruder used for extrusion of aluminium rebars.

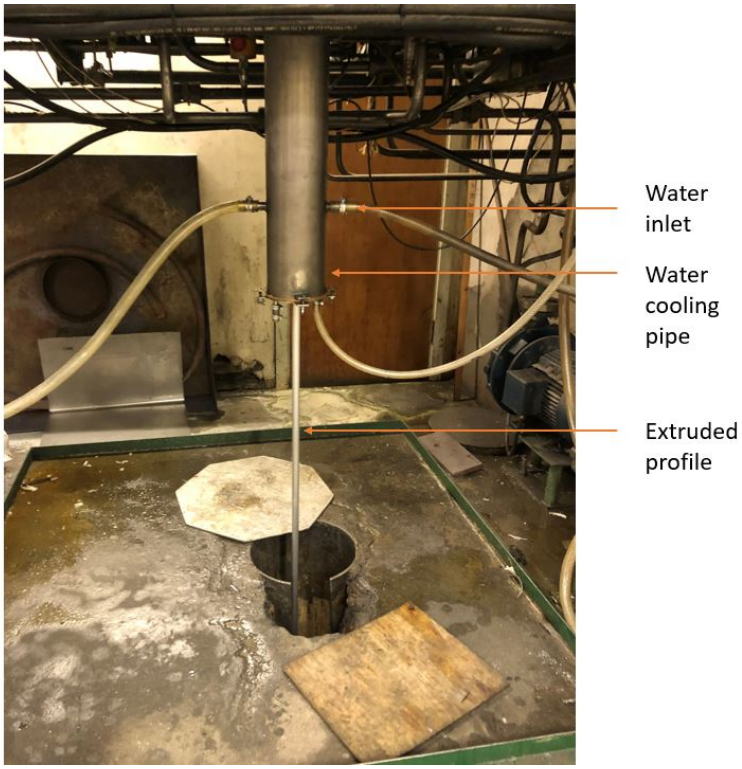

(c) Extruder in basement showing setup for Ø20 mm profiles.

Fig. 3.4.1. Images of vertical extruder used for extrusion of aluminium rebars.

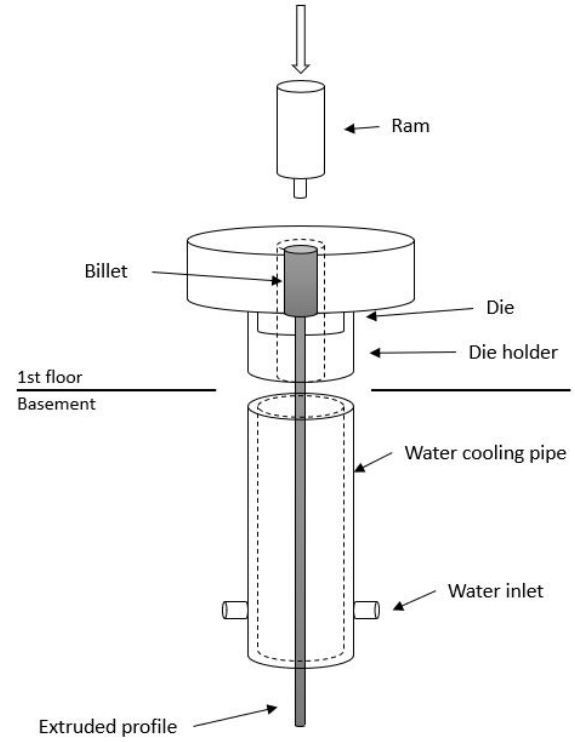

(a)

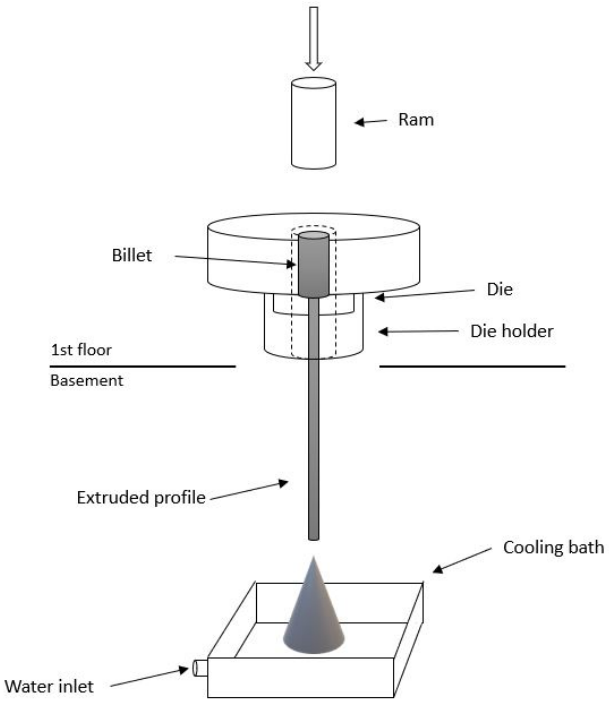

(b)

Fig. 3.4.2. Schematic illustration of extrusion setup for (a) 20mm profiles and (b) 10mm profiles.

3.5 Rolling of Reinforcement Bars

In the initial stages of this project, it was decided that the aluminium profiles were going to be rolled before being cast in concrete. Traditional steel reinforcement has ribs to enhance bond strength. To make similar ribs in aluminium reinforcement, roller tracks were designed by Rune Østhus at SINTEF. These were based on the NS 3576 standard. The roller tracks were subsequently machined into two rollers by SITO Mek A/S at Tingvoll. The theoretical rib values after rolling are given in Table (3.5.1). Images from simulations of the rolling process are given in Appendix D. The rolls before and after installation can be observed in Figure (3.5.1). After installation, a small shift between the upper and lower roll could be seen. It is uncertain whether this was caused by a fault in the machining or a misalignment in the roller.

Tab. 3.5.1. Theoretical rib values after rolling.

Initial diameter [mm]	Final diameter, excl. ribs [mm]	Final diameter, incl. ribs [mm]	Rib height, [mm]
10.5	9.29	9.92	0.32
20	18.62	19.67	0.53

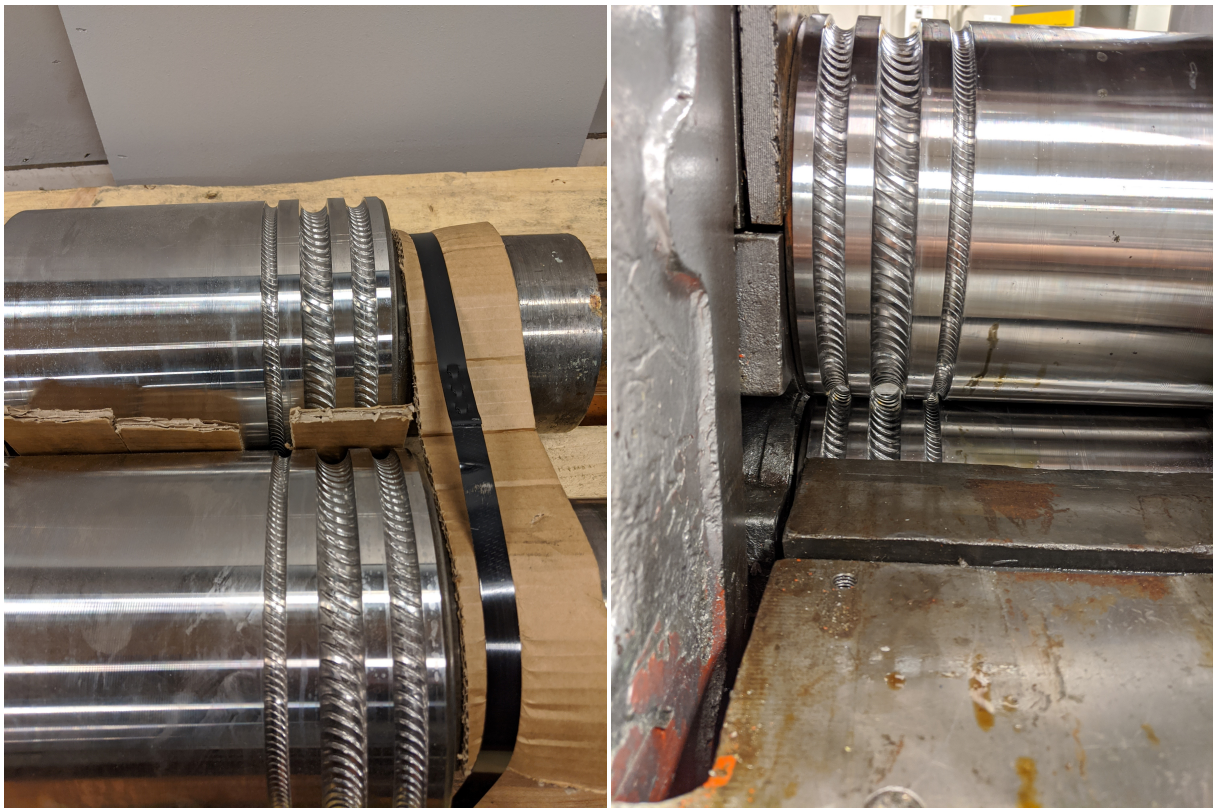

(a) Rolls before installation. **(b)** Rolls after installation in the rolling mill.

Fig. 3.5.1. Rolls designed for rolling of aluminium reinforcement.

Al-9Si-2Cu had to annealed before rolling to lower the hardness. Different heat treatments were tested, but in the end, the following process was used: 525 °C for 3 hours → 250 °C for 2 hours → air cooling. The remaining alloys were not annealed before rolling.

As the rolling commenced, it was discovered that the rolling resulted in significant bending of the profiles. Therefore, a simple device was made by Pål Skaret to minimize bending. Figure (3.5.2) shows the set-up during operation.

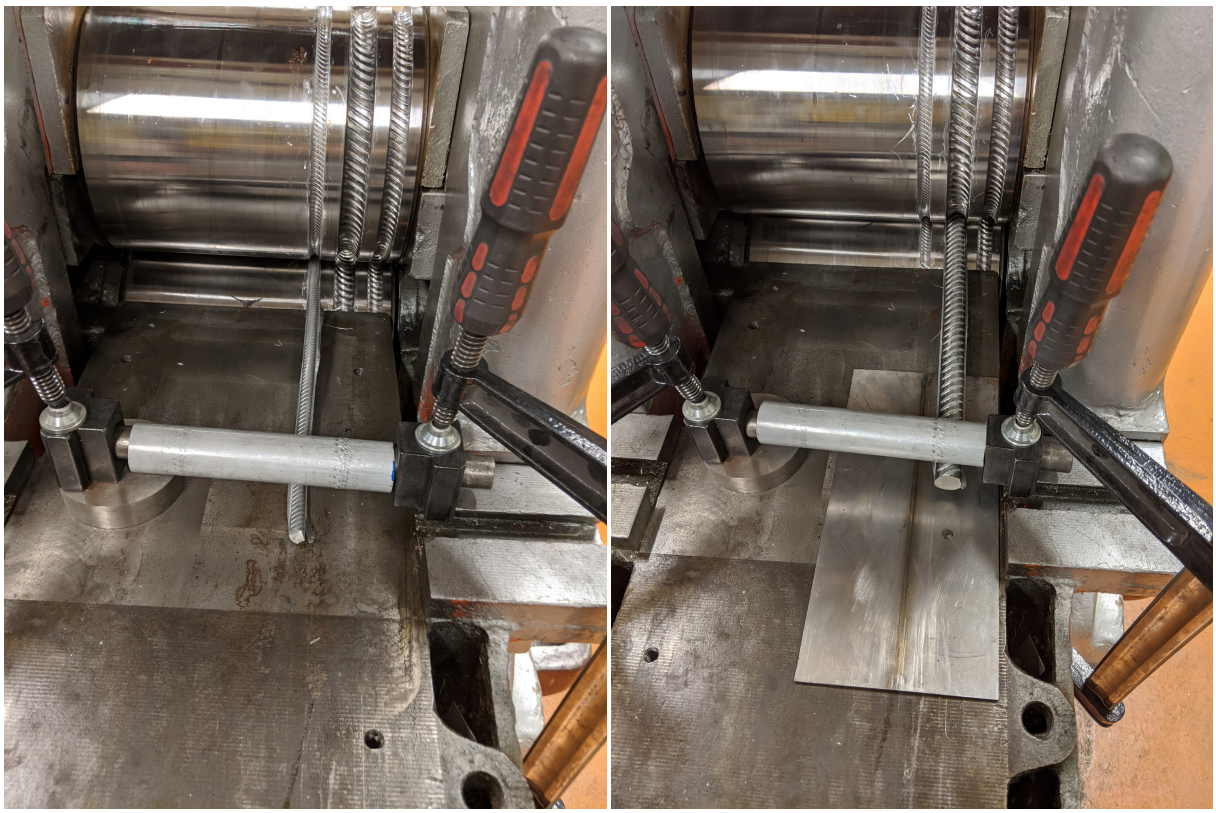

(a) **(b)**

Fig. 3.5.2. Image showing set-up during rolling of (a) 10mm and (b) 20mm profiles.

3.6 Artificial Aging

The combination of Al, Si, Mg, and/or Cu in 6082, Al-9Si-2Cu, and Al-9Si-0.3Mg, makes them susceptible to precipitation hardening. The precipitation sequences and mechanisms have already been discussed in Section 2.5.3. Since aluminium usually has lower strength than steel, the rolled profiles needed to be aged to increase the strength as much as possible. The two 4xxx-alloys did not have a known aging curve on which the heat treatment could be based. Therefore, the aging curve had to be found.

The aging curves of the 4xxx-alloys were found by first cutting Ø10mm samples with length 1cm. The samples were then solid solution heat-treated at 525°C for 5 hours, quenched, aged at 180 °C, and quenched after 5 min, 10 min, 20 min, 1 hour, 3 hours, 5 hours, 8 hours, 12 hours, and 24 hours. The hardness was measured as quickly as possible after each time interval. The final aging curves can be found in Section 4.3.1.

From the aging curves, the time until T6 (peak-aged condition) was determined. This result was used to age the rolled profiles before casting and bond strength testing. Solid solution heat treatment temperature and time, and aging temperature and time until T6 is given in Table (3.6.1). The heat treatment procedure of 6082 was based on the work of Kjetil Kristiansen [60].

Tab. 3.6.1. Artificial aging temperature and time.

Alloy	SSHT* temperature [°C]	SSHT* time	Aging temperature [°C]	Aging time until T6
6082	530	10 min	175	9 h
Al-9Si-2Cu	525	5 h	180	12 h
Al-9Si-0.3Mg	525	5 h	180	8 h

*SSHT = Solid Solution Heat Treatment.

3.7 Casting and Bond Strength Test of Aluminium Reinforced Concrete

After rolling and subsequent heat treatment, the aluminium profiles were cast in concrete by SINTEF. The concrete mix was based on the DARE2C concept and the complete recipe for 30l concrete is given in Table (3.7.1). Ø10mm profiles were cast in 150mm x 150mm x 150mm cubes and Ø20mm profiles were cast in 200mm x 200mm x 200mm cubes. The samples were then left to harden for a minimum of 14 days before bond strength testing could commence. As a reference, four standard steel rebars (2 x Ø10mm and 2 x Ø20mm) were cast and tested as well. The hardened samples can be seen in Figure (3.7.1)

Tab. 3.7.1. Recipe of concrete mix used in bond strength tests and hydrogen measurements. Mix volume = 30 l.

Material	Weigth* [kg]
Norcem anlegg SR A-5319 (Low alkali cement)	5.044
Calcined clay	6.165
Free water	5.831
Absorbed water	0.172
0-18 Årdal A-5231 (Aggregate)	29.796
8-16 Årdal A-5231 (Aggregate)	21.239
Sika viscocrete RMC-315 (Superplasticizer)	0.067

*wet weight

(a) Ø10mm **(b)** Ø20mm

Fig. 3.7.1. Aluminium rebars cast in concrete.

The bond strength testing was conducted and designed by SINTEF. The test was based on

NS-EN 10080, but some adjustments were made due to limited material and equipment. Figure (3.7.2) summarizes the parameters in the tests. Displacement was logged with a Linear Variable Differential Transformer (LVDT). Loading rate was estimated from equation (2.9.4) and set to 56 N/S and 224 N/S for Ø10mm and Ø20mm, respectively. The test set-up and components are given in Figure (3.7.3).

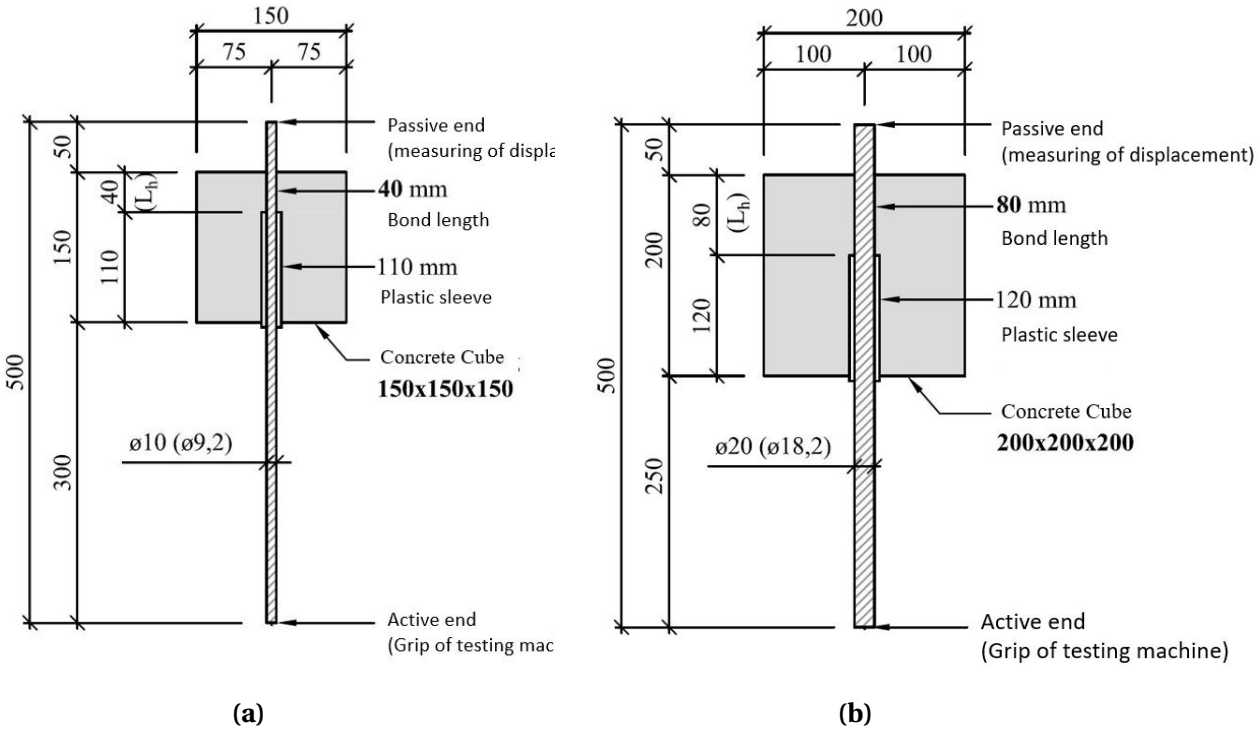

Fig. 3.7.2. Bond strength test design for (a) Ø10mm and (b) Ø20mm profiles. All measurements are given in mm.

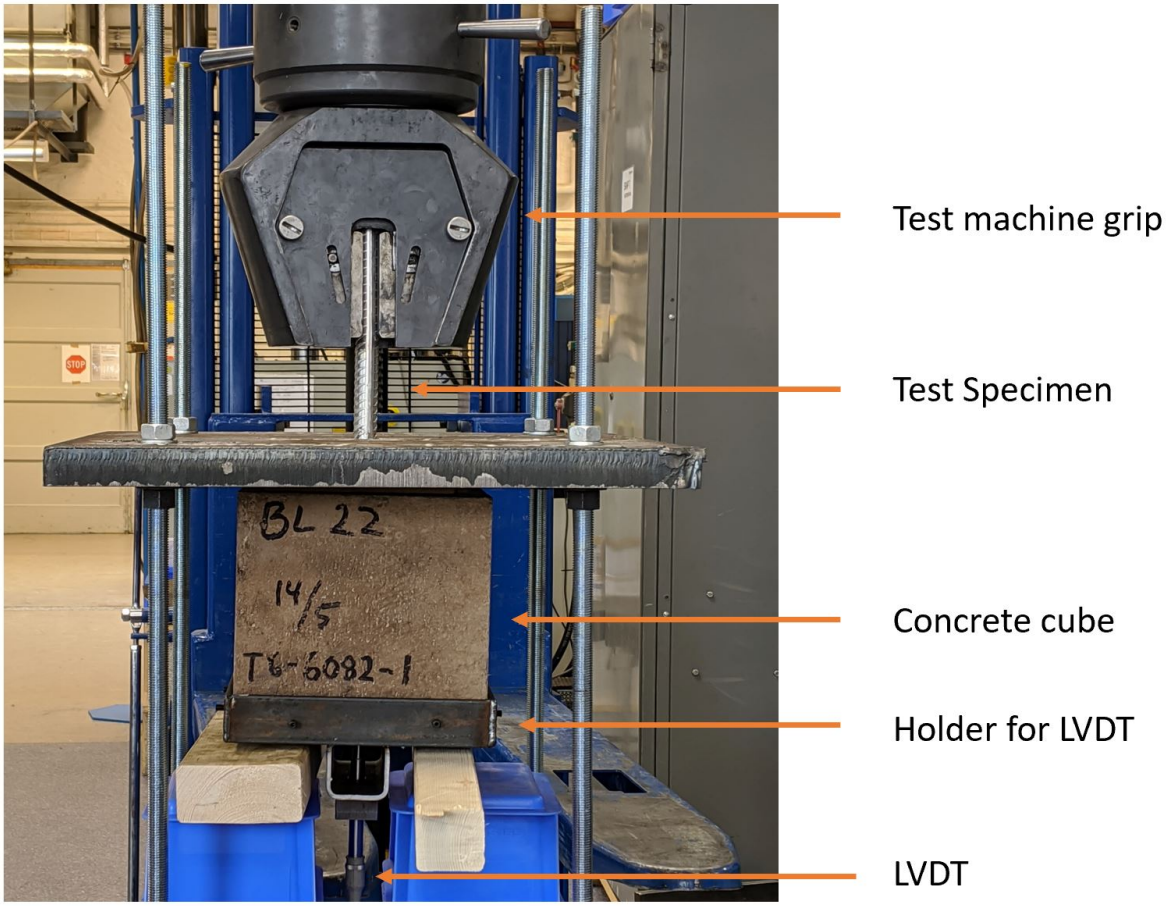

Fig. 3.7.3. Bond strength test set-up with some important components marked.

3.8 Hydrogen Gas Measurements

Measuring hydrogen gas evolution of aluminium in concrete can be used as an indicator of how the aluminium sample corrodes. This can be seen from equation (2.3.2). The hydrogen evolution was therefore measured for all the alloys (as extruded) with and without ribs. It was also measured for 6082, Al-9Si-2Cu, and Al-9Si-0.3Mg in T6 temper without ribs.

First, the different alloys with Ø10 mm were cut into 4 cm long pieces. These pieces were cast in concrete in small cups and placed in an exicator, see Figure (3.8.1). Gas Chromatography (GC) was then conducted by SINTEF. Figure (3.8.2) shows the GC set-up.

Fig. 3.8.1. Cup containing concrete and aluminium sample.

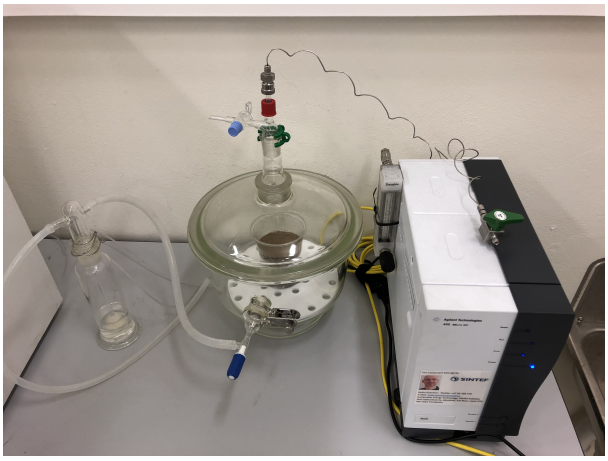

Fig. 3.8.2. Gas chromatography set-up for measuring hydrogen gas evolution. The cup was placed in the exicator seen in the centre of the image.

4 Results

4.1 Characterization of Extruded Profiles

4.1.1 Grain Structure Characterization by LOM

Four alloys of different compositions were extruded through conventional ram extrusion (6082, 5052, Al-9Si-2Cu, and Al-9Si-0.3Mg). A minimum of 3 billets per alloy were extruded as Ø10mm and Ø20mm profiles. In this section, a selection of LOM micrographs of each alloy is given. These are micrographs of the profiles that were eventually cast in concrete.

Bright-field (BF) micrographs of the transverse cross-section of the extruded alloys are given in Figure (4.1.1) through Figure (4.1.4). The alloys with high alloying content (Al-9Si-2Cu and Al-9Si-0.3Mg) have a high concentration of precipitates on the surface. These are not homogeneously distributed and appear to have no particular shape. 6082 and 5052 have some precipitates on the surface, but these are few and small.

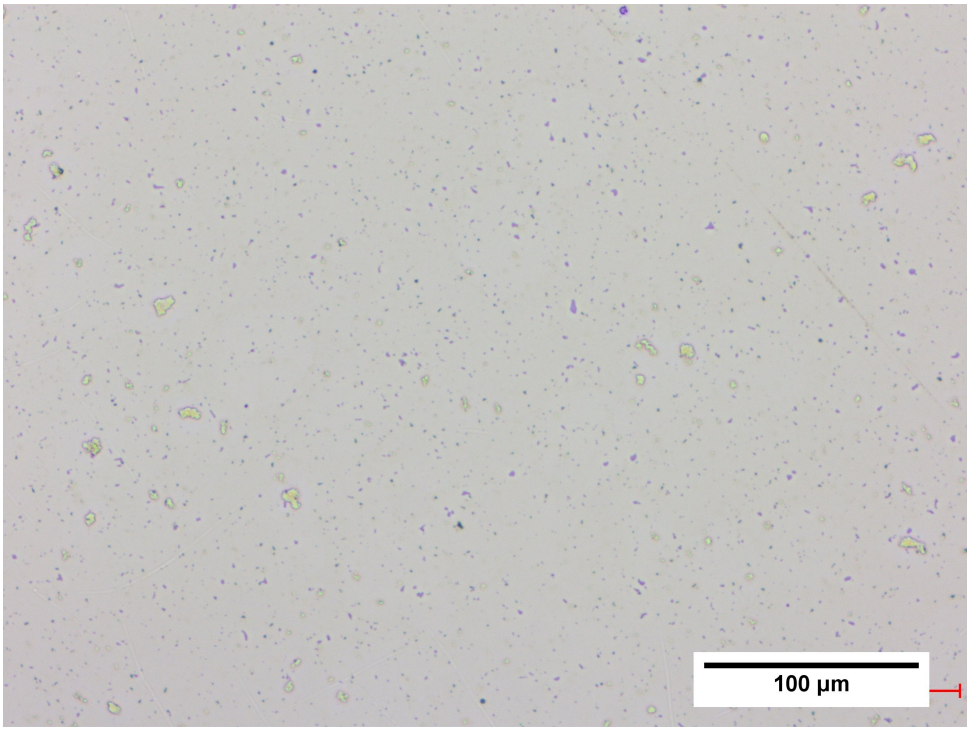

(a) Ø10mm

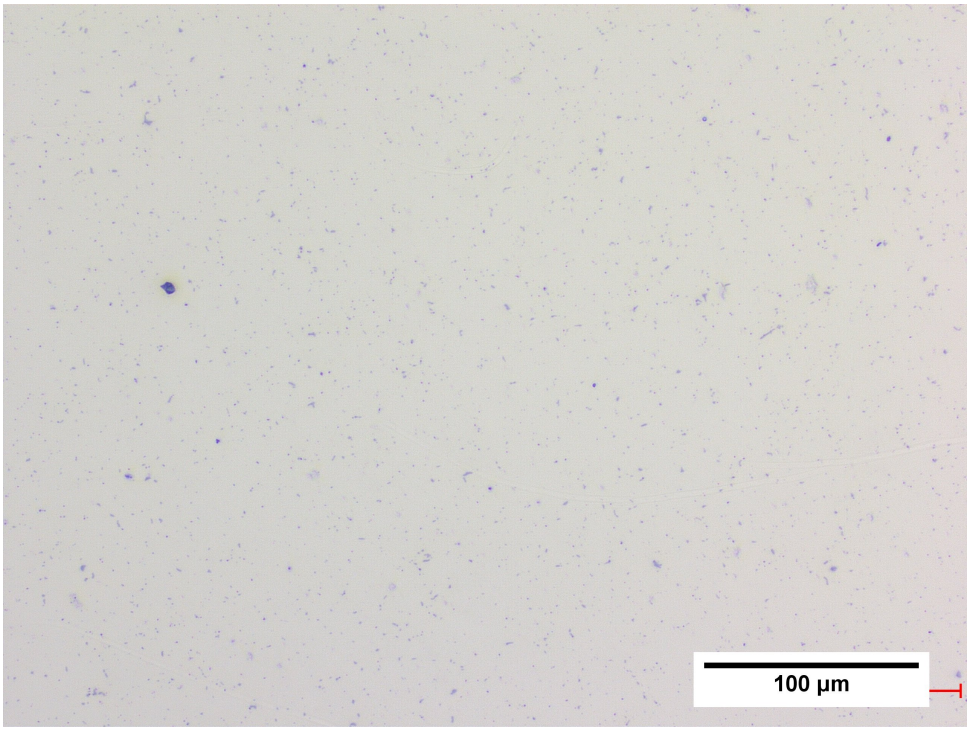

(b) Ø20mm

Fig. 4.1.1. Bright-field illumination and 20x magnification of transverse cross-section of 6082.

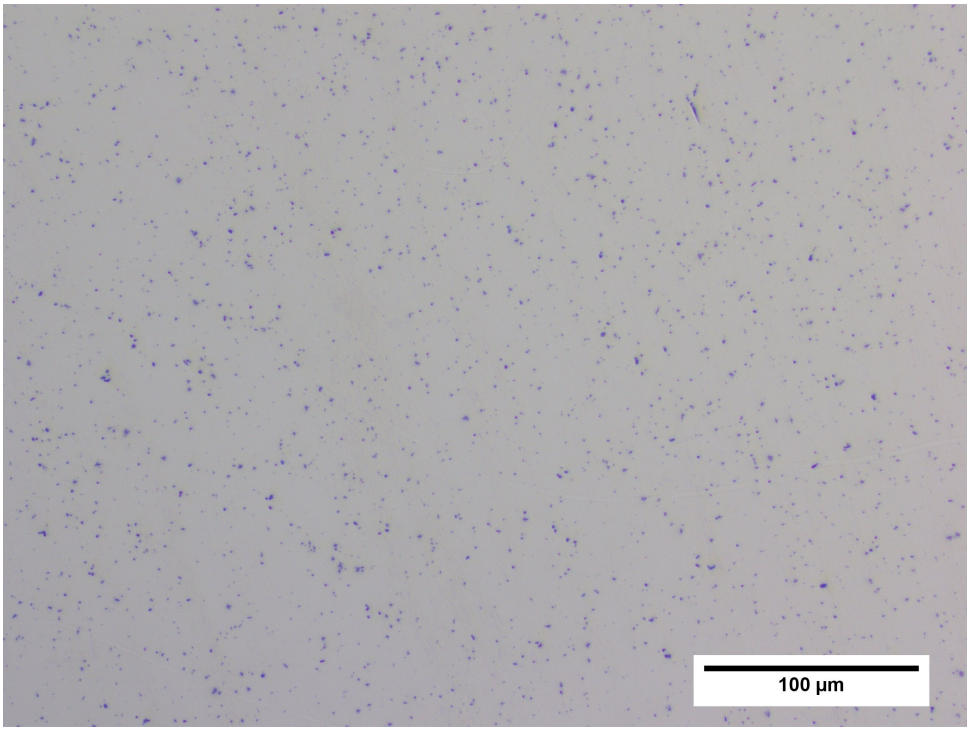

(a) Ø10mm

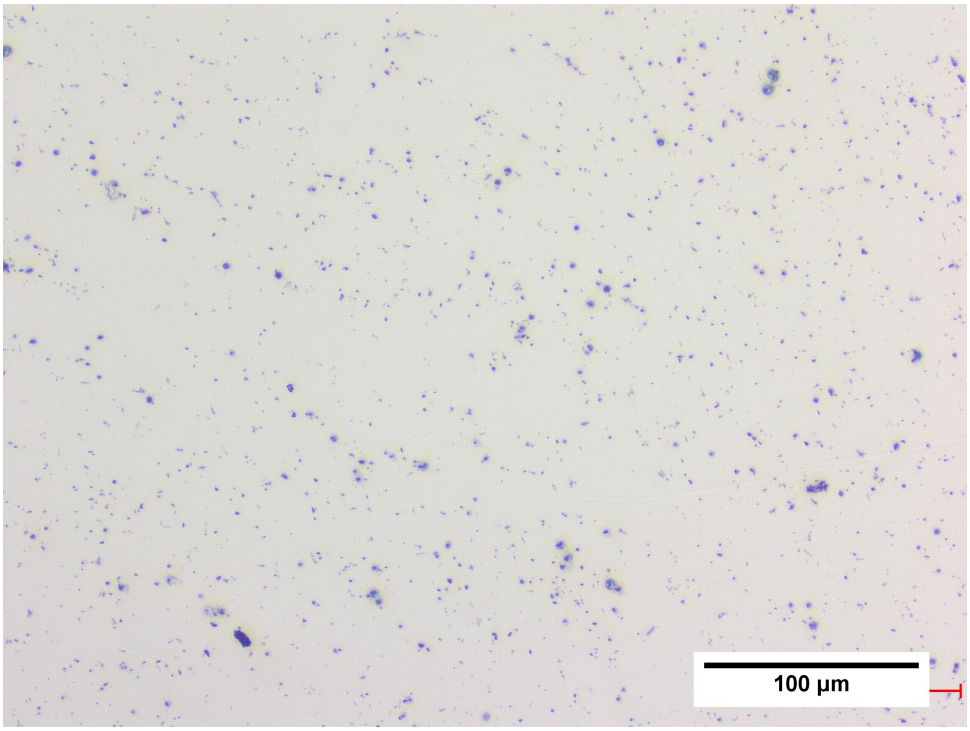

(b) Ø20mm

Fig. 4.1.2. Bright-field illumination and 20x magnification of transverse cross-section of 5052.

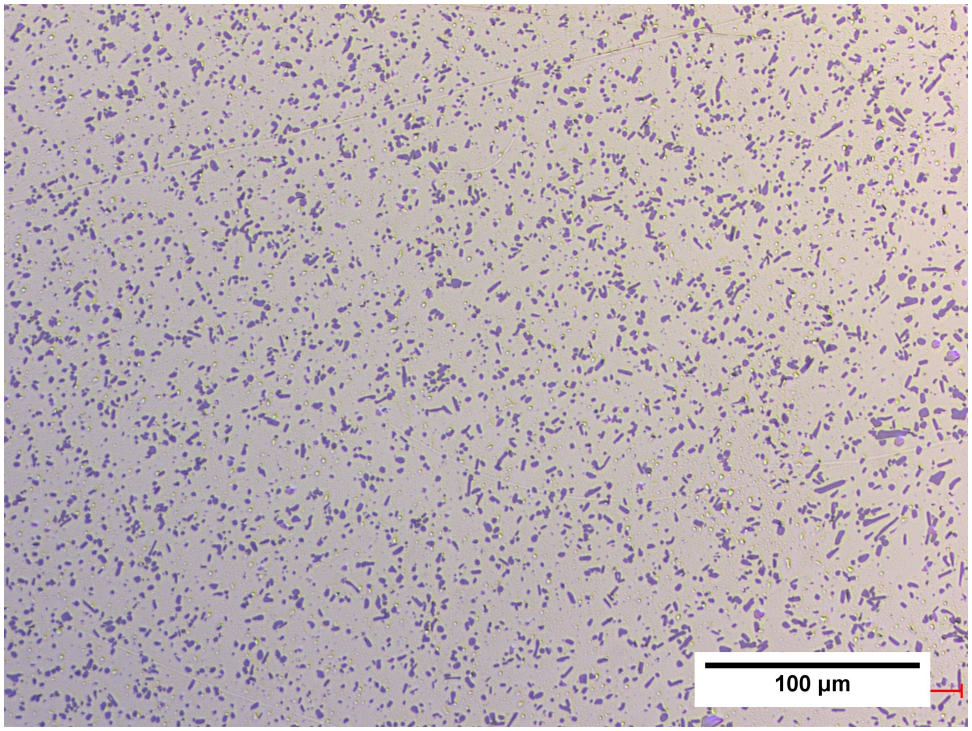

(a) Ø10mm

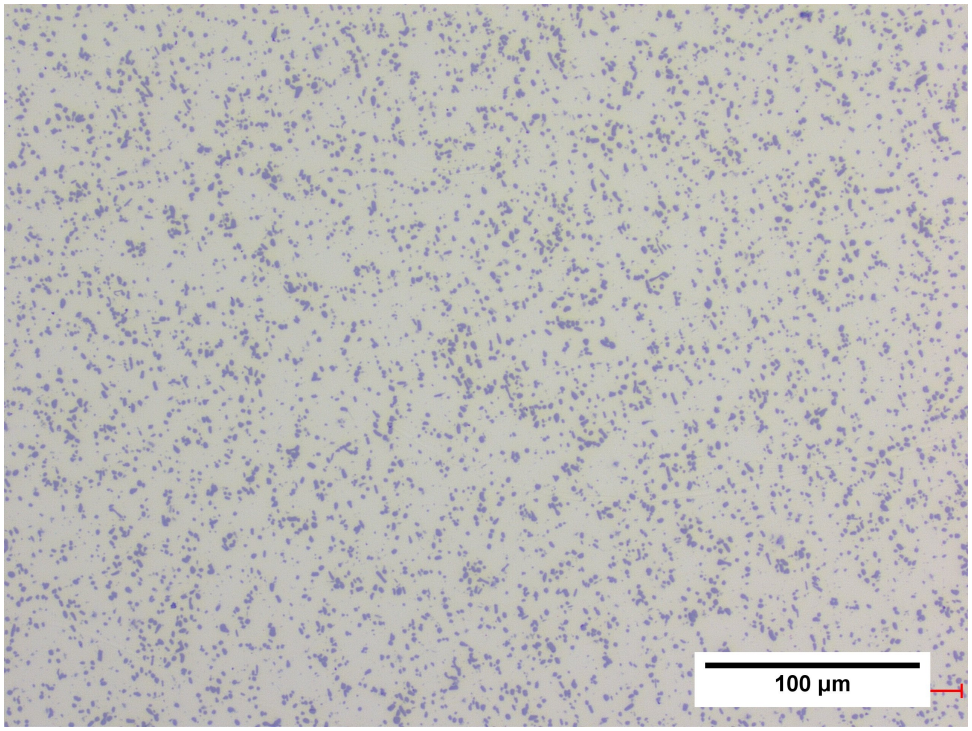

(b) Ø20mm

Fig. 4.1.3. Bright-field illumination and 20x magnification of transverse cross-section of Al-9Si-2Cu.

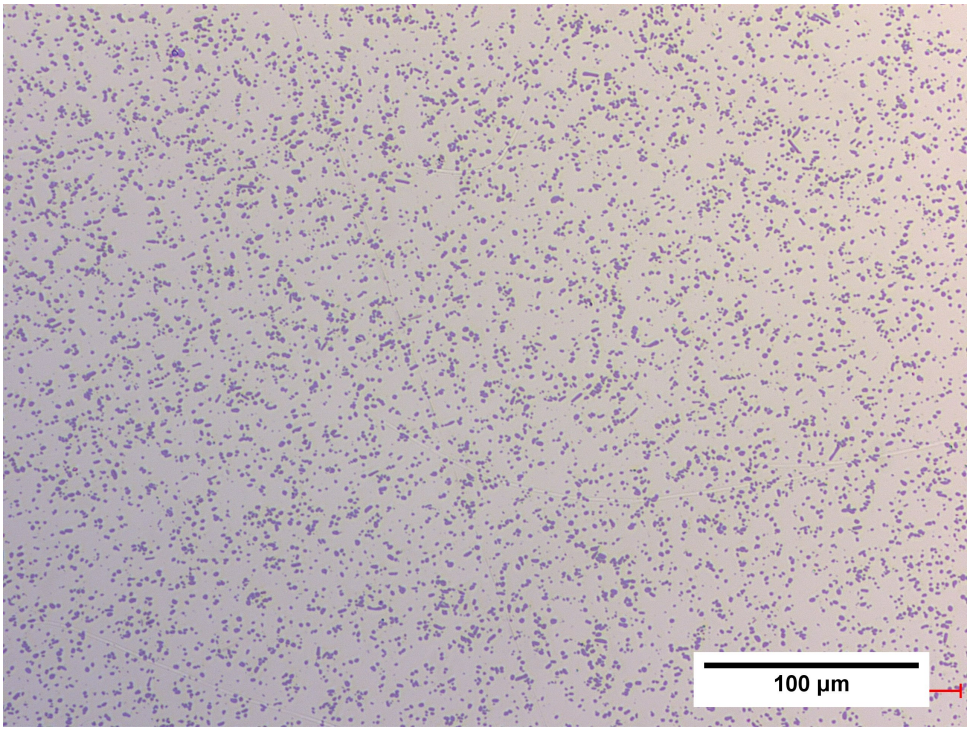

(a) Ø10mm

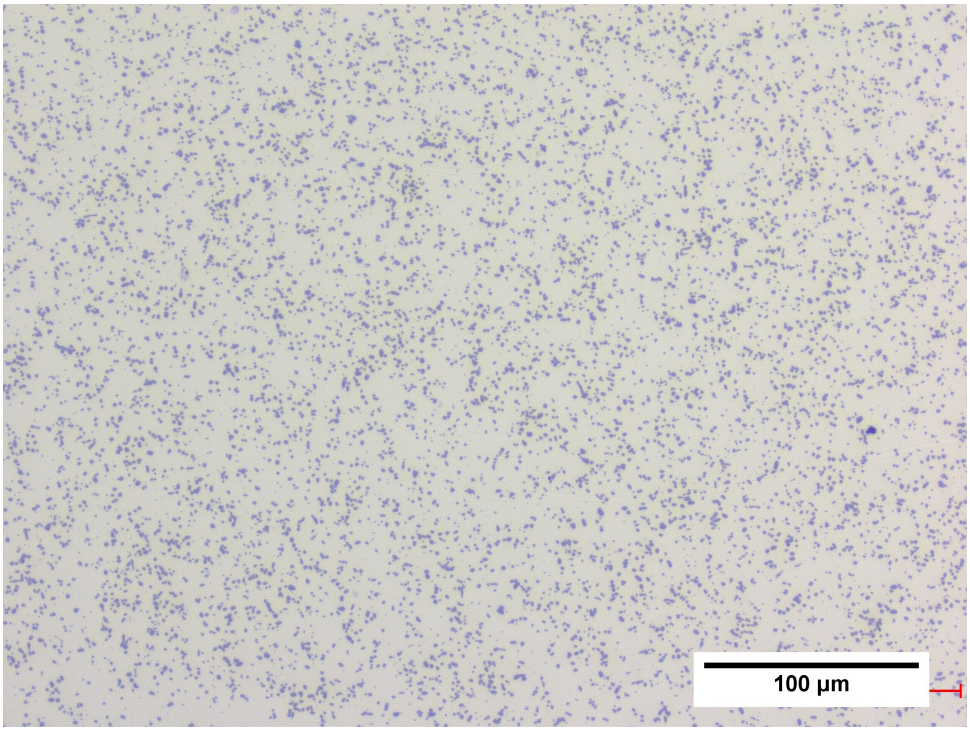

(b) Ø20mm

Fig. 4.1.4. Bright-field illumination and 20x magnification of transverse cross-section of Al-9Si-0.3Mg.

Polarized light illumination micrographs of the transverse cross-sections are given in Figure (4.1.5) through Figure (4.1.8). The micrographs were taken from the edge of the sample towards the center. They were made by stitching multiple images together,resulting in a seam in some parts of the images.

Except from 6082, the alloys have a similar grain structure with the smallest grain size located at the edges. The grains have different shapes and vary in size. For the Ø10mm profile of 6082, the grains are large at the edges and no distinct grain boundaries can be seen in the center. In the micrograph of the Ø20mm profile of 6082, there are no distinct grain boundaries.

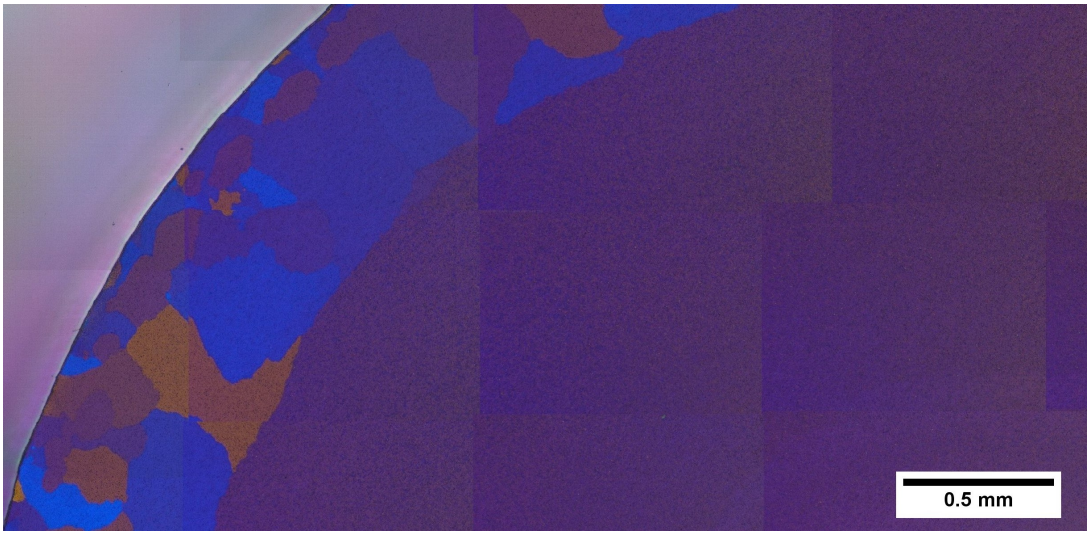

(a) Ø10mm

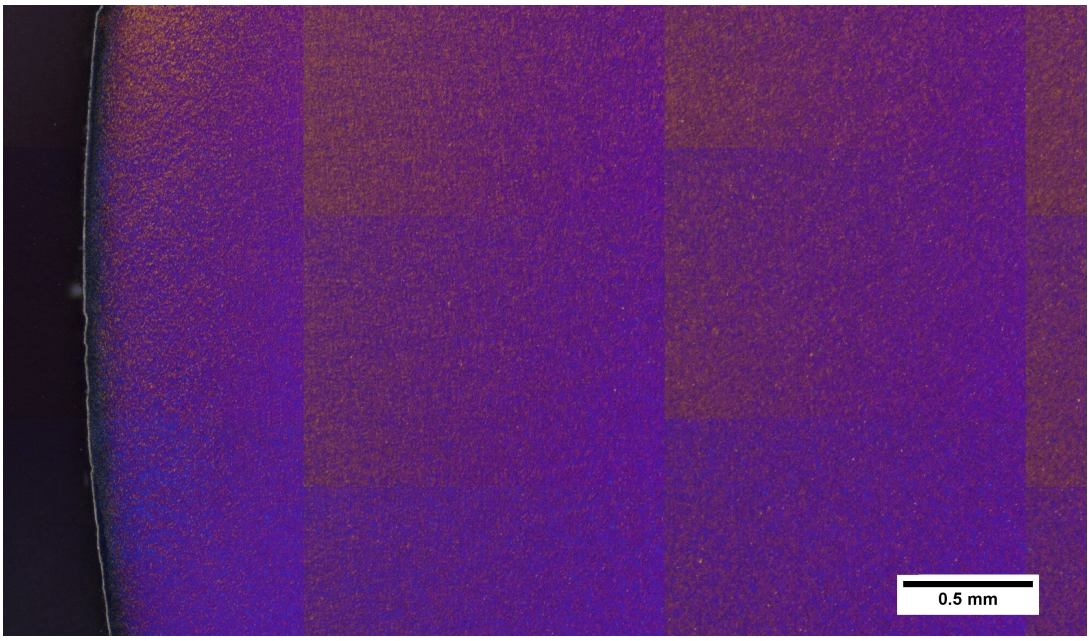

(b) Ø20mm

Fig. 4.1.5. Polarised light illumination and 5x magnification of transverse cross-section of 6082.

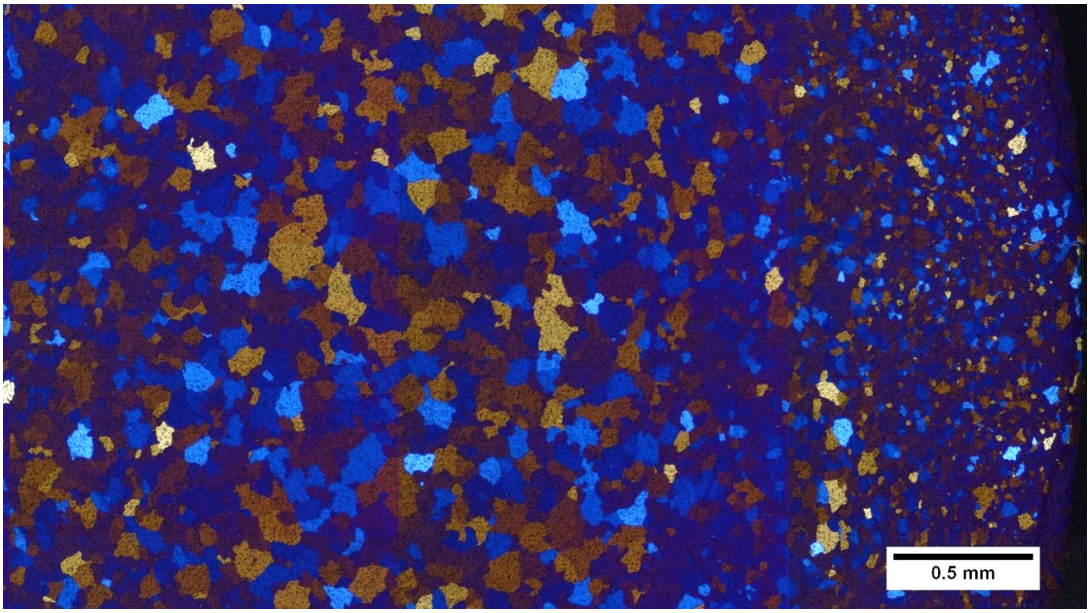

(a) Ø10mm

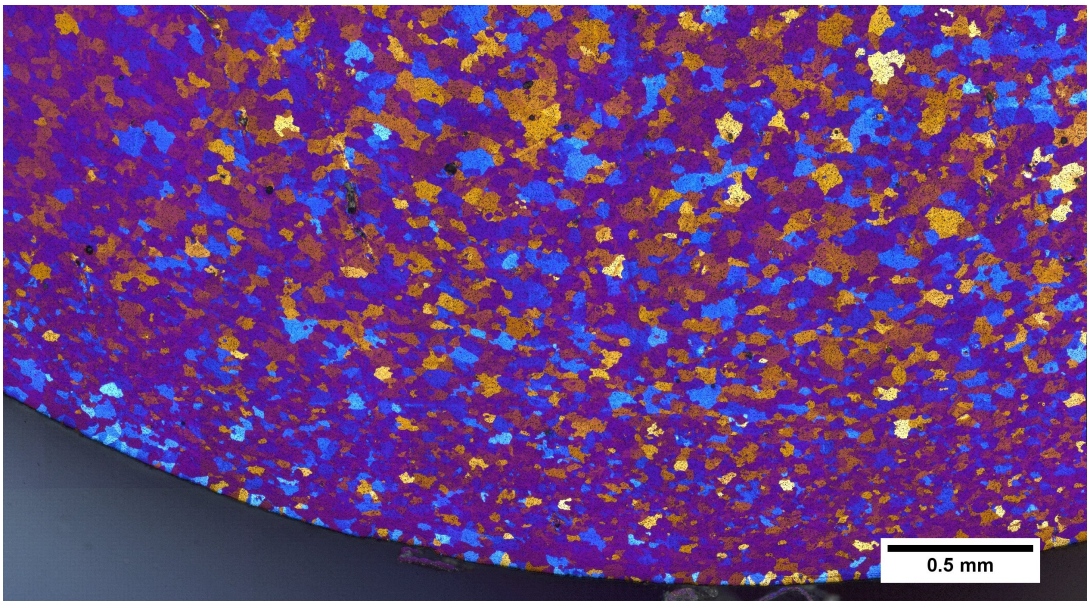

(b) Ø20mm

Fig. 4.1.6. Polarised light illumination and 5x magnification of transverse cross-section of 5052.

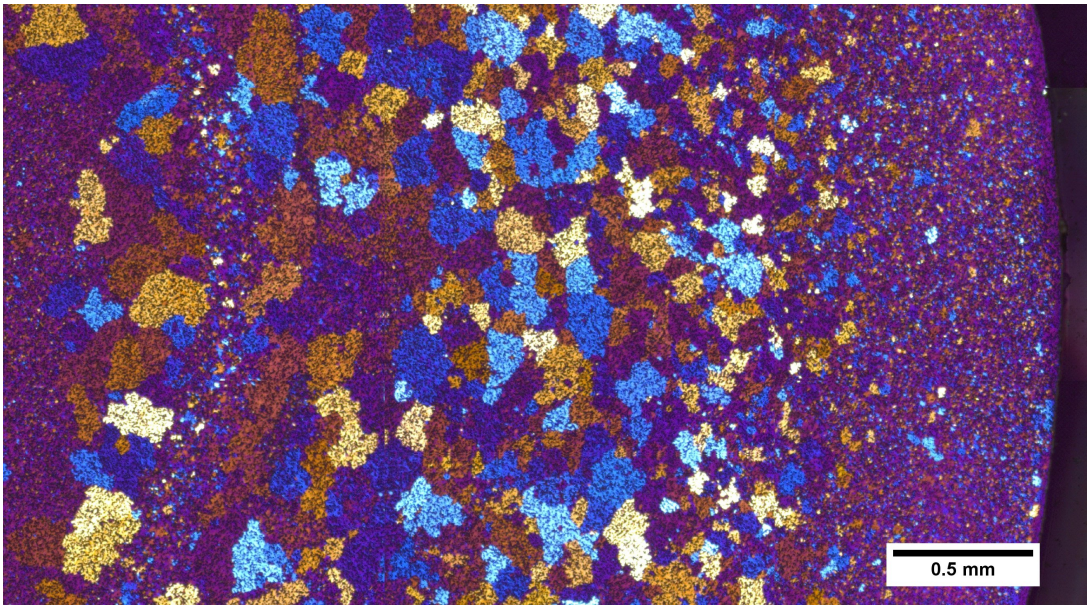

(a) Ø10mm

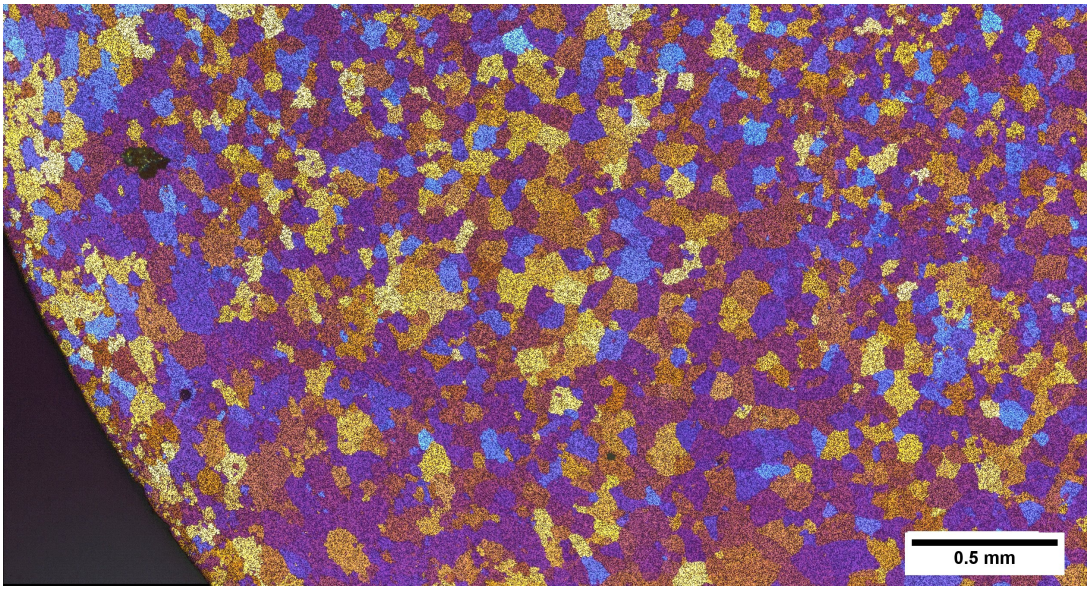

(b) Ø20mm

Fig. 4.1.7. Polarised light illumination and 5x magnification of transverse cross-section of Al-9Si-2Cu.

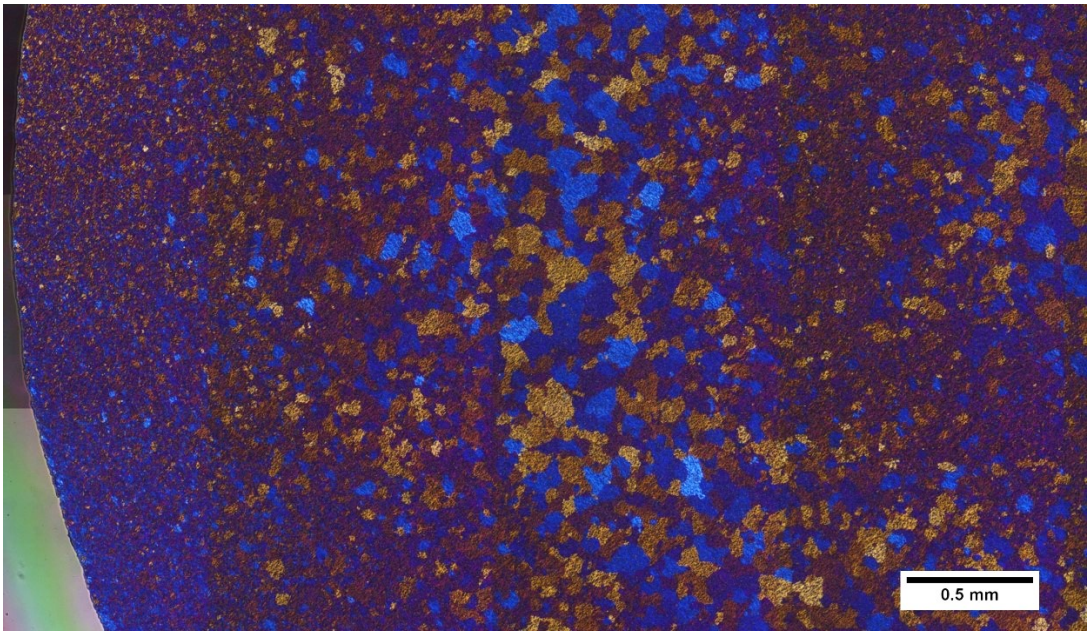

(a) Ø10mm

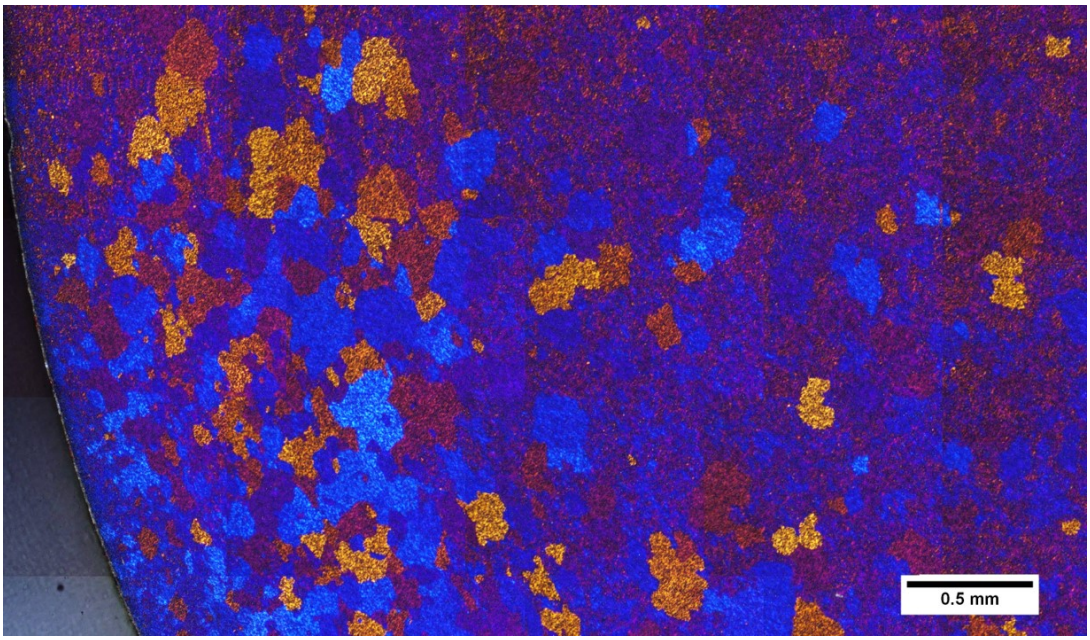

(b) Ø20mm

Fig. 4.1.8. Polarised light illumination and 5x magnification of transverse cross-section of Al-9Si-0.3Mg.

Polarized light illumination micrographs of the longitudinal cross-sections are given in Figure (4.1.9) through Figure (4.1.12). The grain structure of these is similar to the transverse cross-sections, but the grains are elongated in the extrusion direction. The longitudinal cross-section of Ø10mm Al-9Si-2Cu has alternating sections of small, round grains, and long elongated grains.

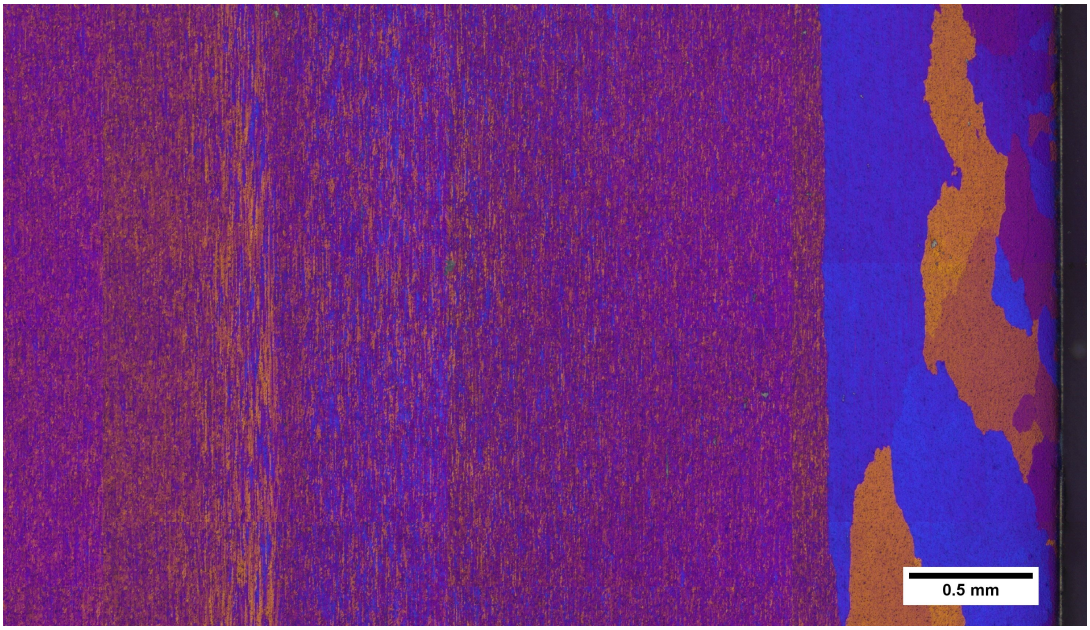

(a) Ø10mm

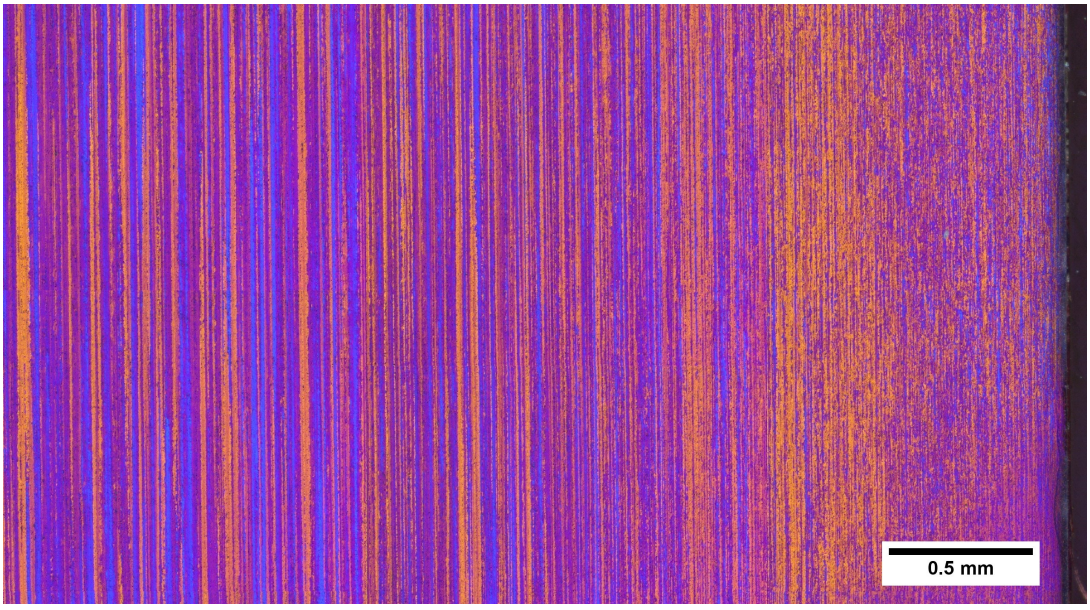

(b) Ø20mm

Fig. 4.1.9. Polarised light illumination and 5x magnification of longitudinal cross-section of 6082.

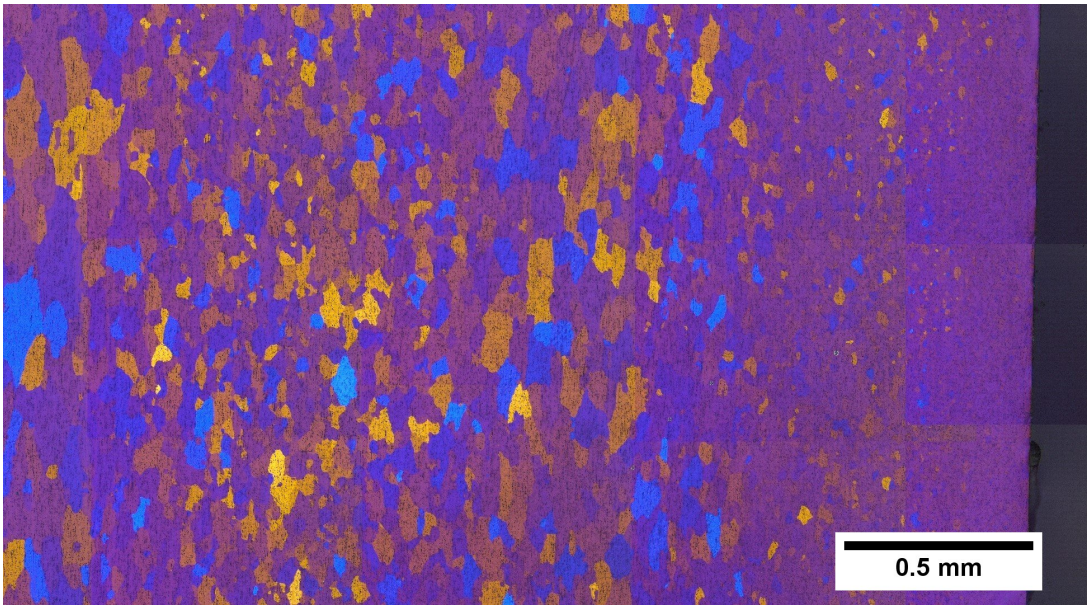

(a) Ø10mm

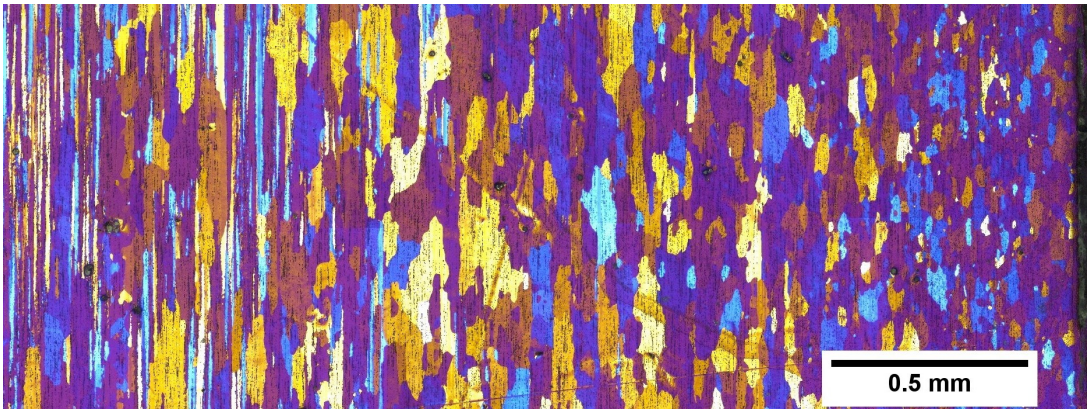

(b) Ø20mm

Fig. 4.1.10. Polarised light illumination and 5x magnification of longitudinal cross-section of 5052.

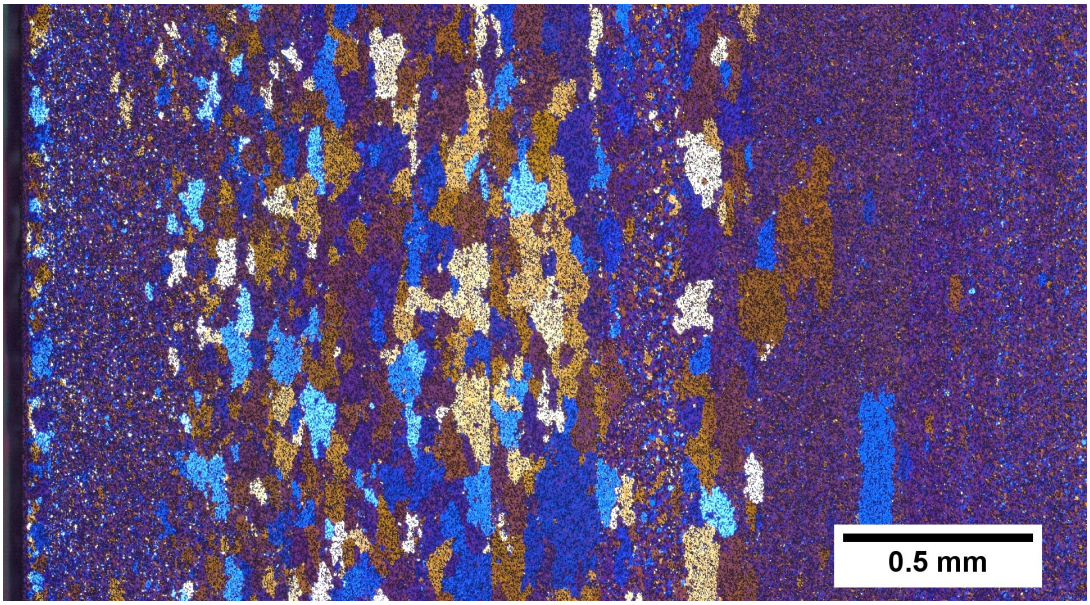

(a) Ø10mm

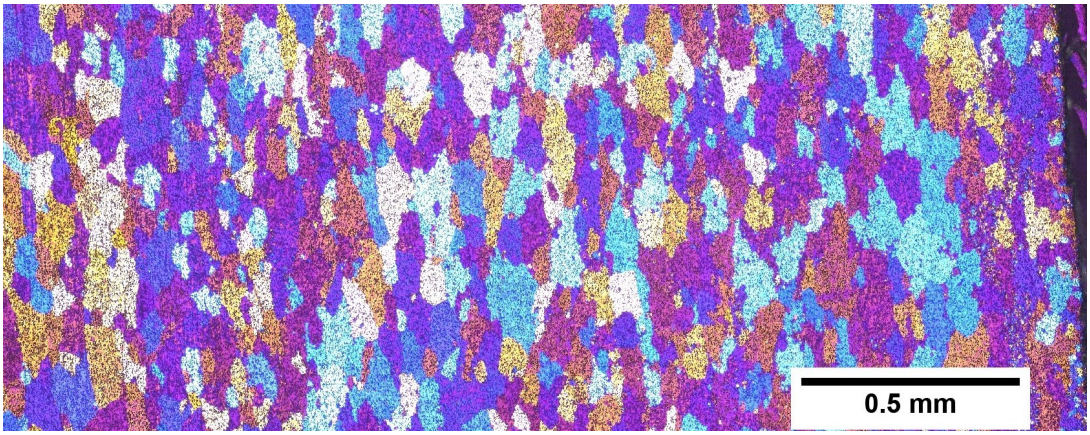

(b) Ø20mm

Fig. 4.1.11. Polarised light illumination and 5x magnification of longitudinal cross-section of Al-9Si-2Cu.

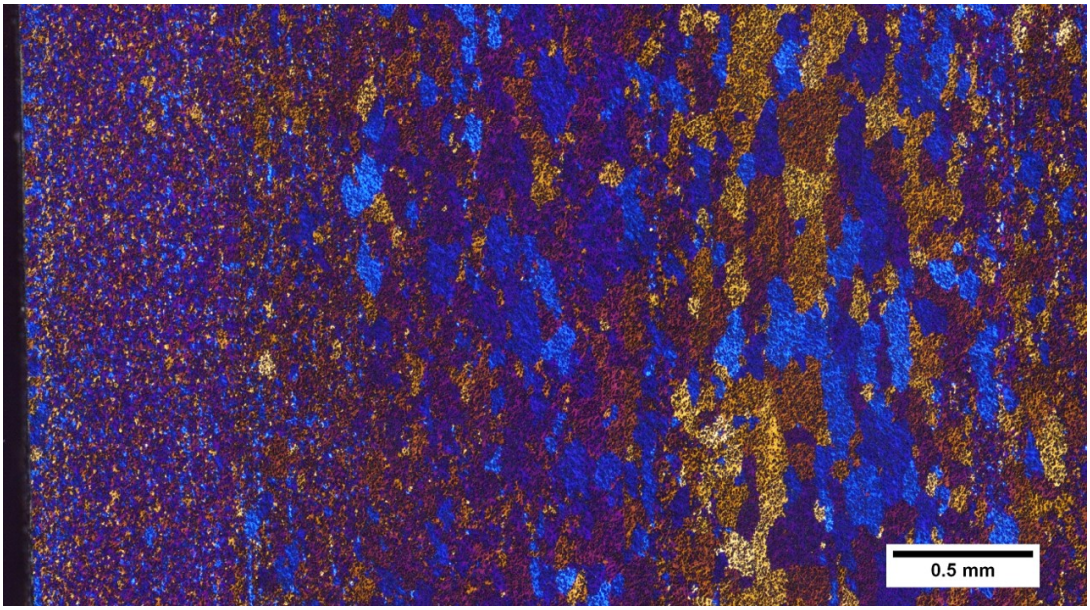

(a) Ø10mm

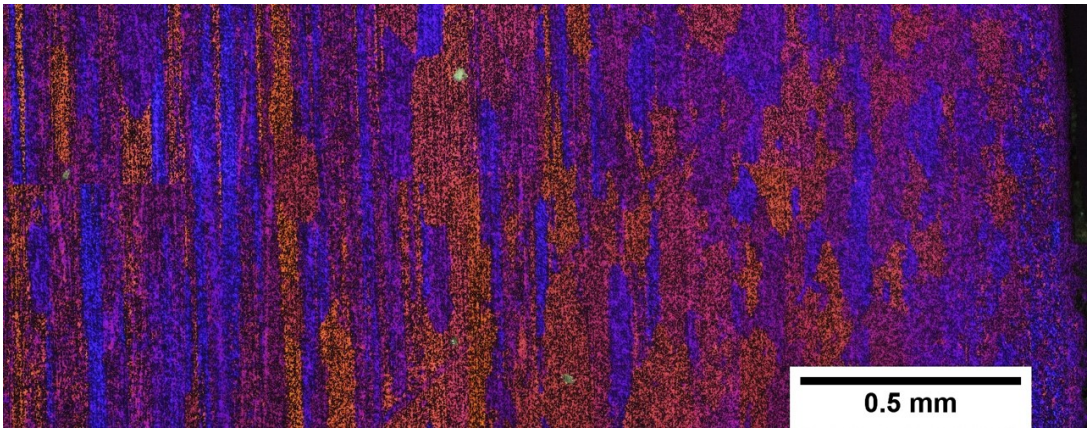

(b) Ø20mm

Fig. 4.1.12. Polarised light illumination and 5x magnification of longitudinal cross-section of Al-9Si-0.3Mg.

4.1.2 Hardness

The hardness of the ram-extruded profiles is summarized in Figure (4.1.13). The average hardness is marked with circular points and the standard deviation is indicated with vertical lines. Generally, the Ø20mm profiles achieve the highest hardness. Al-9Si-2Cu is the alloy with the highest measured hardness and 5052 the one with the lowest.

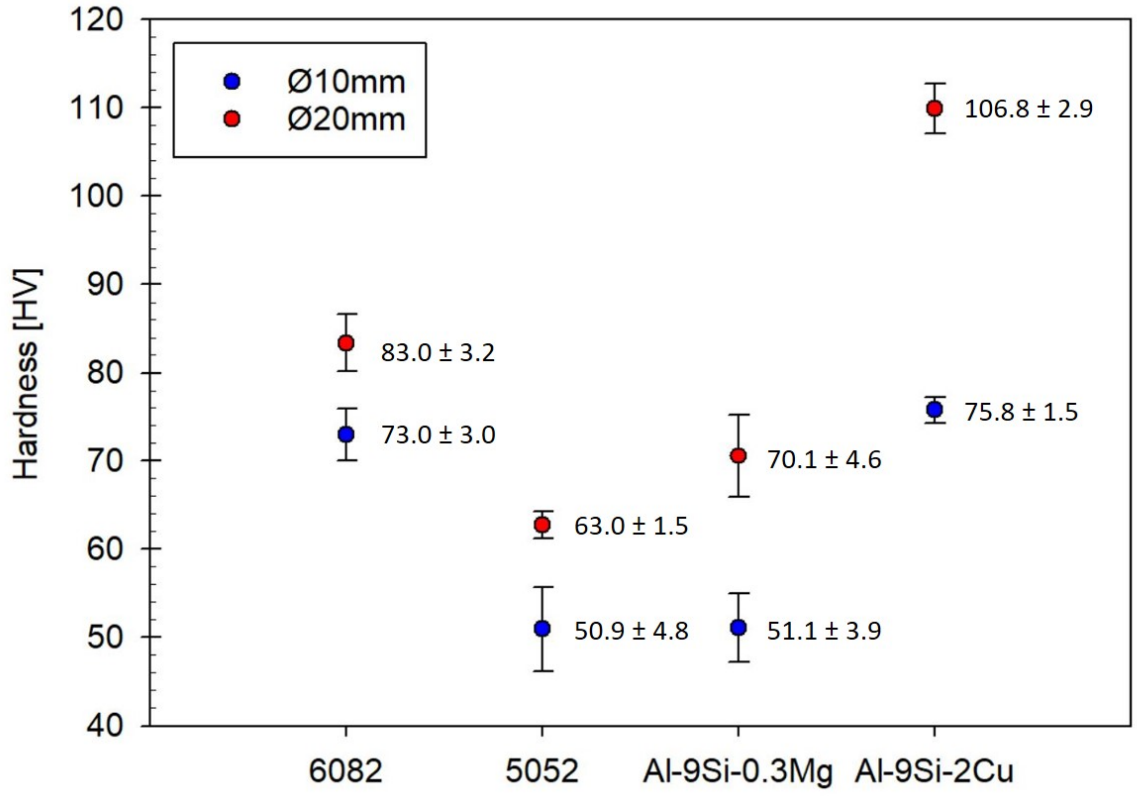

Fig. 4.1.13. Hardness of ram-extruded profiles.

4.1.3 Tensile Strength

The stress-strain curves of the ram-extruded Ø10mm and Ø20mm profiles are given in Figure (4.1.14) and Figure (4.1.15), respectively. Al-9Si-2Cu has the highest tensile strength but is also the least ductile alloy. On the other hand, 5052 has the lowest strength and the highest ductility.

One of the Ø20mm 6082 samples and one of the Ø20mm Al-9Si-0.3 Mg samples have lower strength than the rest of the samples of the same alloy. Visual inspection showed that these samples were damaged, which may have occurred during the machining of the samples.

All samples, except for Ø10mm Al-9Si-0.3Mg and Ø20mm 5052, were tested three times. The average values of tensile strength and total extension are given in Table (4.1.1). The damaged samples were not included in the calculation of average values.

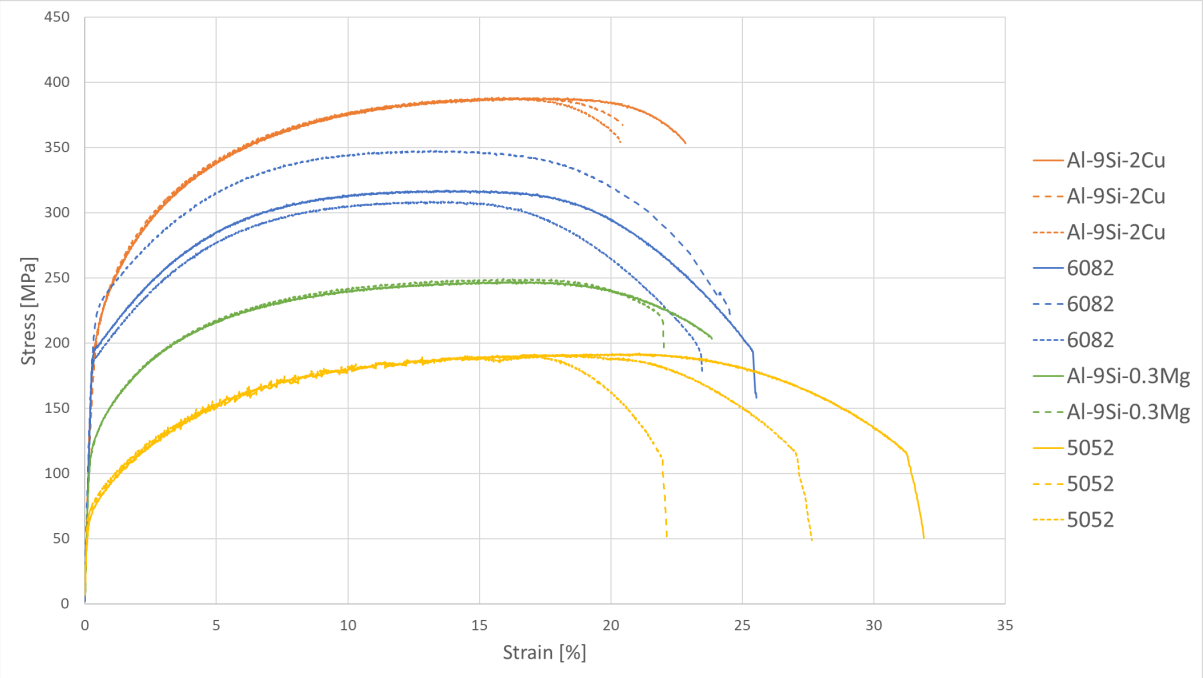

Fig. 4.1.14. Stress-strain curve of ram-extruded Ø10mm profiles.

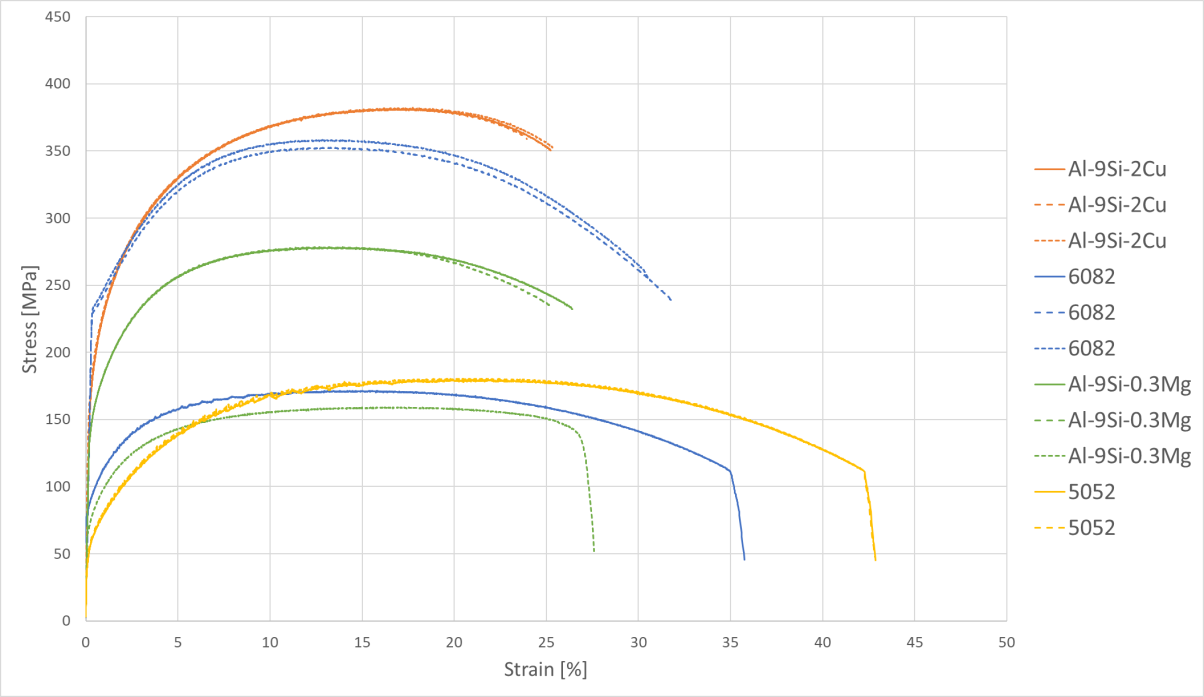

Fig. 4.1.15. Stress-strain curve of ram-extruded Ø20mm profiles.

Tab. 4.1.1. Average values of tensile strength and total extension ± standard deviation of ram-extruded profiles.

Alloy	Ultimate tensile strength, σ_{UTS} [MPa]	Total extension at maximum force, A_{gt} [%]	Total extension at fracture, A_f [%]
Ø10mm			
6082	324.3 ± 20.3	13.5 ± 0.3	24.5 ± 1.0
5052	191.1 ± 1.1	18.7 ± 2.1	27.2 ± 4.9
Al-9Si-2Cu	388.1 ± 0.2	16.2 ± 0.8	21.2 ± 1.4
Al-9Si-0.3Mg	248.1 ± 1.3	16.1 ± 0.3	22.9 ± 0.6
Ø20mm			
6082	355.5 ± 4.0	13.4 ± 0.7	32.7 ± 2.7
5052	180.2 ± 0.6	20.3 ± 0.8	42.9 ± 0.0
Al-9Si-2Cu	381.6 ± 0.5	16.9 ± 0.8	24.8 ± 0.8
Al-9Si-0.3Mg	278.5 ± 0.4	14.1 ± 1.6	26.4 ± 1.1

4.2 Characterization of Rolled Profiles

4.2.1 Rib Geometry

Figures (4.2.1) and (4.2.2) shows the Ø10mm and Ø20 mm aluminium profiles after rolling, respectively.The geometry of the rolled profiles compared to standard steel reinforcement is summarized in Table (4.2.1). The height of the ribs does not appear to be dependent on the alloy. The height is significantly lower than standard steel reinforcement.

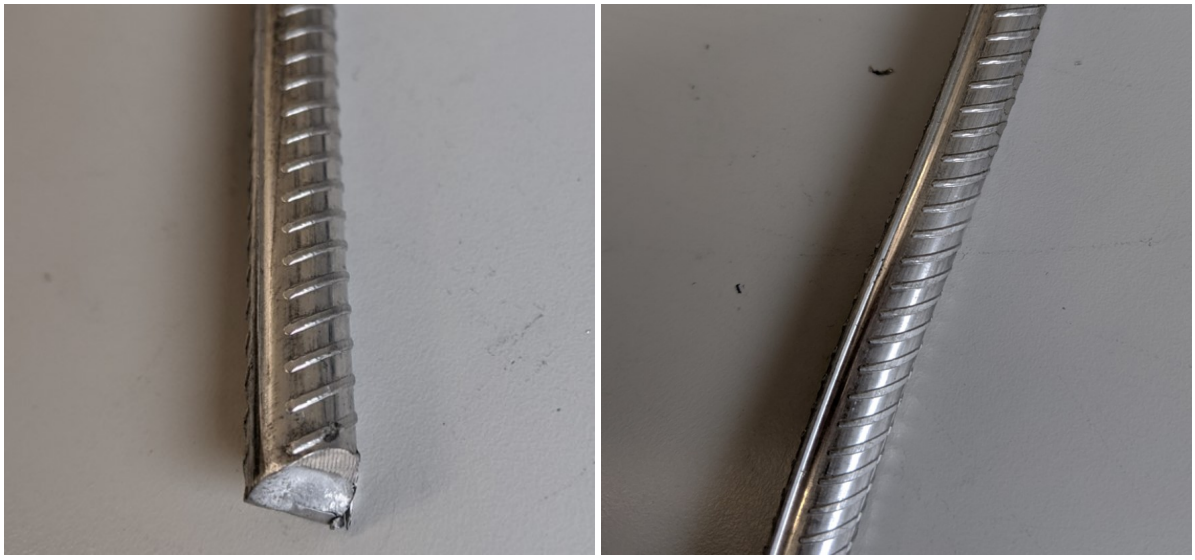

Fig. 4.2.1. Geometry of rolled Ø10mm profiles.

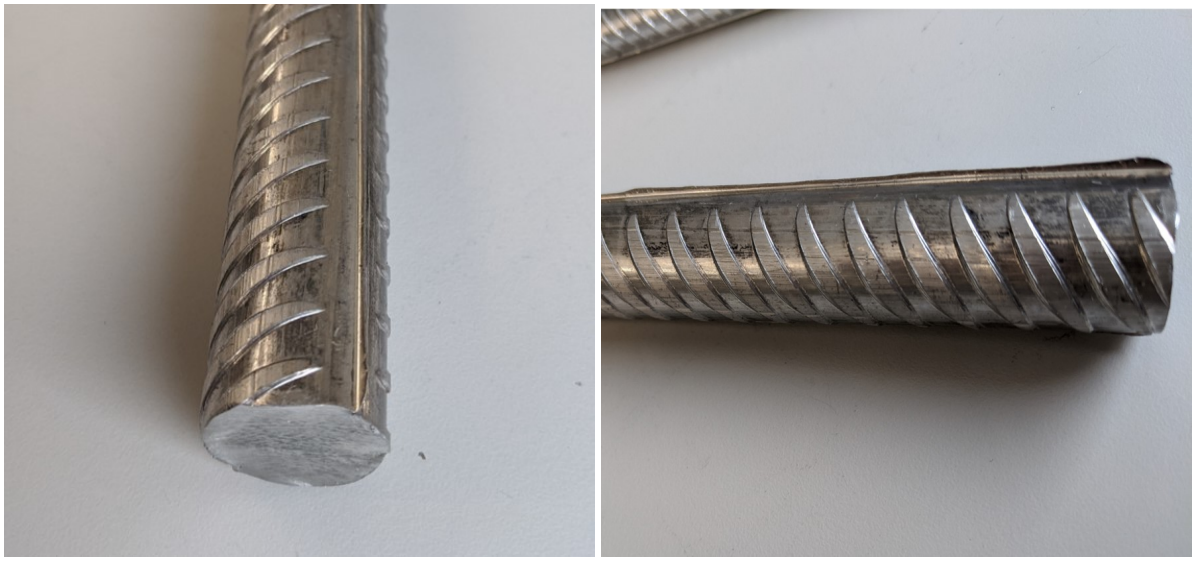

Fig. 4.2.2. Geometry of rolled Ø20mm profiles.

Tab. 4.2.1. Rib geometry of aluminium profiles after rolling compared to standard steel reinforcement. Standard deviation is indicated with ±.

Alloy	Inner diameter (excl. ribs) [mm]	Outer diameter (incl. ribs) [mm]	Rib height, [mm]
Ø10mm			
Reference steel*	-	-	0.3 to 1.5
6082	9.65 ± 0.05	9.96 ± 0.04	0.15 ± 0.03
5052	9.65 ± 0.13	9.98 ± 0.03	0.14 ± 0.07
Al-9Si-2Cu	9.69 ± 0.07	9.99 ± 0.02	0.14 ± 0.05
Al-9Si-0.3Mg	9.59 ± 0.07	9.94 ± 0.04	0.18 ± 0.02
Ø20mm			
Reference steel*	-	-	0.6 to 3.0
6082	18.78 ± 0.05	19.68 ± 0.10	0.45 ± 0.07
5052	18.63 ± 0.06	19.55 ± 0.08	0.46 ± 0.06
Al-9Si-2Cu	18.71 ± 0.11	19.60 ± 0.06	0.45 ± 0.05
Al-9Si-0.3Mg	18.65 ± 0.03	19.56 ± 0.05	0.46 ± 0.04

* Based on NS-EN 10080:2005. See Table (2.8.1).

4.2.2 Hardness

The hardness of the rolled profiles is presented in two ways; (1) average hardness compared to average hardness before rolling, and (2) hardness profile from edge to center. The first one is summarized in Figure (4.2.3) and Figure (4.2.4). As can be seen in the figure, the average hardness of the Ø10mm profiles increased with rolling. The increase differs from alloy to alloy and is most significant for 6082. Contrarily, the hardness of the extruded Ø20mm profiles was not significantly changed by rolling, except for Al-9Si-0.3Mg.

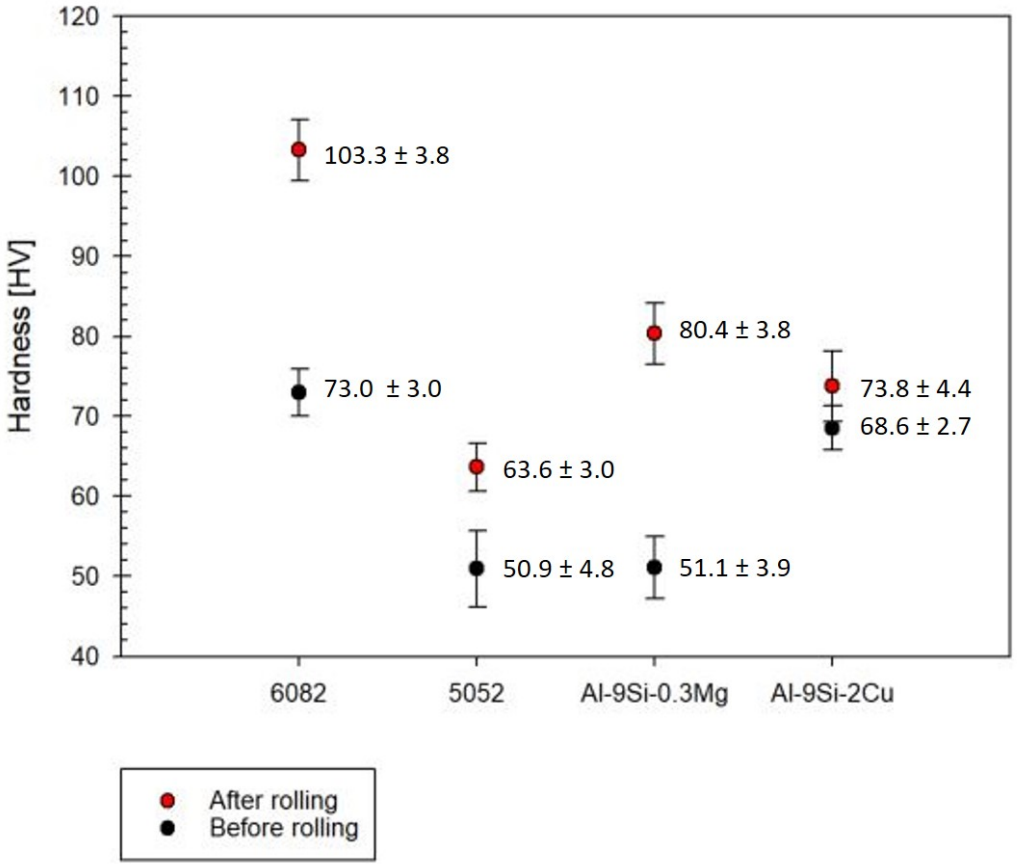

Fig. 4.2.3. Average hardness of Ø10mm profiles before and after rolling.

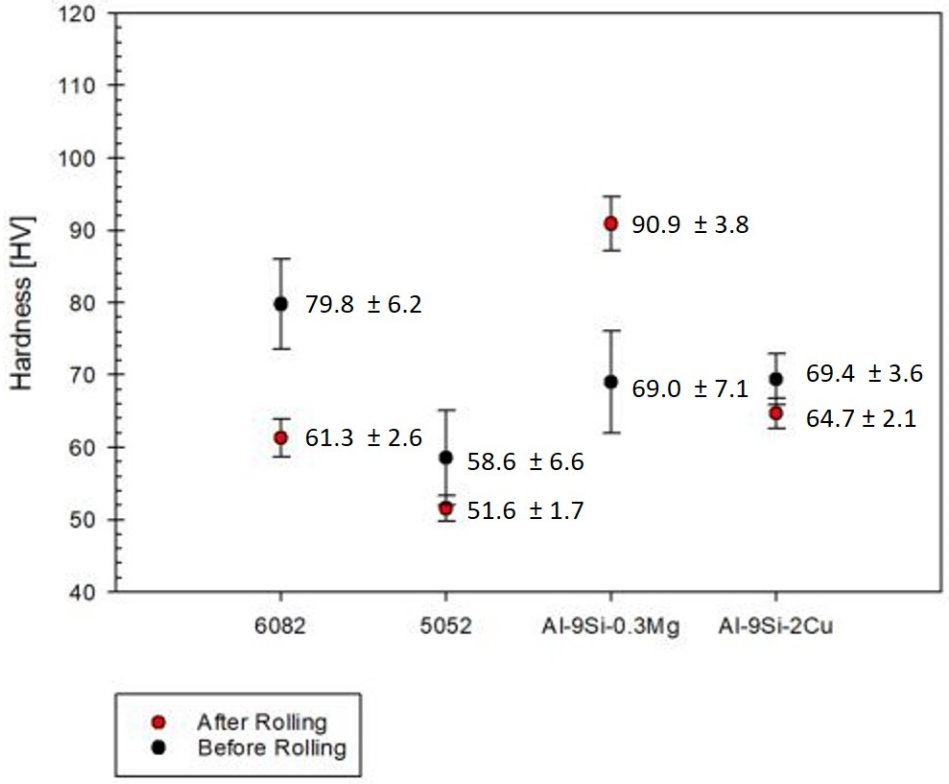

Fig. 4.2.4. Average hardness of Ø20mm profiles before and after rolling.

The hardness was mostly constant across the transverse and longitudinal cross-sections. In Figure (4.2.5), the hardness profiles of the Ø10mm longitudinal cross-sections are given. As can be seen in the figure, there is little change in the hardness. The remaining hardness profiles are presented in Appendix E.

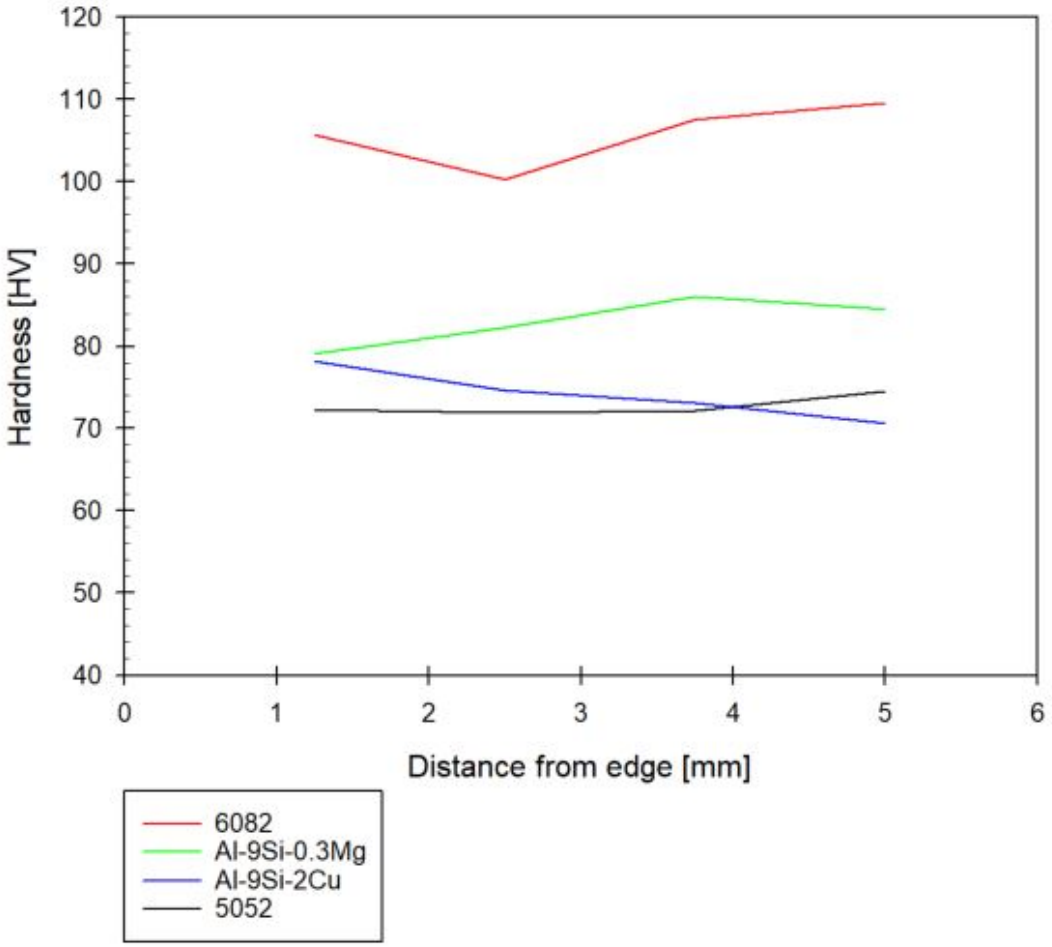

Fig. 4.2.5. Hardness profile of Ø10mm longitudinal cross-sections.

4.3 Heat Treatment of Extruded Profiles

After extrusion and rolling, some of the aluminium profiles were heat treated. The heat treatment of Al-9Si-2Cu and Al-9Si-0.3Mg were based on the results presented in this section.

4.3.1 Aging Curve

The aging curve of Al-9Si-0.3Mg can be found in Figure (4.3.1). The peak hardness is achieved after 8 hours at 120.6 HV ± 4.0 HV. The aging curve of Al-9Si-2Cu is given in Figure (4.3.2). It reaches a peak hardness after 12 hours at 150.5 HV ± 8.0 HV.

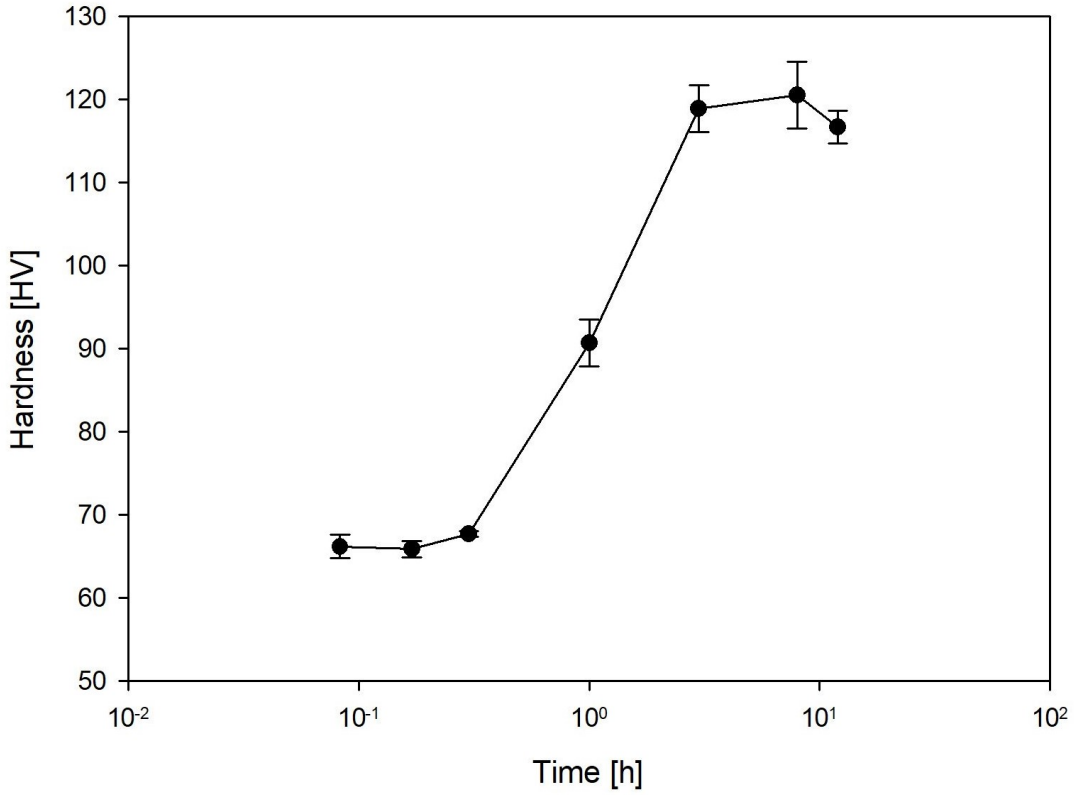

Fig. 4.3.1. Aging curve of Al-9Si-0.3Mg

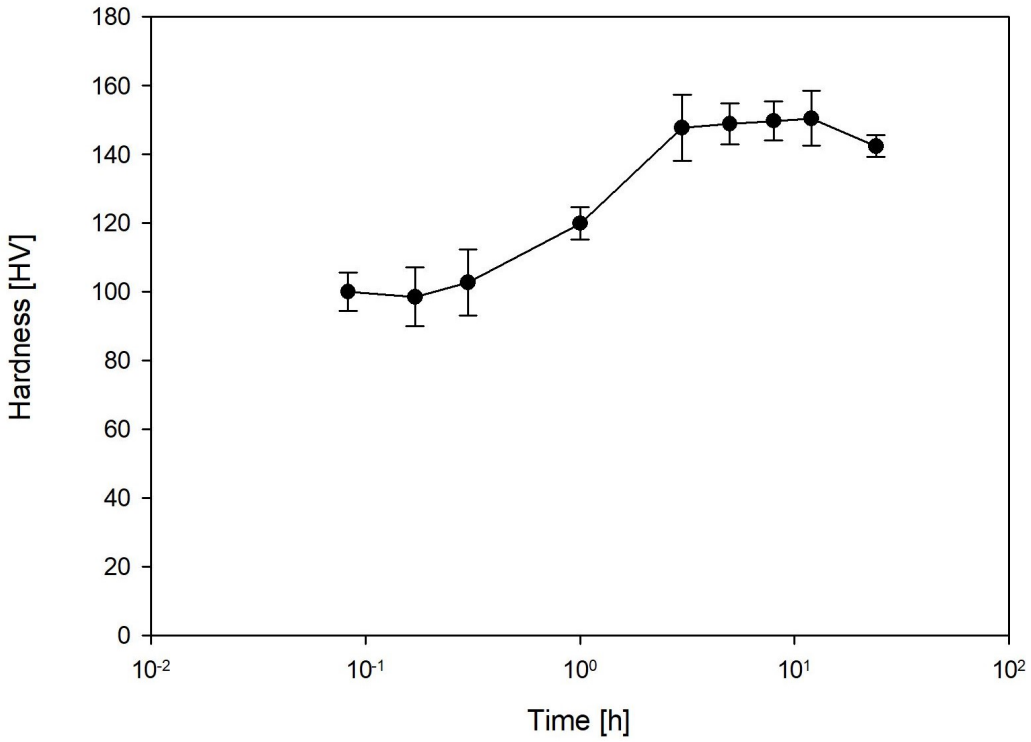

Fig. 4.3.2. Aging curve of Al-9Si-2Cu

4.3.2 Tensile Tests

The stress-strain curves of the heat-treated samples are given Figure (4.3.3) and Figure (4.3.4) for Ø10mm and Ø20mm, respectively. The alloys were heat treated to peak hardness as described in Table (3.6.1). Each alloy was tensile tested twice. Average values ± standard deviation are given in Table (4.3.1).

The difference between Ø10mm T6-6082 and Ø20mm T6-6082 is quite large. There was no damage to the Ø20mm samples that could explain this difference. Nothing particular occurred during the testing either. Whatever caused the difference must have occurred before the testing. The tensile properties of Ø10mm and Ø20mm Al-9Si-2Cu and Al-9Si-0.3Mg were quite similar. T6-Al-9Si-2Cu achieves the highest tensile strength, but is the least ductile.

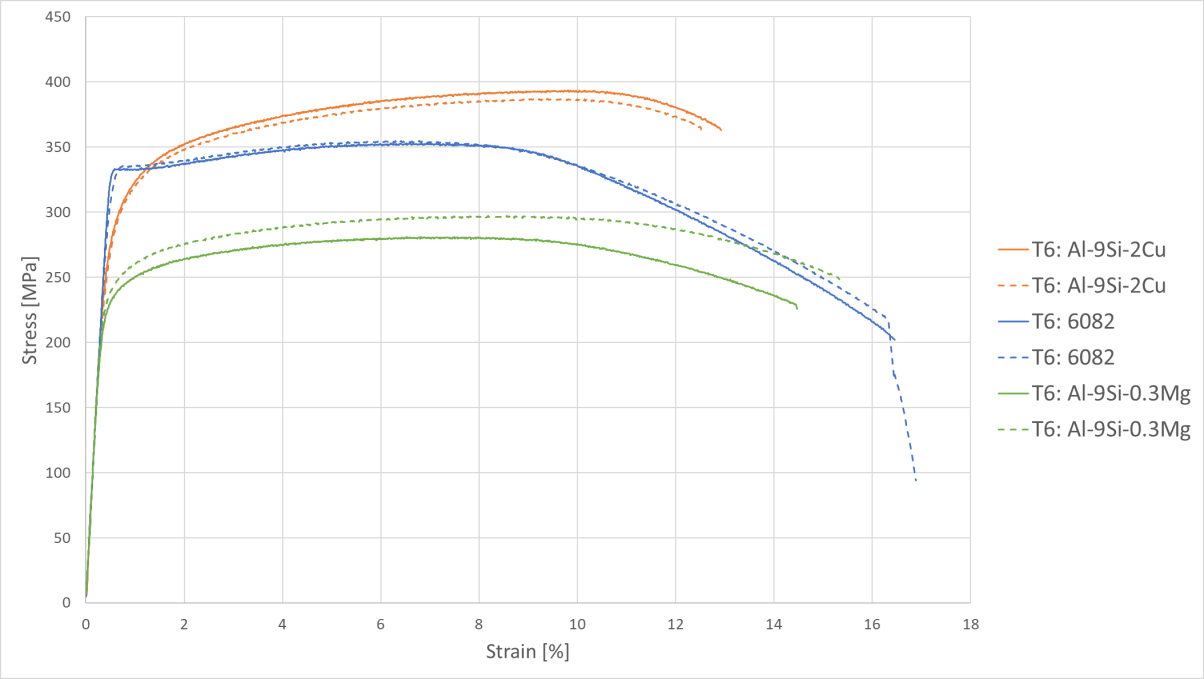

Fig. 4.3.3. Stress-strain curve of heat-treated Ø10mm profiles.

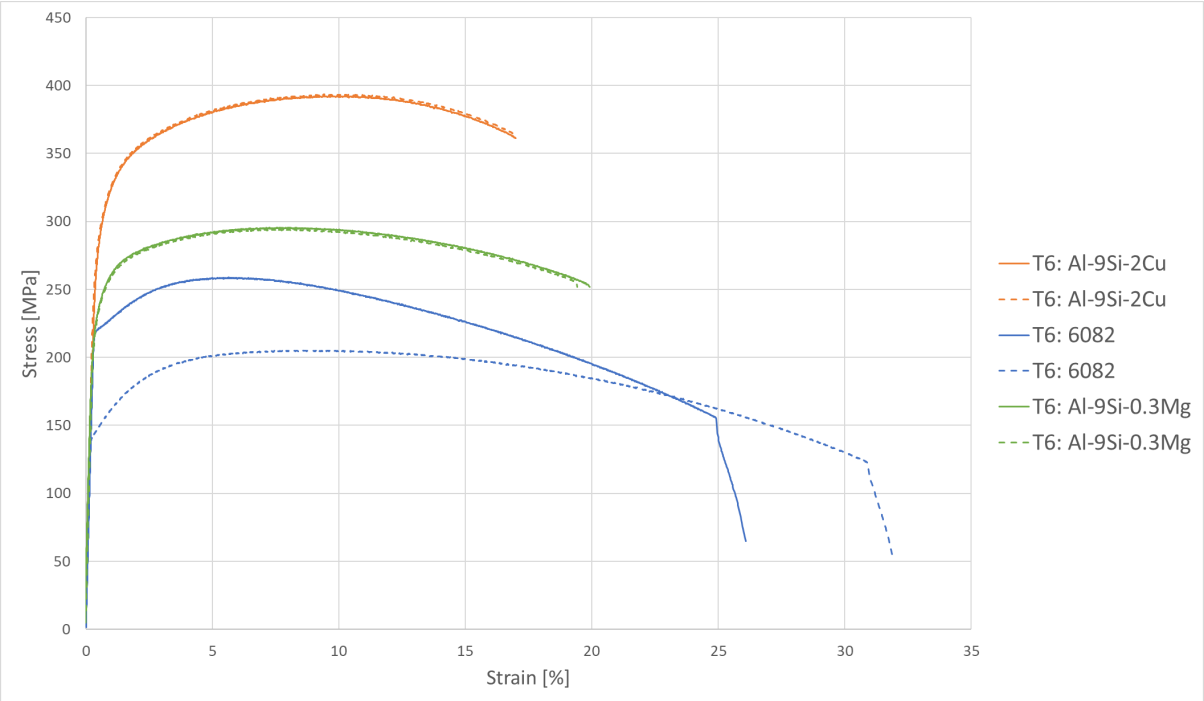

Fig. 4.3.4. Stress-strain curve of heat-treated Ø20mm profiles.

Tab. 4.3.1. Average values of tensile strength and total extension ± standard deviation of heat-treated samples.

Alloy	Ultimate tensile strength, σ_{UTS} [MPa]	Total extension at maximum force, A_{gt} [%]	Total extension at fracture, A_f [%]
Ø10mm			
6082	353.7 ± 1.4	6.3 ± 0.2	16.7 ± 0.3
Al-9Si-2Cu	390.2 ± 4.5	9.5 ± 0.1	12.7 ± 0.3
Al-9Si-0.3Mg	289.0 ± 11.5	7.3 ± 0.7	14.9 ± 0.6
Ø20mm			
6082	232.1 ± 37.8	7.4 ± 2.5	29.0 ± 4.1
Al-9Si-2Cu	393.0 ± 0.9	9.7 ± 0.4	17.0 ± 0.0
Al-9Si-0.3Mg	294.9 ± 0.8	7.6 ± 0.0	19.7 ± 0.3

4.3.3 Grain Structure Characterization by LOM

The heat treatment was also applied to Ø10mm aluminium samples that were used for hydrogen measurements. These samples were examined in LOM.

Bright-field illumination micrographs of the transverse cross-section of the heat-treated samples are given in Figure (4.3.5) through Figure (4.3.7). 6082 have a few particles of varying sizes distributed on the surface. Al-9Si-2Cu and Al-9Si-0.3Mg have many particles with similar size on the surface. The particles on Al-9Si-0.3Mg appear to be smaller than those on Al-9Si-2Cu.

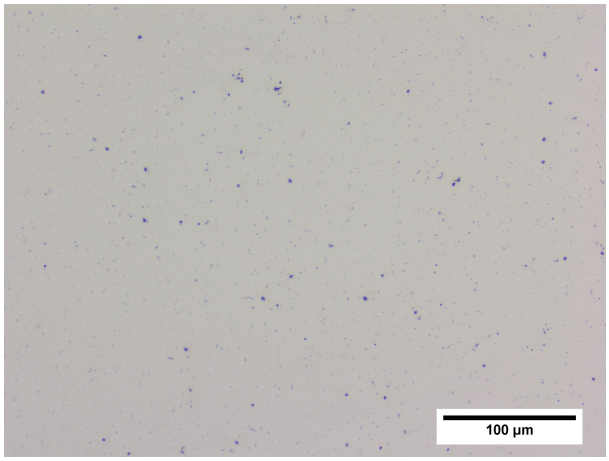

Fig. 4.3.5. Bright-field illumination and 20x magnification of transverse cross-section of heat-treated 6082.

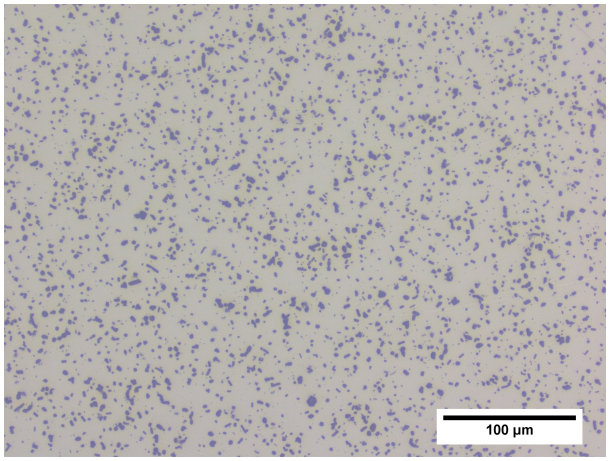

Fig. 4.3.6. Bright-field illumination and 20x magnification of transverse cross-section of heat-treated Al-9Si-2Cu.

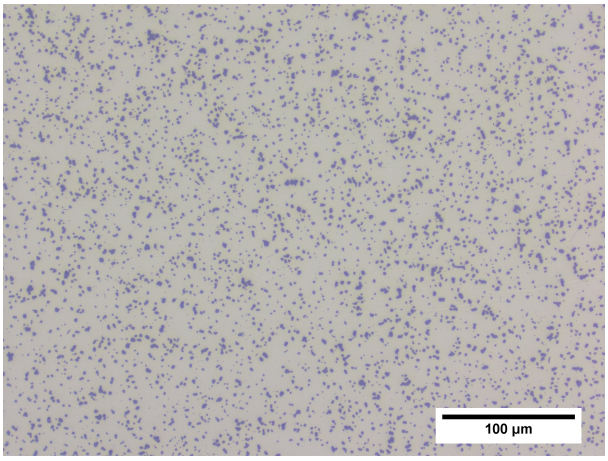

Fig. 4.3.7. Bright-field illumination and 20x magnification of transverse cross-section of heat-treated Al-9Si-0.3Mg.

Polarized light illumination micrographs of the transverse and longitudinal cross-section of the heat-treated samples are given in Figure (4.3.8) through Figure (4.3.10). The transverse

cross-section of 6082 (Figure (4.3.8a)) has large grains on the edge and no distinct grain boundaries in the center. The longitudinal cross-section has a similar grain structure, but the grains in the center are thin and elongated. The grain structure of Al-9Si-2Cu (Figure (4.3.9)) and Al-9Si-0.3Mg (Figure (4.3.10)) fine at the edges and gets coarser towards the centre. The longitudinal cross-sections have slightly more elongated grains than the transverse cross-sections.

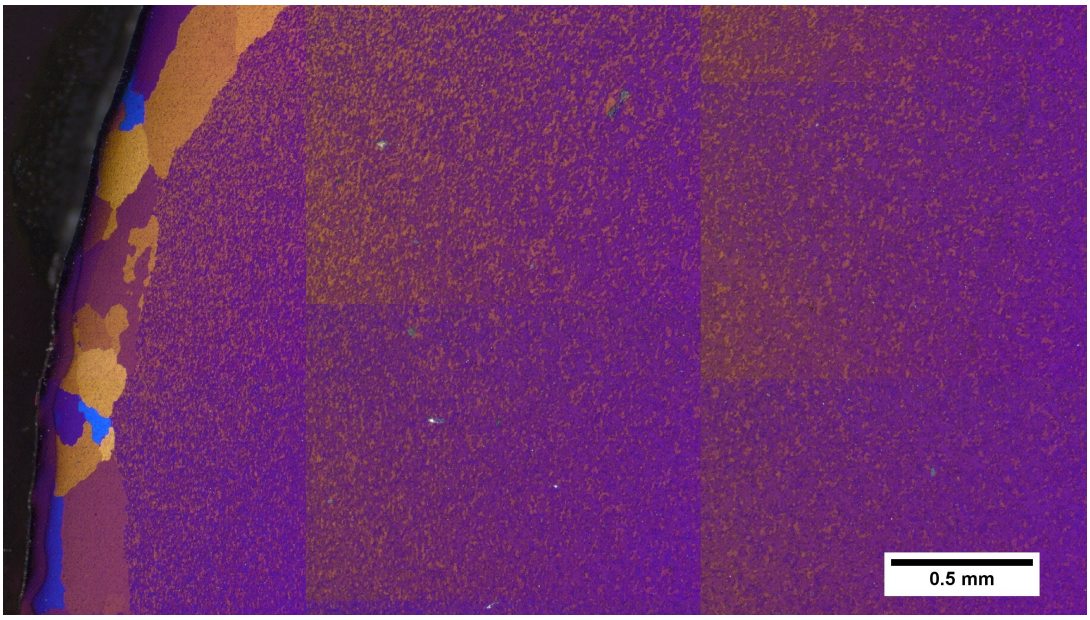

(a) Transverse cross-section.

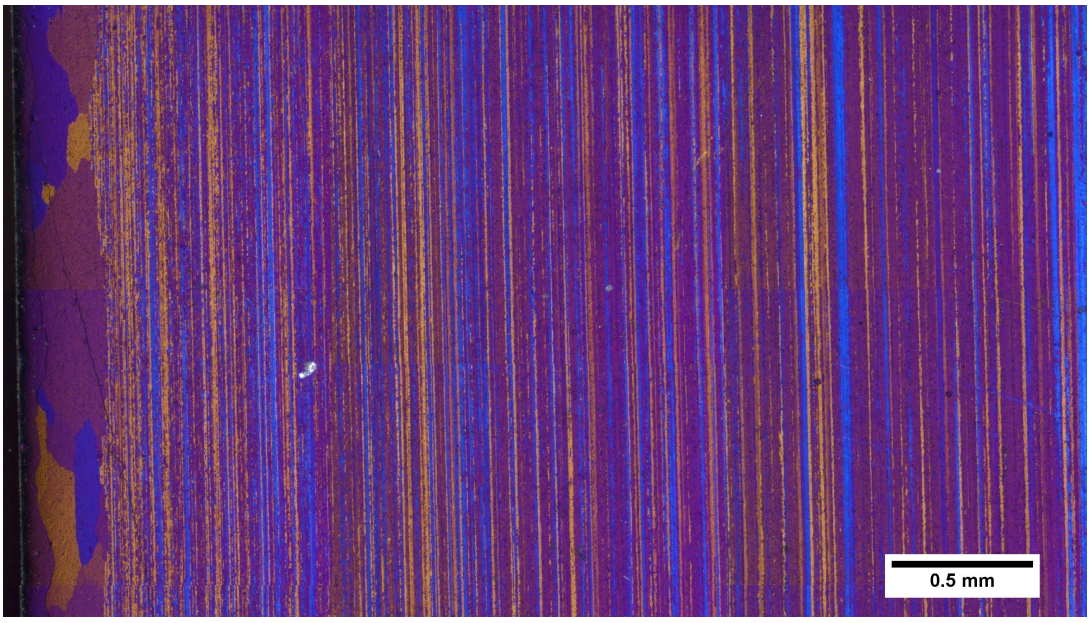

(b) Longitudinal cross-section.

Fig. 4.3.8. Polarised light illumination and 5x magnification of heat-treated 6082.

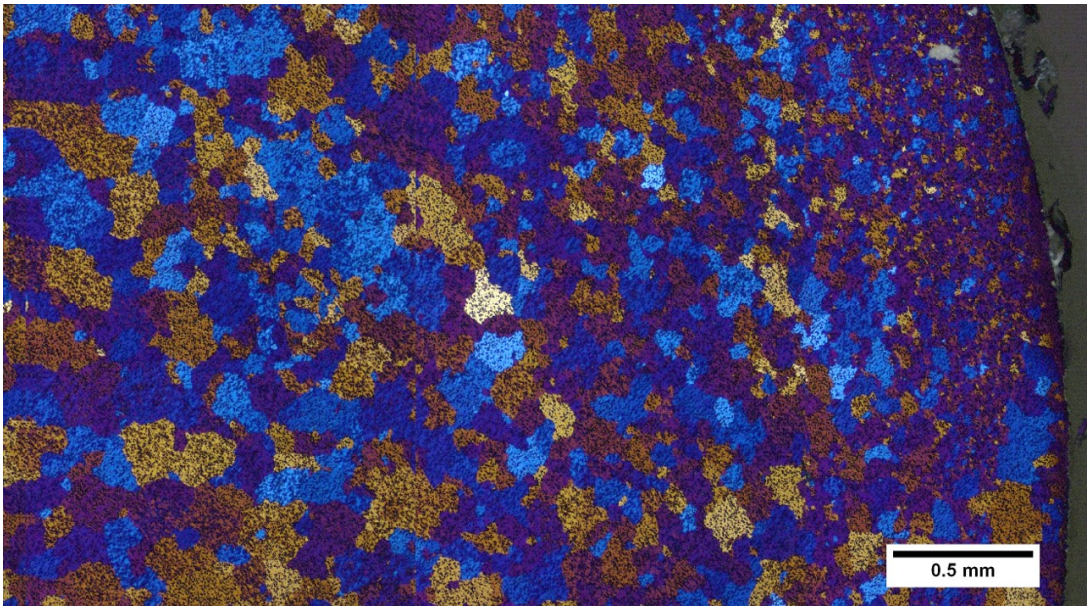

(a) Transverse cross-section.

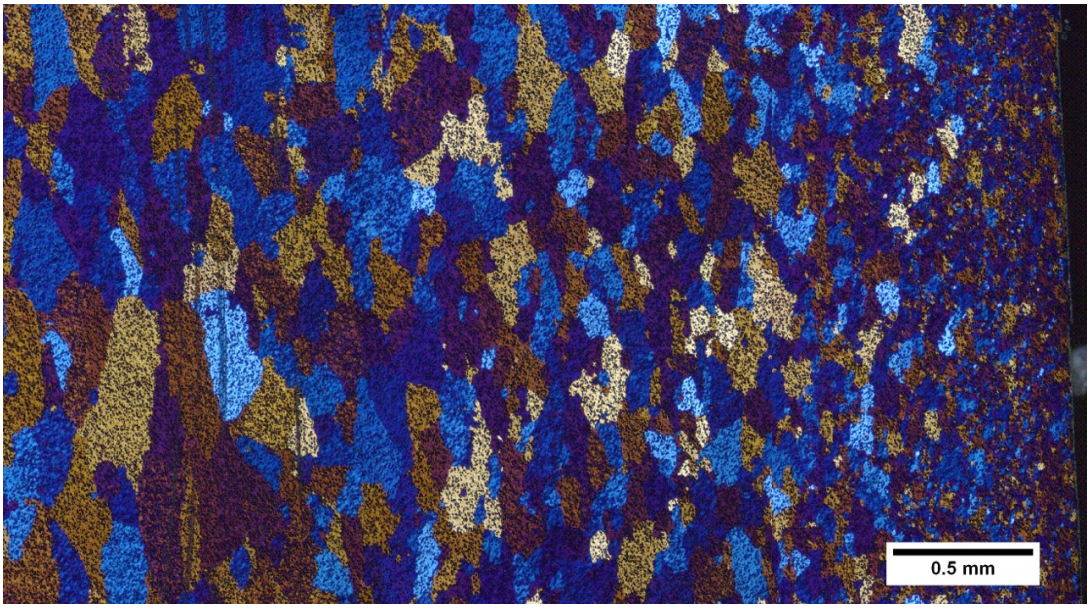

(b) Longitudinal cross-section.

Fig. 4.3.9. Polarised light illumination and 5x magnification of heat-treated Al-9Si-2Cu.

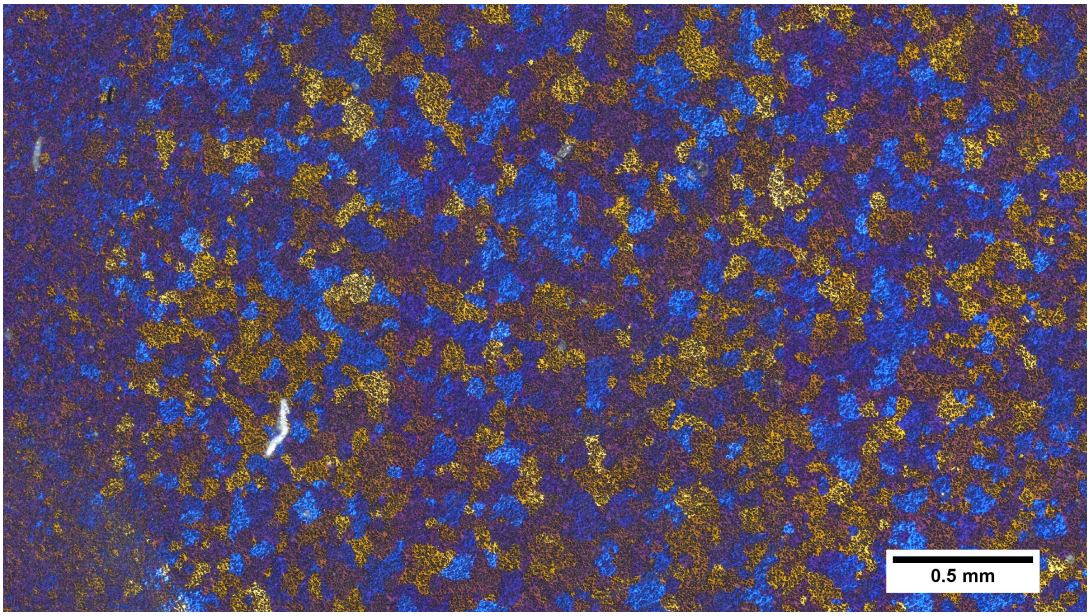

(a) Transverse cross-section.

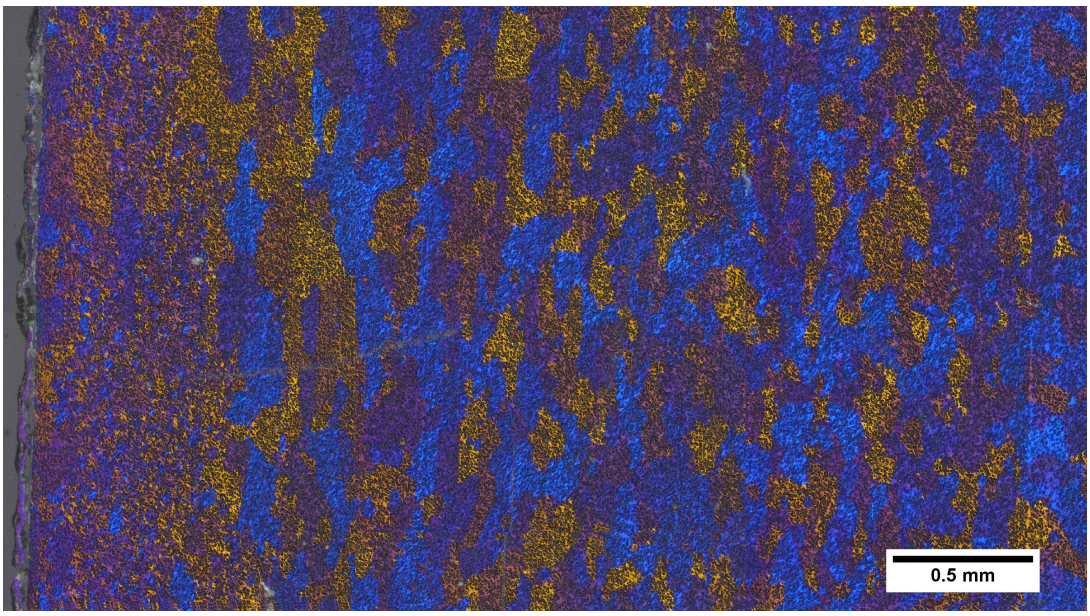

(b) Longitudinal cross-section.

Fig. 4.3.10. Polarised light illumination and 5x magnification of heat-treated Al-9Si-0.3.

4.3.4 Particle Characterization by SEM

When the aluminium alloys are heat treated, small particles precipitate. In an attempt to characterize these particles, the heat-treated samples were examined in SEM. EDS analysis was used to find the composition of selected particles. These were chosen so that particles of different shapes and sizes was analysed. Multiple analyses were conducted, but they mostly yielded the same results. In this section, one EDS analysis per heat-treated alloy is presented.

An SEM micrograph of the heat-treated 6082-alloy is given in Figure (4.3.11a). Large white particles and small gray particles can be observed. The particles used in the EDS analysis are marked in Figure (4.3.11b), and the results are summarized in Table (4.3.2). Al, Si, and Mn appear to be the main constituents in the particles.

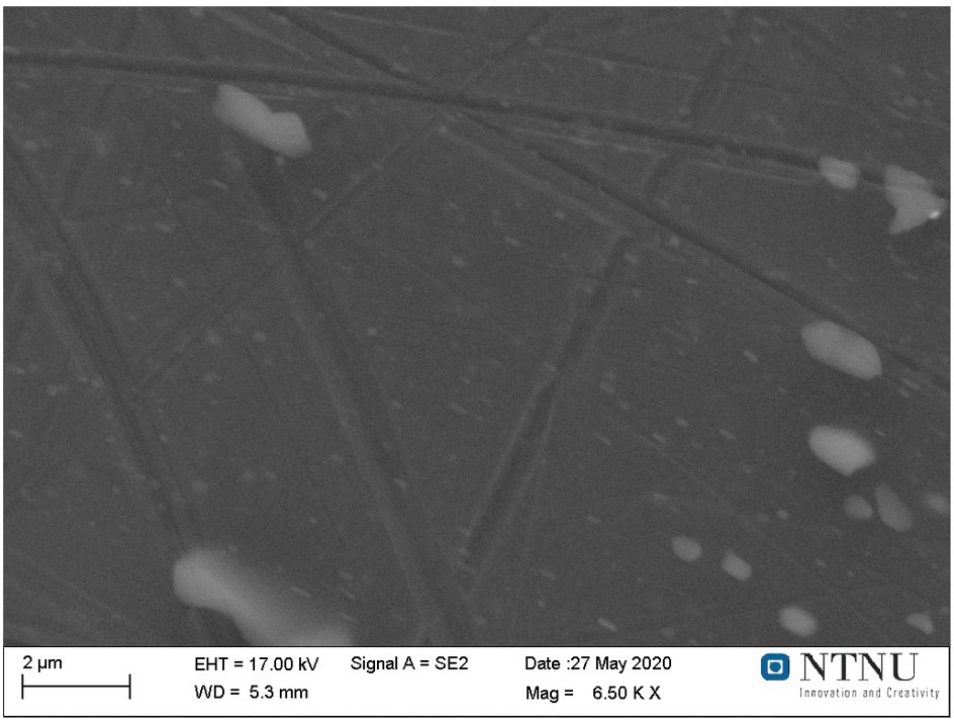

(a) SEM micrograph at 6500x magnification.

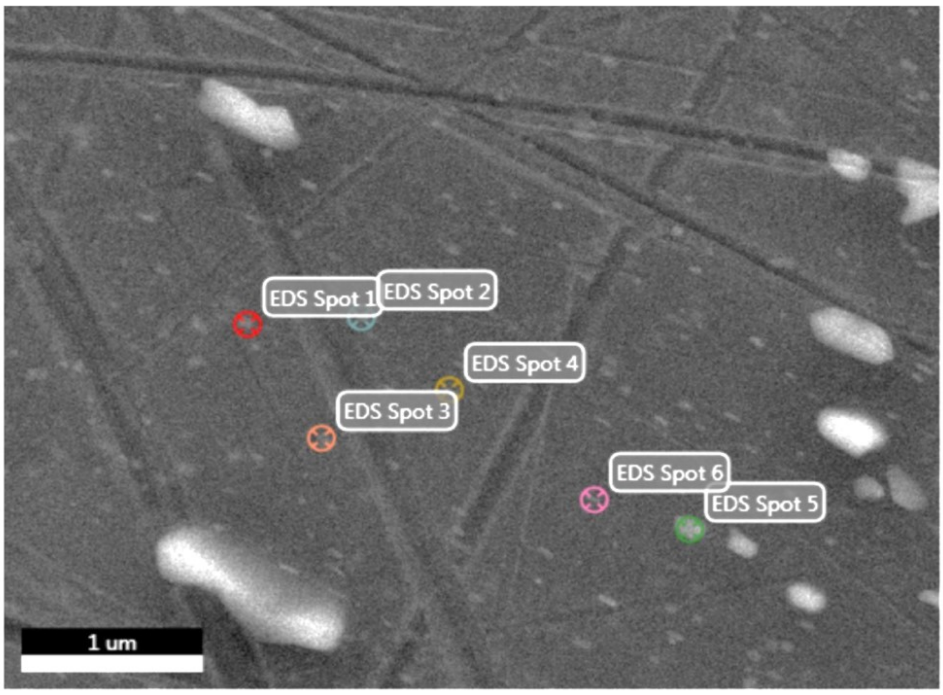

(b) Spots used for EDS analysis

Fig. 4.3.11. SEM micrographs of heat-treated 6082.

Tab. 4.3.2. EDS result from heat-treated 6082. Each EDS spot corresponds to an area in Figure (4.3.11b).

Element	Weight percent [wt%]	Error [%]	Element	Weight percent [wt%]	Error [%]
EDS Spot 1			EDS Spot 4		
Al	95.24	1.35	Al	96.83	1.21
Si	2.85	9.54	Si	2.22	10.05
Mn	1.45	5.71	Mn	0.95	7.06
Cr	0.46	15.27	EDS Spot 5		
EDS Spot 2			Al	93.62	1.56
Al	98.41	1.06	Si	3.37	9.39
Si	1.59	10.74	Mn	1.68	6.39
EDS Spot 3			Fe	1.34	7.84
Al	99.23	1.17	EDS Spot 6		
Mn	0.77	7.39	Al	96.60	1.24
			Si	2.28	9.81
			Mn	1.13	7.29

The SEM micrograph used for EDS analysis of heat-treated Al-9Si-2Cu is given in Figure (4.3.11a). The particles used in the EDS analysis is marked in Figure (4.3.12b), and the results are summarized in Table (4.3.3). The particles have a more complex composition than the particles in 6082. These have more alloying elements, but Al, Fe, Mn, and Cu stand out as the main ones.

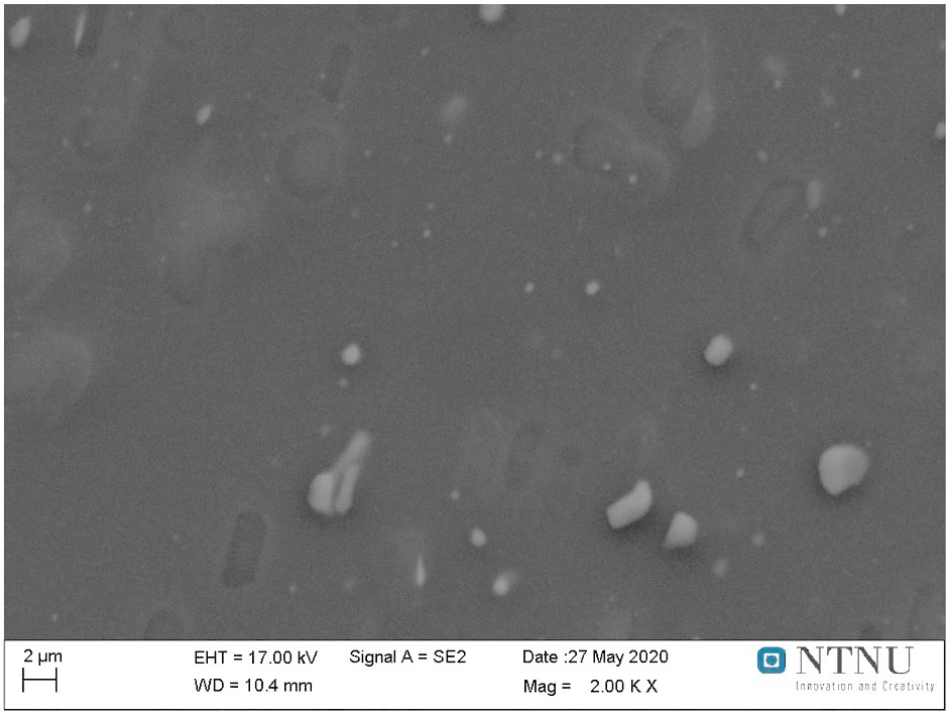

(a) SEM micrograph at 2000x magnification.

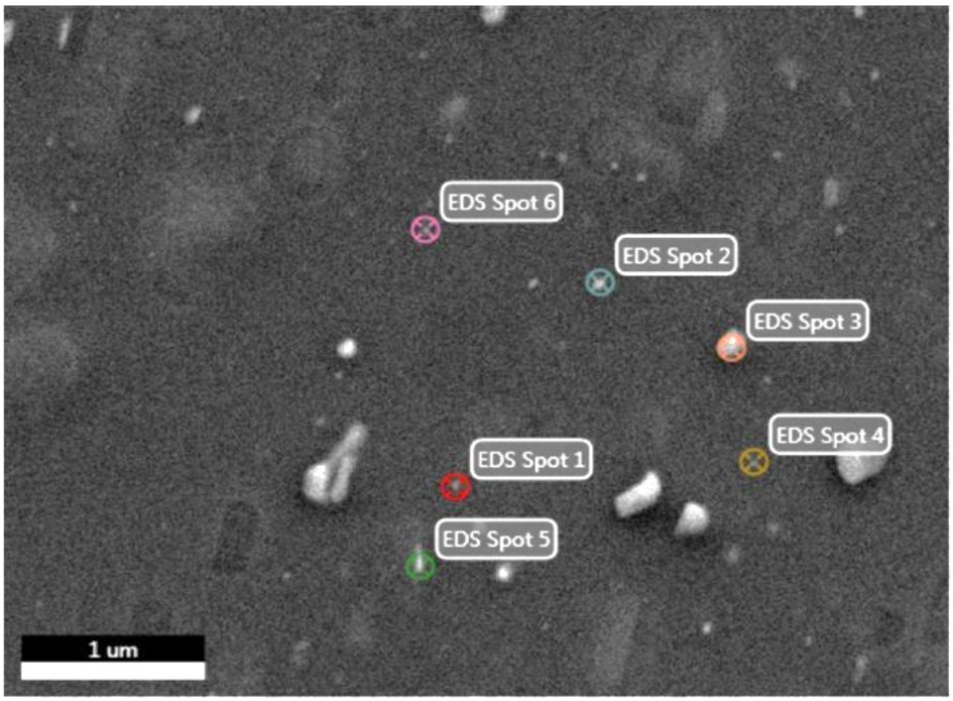

(b) Spots used for EDS analysis

Fig. 4.3.12. SEM micrographs of heat-treated Al-9Si-2Cu.

Tab. 4.3.3. EDS result from heat-treated Al-9Si-2Cu. Each EDS spot corresponds to an area in Figure (4.3.12b).

Element	Weight percent [wt%]	Error [%]	Element	Weight percent [wt%]	Error [%]
EDS Spot 1			EDS Spot 4		
Al	80.35	3.93	Al	85.11	3.41
Fe	6.26	3.04	Cu	5.94	4.09
Cu	5.06	4.59	Fe	4.34	3.31
Mn	2.41	4.48	Cr	2.18	4.46
Cr	2.38	4.34	Mn	2.02	4.80
V	1.29	6.09	Ca	0.41	6.33
Co	1.20	6.93	EDS Spot 5		
Mg	1.05	6.34	Al	70.16	4.96
EDS Spot 2			Fe	15.16	2.38
Al	75.41	4.44	Cu	7.40	4.03
Fe	10.26	2.54	Mn	3.78	3.45
Cu	5.23	4.34	Cr	3.51	3.63
Mn	3.60	3.54	EDS Spot 6		
Cr	3.37	3.53	Al	86.74	3.26
Co	1.12	6.89	Cu	6.38	3.68
Mg	1.00	6.99	Fe	2.70	3.64
EDS Spot 3			Cr	2.26	4.30
Al	67.23	5.22	Mn	1.92	4.18
Fe	14.59	2.26			
Cu	8.02	4.12			
Mn	3.64	3.07			
Cr	2.86	3.33			
Ni	2.18	4.51			
V	1.47	4.41			

Figure (4.3.13a) shows a SEM micrograph of heat-treated Al-9Si-0.3Mg. White particles of similar size can be observed on the surface. Some particles appear as "bumps" and are considerably larger. The particles used in the EDS analysis are marked in Figure (4.3.13b) and the results are summarized in Table (4.3.4). Al, Si, and Fe are the main elements in the particles.

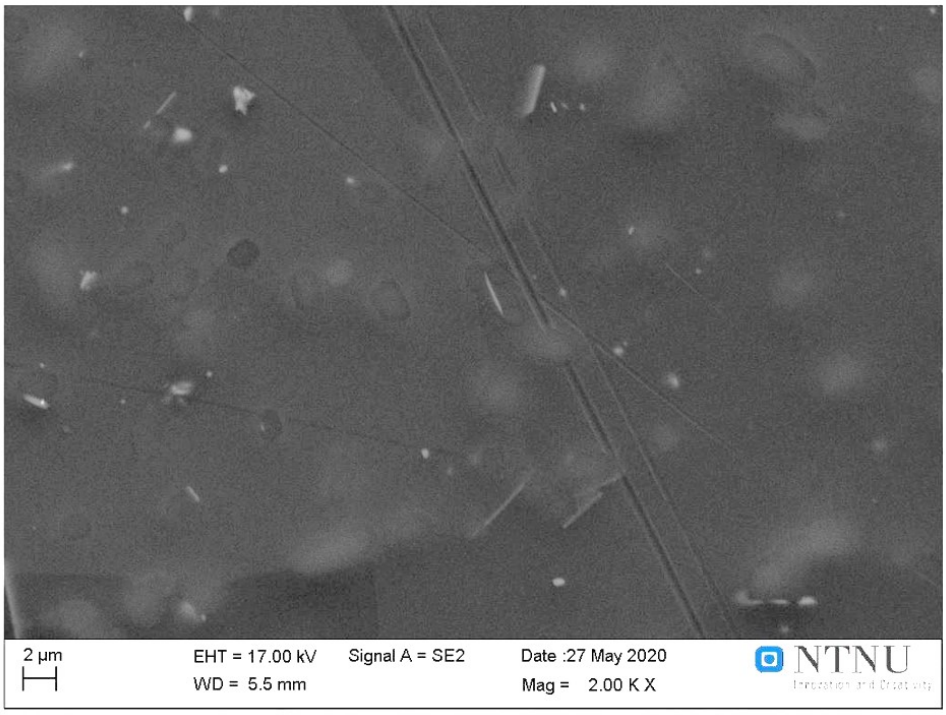

(a) SEM micrograph at 2000x magnification.

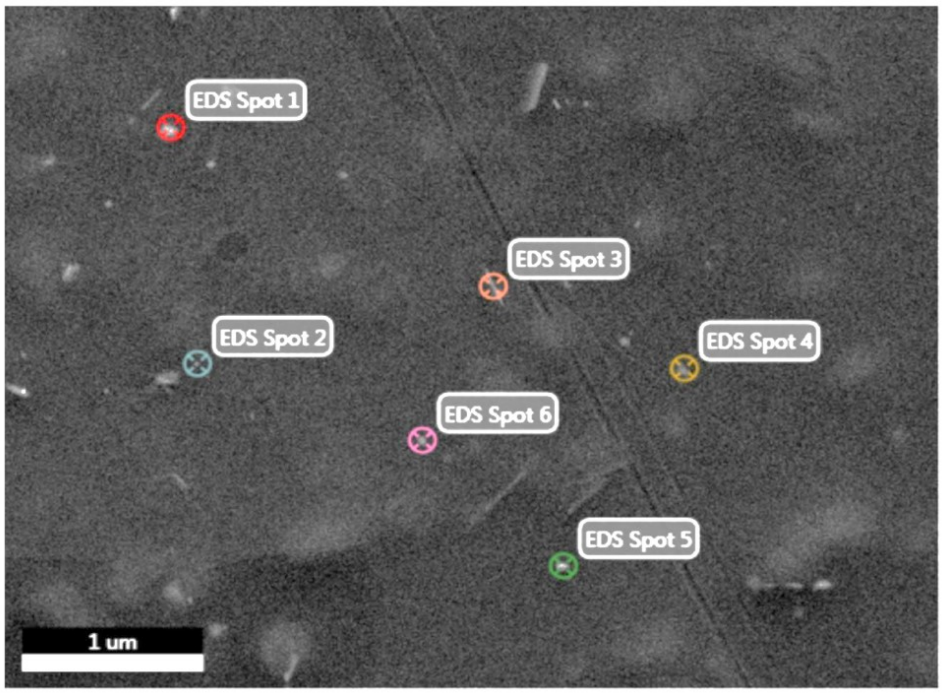

(b) Spots used for EDS analysis

Fig. 4.3.13. SEM micrographs of heat-treated Al-9Si-0.3Mg.

Tab. 4.3.4. EDS result from heat-treated Al-9Si-0.3Mg. Each EDS spot corresponds to an area in Figure (4.3.13b).

Element	Weight percent [wt%]	Error [%]	Element	Weight percent [wt%]	Error [%]
EDS Spot 1			EDS Spot 4		
Al	75.95	2.64	Al	89.46	2.19
Si	13.82	7.90	Fe	6.30	2.90
Fe	8.49	2.54	Si	3.36	9.32
EDS Spot 2			O	0.68	14.07
Al	90.51	1.54	Ni	0.19	40.22
Si	6.22	8.61	EDS Spot 5		
Fe	1.82	5.95	Al	85.01	2.50
EDS Spot 3			Fe	5.54	2.91
Si	50.88	5.90	Si	5.47	8.67
Al	44.08	2.11	Mg	1.72	4.19
Fe	3.46	3.75	O	1.44	11.13
			EDS Spot 6		
			Al	97.16	1.27
			Si	1.84	10.22
			Fe	0.69	14.53

4.4 Investigations of Aluminium Reinforcement

4.4.1 Bond-Strength Tests

The output of a bond-strength test is force [kN] versus slip. Equation (2.9.5) is usually used to transform force to bond stress. However, the equation is based on a bond length of 5 x diameter. In this case, the bond length was only 4 x diameter. Therefore, the equation is changed as described by equation (4.4.1).

$$\tau_{dm} = \frac{1}{4\pi} \frac{F_a}{d^2} \frac{f_{cm}}{f_c} \tag{4.4.1}$$

$\frac{f_{cm}}{f_c}$ was set to 1. The bond stress-slip curves for Ø10mm and Ø20mm are given in Figure (4.4.1) and Figure (4.4.2), respectively. Average bond-strength values ± standard deviation are given in Table (4.4.1). Note: Only heat-treated 6082, Al-9Si-2Cu, and Al-9Si-0.3Mg were bond strength tested.

The Ø10mm reinforcement and Ø20mm reinforcement generally display the same trend. 6082 and 5052 have considerably lower bond strength than Al-9Si-2Cu and Al-9Si-0.3Mg. However, the difference in bond strength is smaller among the Ø10mm profiles than the Ø20mm profiles. All aluminium samples have lower bond strength than the steel reinforcement. The curves of the aluminium reinforcement are also less steep, indicating that the reinforcement slips early and is slowly pulled out of the concrete.

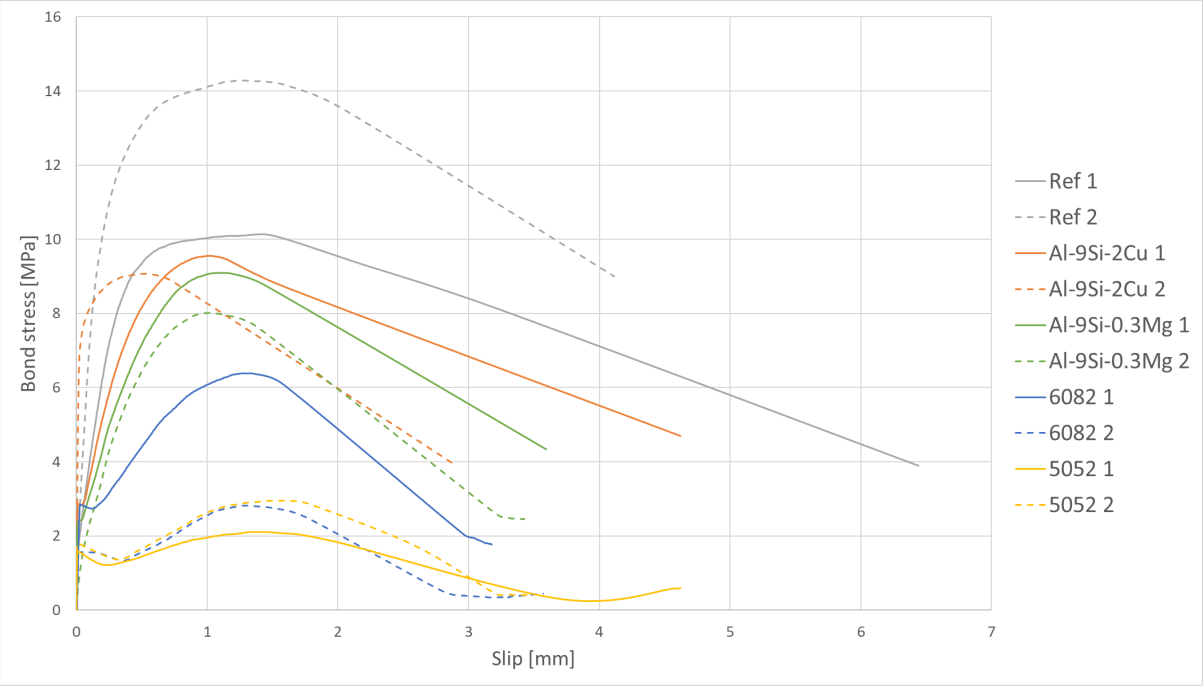

Fig. 4.4.1. Bond stress-slip curve of Ø10mm aluminium and steel reinforcement. Ref = reference steel.

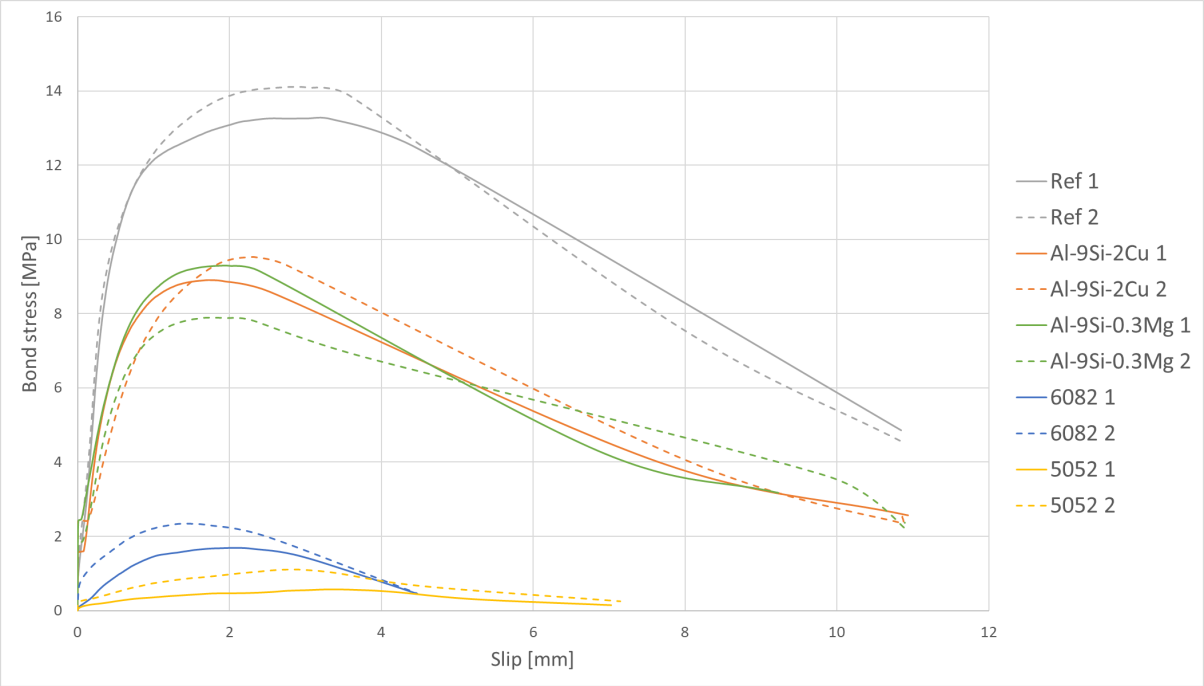

Fig. 4.4.2. Bond stress-slip curve of Ø20mm aluminium and steel reinforcement. Ref = reference steel.

Tab. 4.4.1. Average bond strength ± standard deviation.

Alloy	Bond strength, [MPa]	
	Ø10mm	Ø20mm
Steel	12.2 ± 2.9	13.7 ± 0.6
T6-6082	4.6 ± 2.5	2.0 ± 0.5
5052	2.5 ± 0.6	0.8 ± 0.4
T6-Al-9Si-2Cu	9.3 ± 0.3	9.2 ± 0.4
T6-Al-9Si-0.3Mg	8.6 ± 0.8	8.6 ± 1.0

4.4.2 Hydrogen Measurements

The results of the hydrogen measurements are given in Figure (4.4.3) and Figure (4.4.4). Hydrogen gas is defined as % hydrogen gas in the exicator at the given time. Figure (4.4.3) compares the hydrogen evolution of ribbed and non-ribbed samples. Independent of ribs or no ribs, the curves are steepest in the first 5 to 10 hours, at which most of the hydrogen is released. After this, the curves flatten out and seem to approach a steady state. The ribbed samples release more hydrogen than the non-ribbed samples. 6082 release the most hydrogen and Al-9Si-2Cu the least.

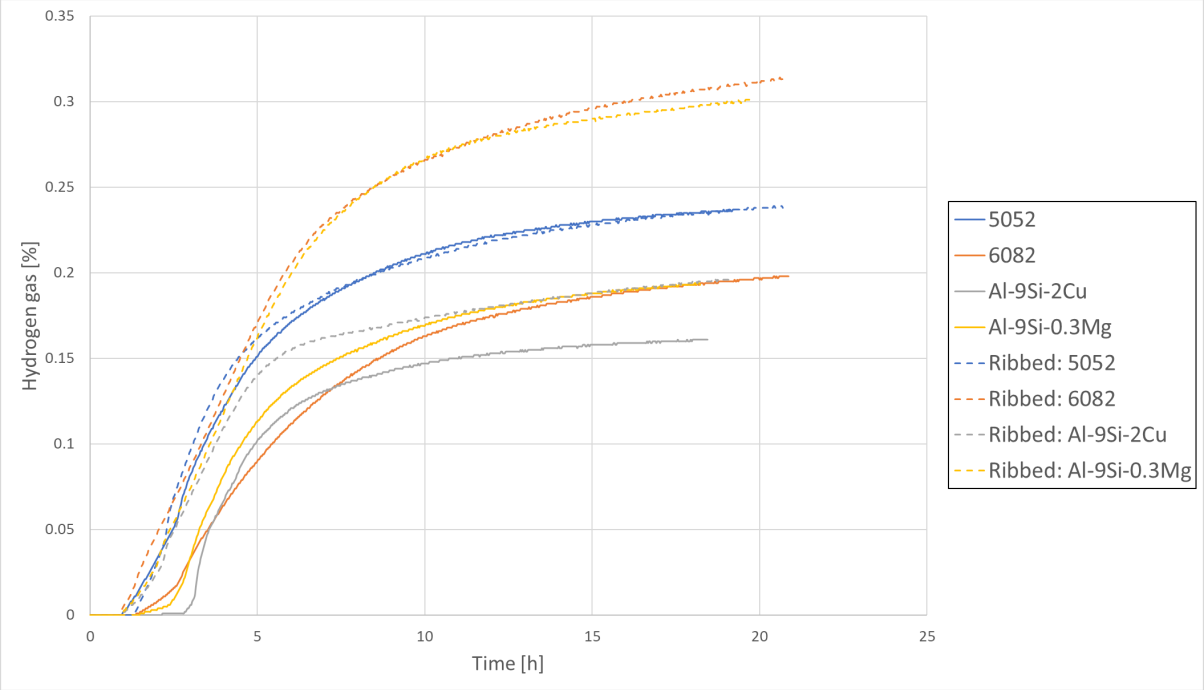

Fig. 4.4.3. Hydrogen evolution of ribbed and non-ribbed aluminium samples cast in concrete.

Figure (4.4.4) compares the heat-treated (T6) samples to the not heat-treated samples, both without ribs. The heat-treated samples evolve significantly less hydrogen than the not heat-treated samples. The curve is also less steep than for the heat-treated samples. T6 Al-9Si-0.3Mg releases the least hydrogen and 5052 the most.

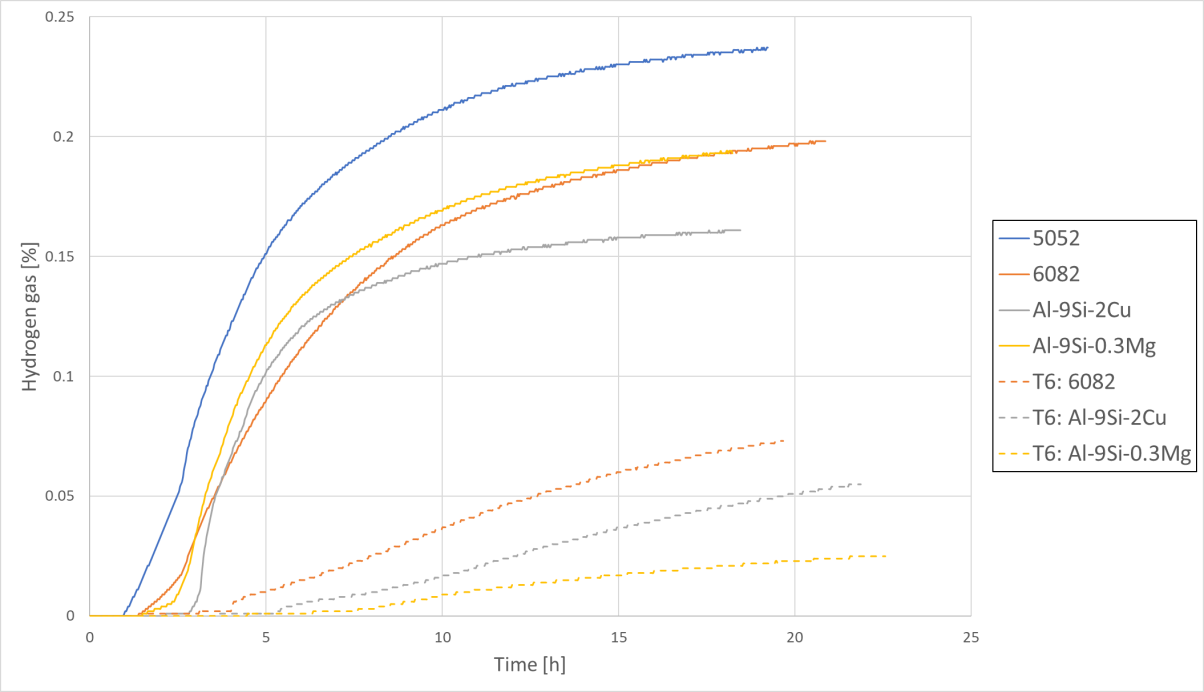

Fig. 4.4.4. Hydrogen evolution of heat-treated and not heat-treated samples aluminium samples cast in concrete.

4.4.3 Visual Inspection

The bond-strength tested samples after pull out can be observed in Figure (4.4.5) and Figure (4.4.6). Steel, T6-Al-9Si-2Cu, and T6-Al-9Si-0.3Mg have concrete residue in between the ribs, while 5052 and T6-6082 have a layer of concrete that encloses the profiles. There is little difference between the Ø10mm reinforcement and Ø20mm reinforcement, but there appears to be less concrete residue on the Ø10mm T6-6082 samples compared to the Ø20mm T6-6082 samples.

(a) Reference steel

(b) T6-6082

(c) 5052

(d) T6-Al-9Si-2Cu

Fig. 4.4.5. Ø10mm aluminium reinforcement after bond strength test.

(e) T6-Al-9Si-0.3Mg

Fig. 4.4.5. Ø10mm aluminium reinforcement after bond strength test.

(a) Reference steel

(b) T6-6082

(c) 5052

(d) T6-Al-9Si-2Cu

Fig. 4.4.6. Ø20mm aluminium reinforcement after bond strength test.

(e) T6-Al-9Si-0.3Mg

Fig. 4.4.6. Ø20mm aluminium reinforcement after bond strength test.

To check for signs of reaction/corrosion between the concrete and aluminium reinforcement, the samples used in bond-strength tests were split in half and inspected (except for T6-Al-9Si-0.3Mg). The samples were split approximately 28-30 days after they were cast. In Figure (4.4.7), the split aluminium reinforced concrete can be seen. The area where concrete and aluminium were in contact is marked. There was no obvious corrosion product on the interface between the aluminium alloys and concrete. However, there was a dark reaction product between 6082-T6 and the concrete. This can be observed in Figure (4.4.8). The concrete that encircled 5052 and T6-6082 had more pores than the T6-Al-9Si-2Cu- concrete sample.

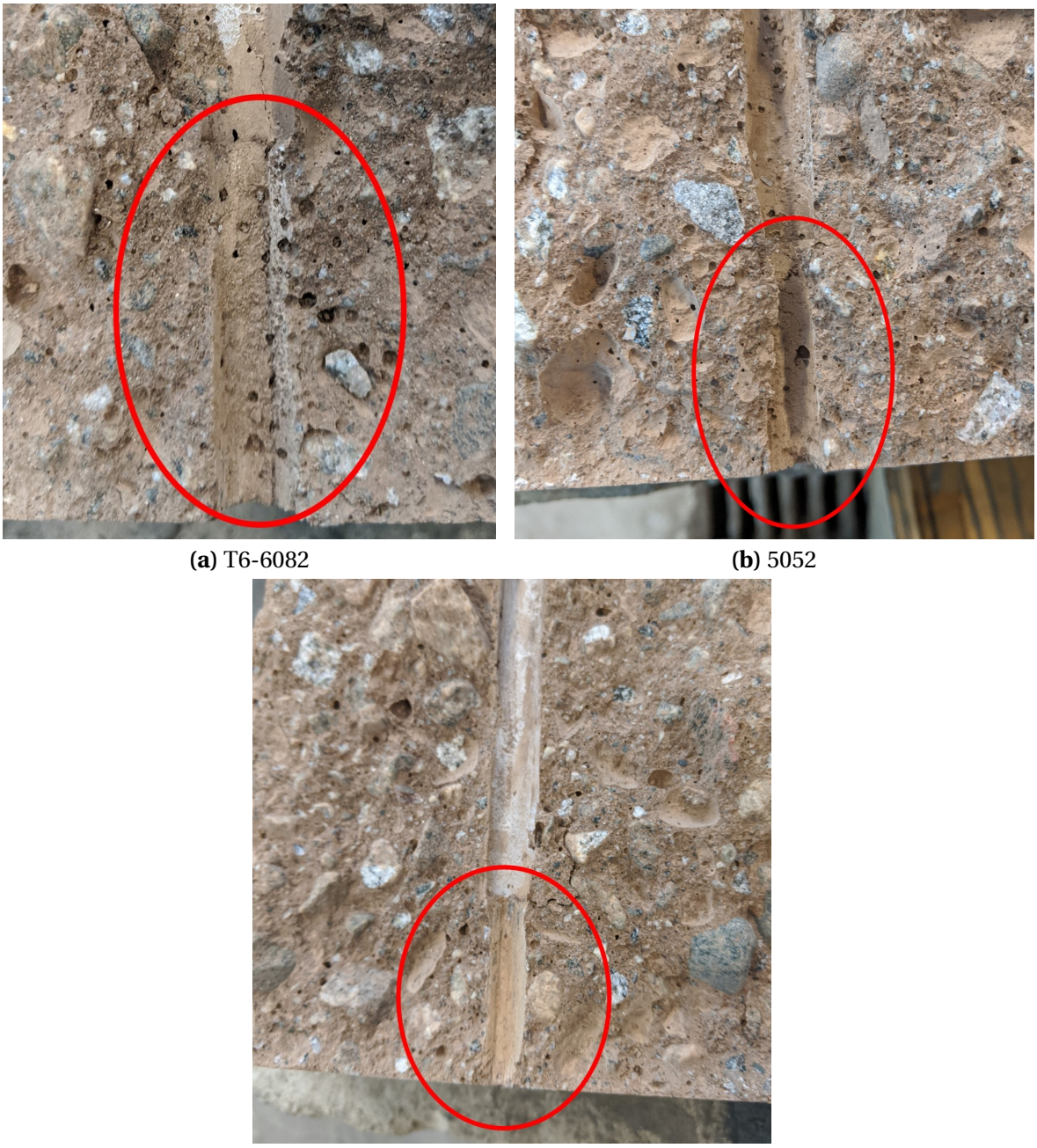

(a) T6-6082 **(b)** 5052

(c) T6-Al-9Si-2Cu

Fig. 4.4.7. Split aluminium reinforced concrete samples.

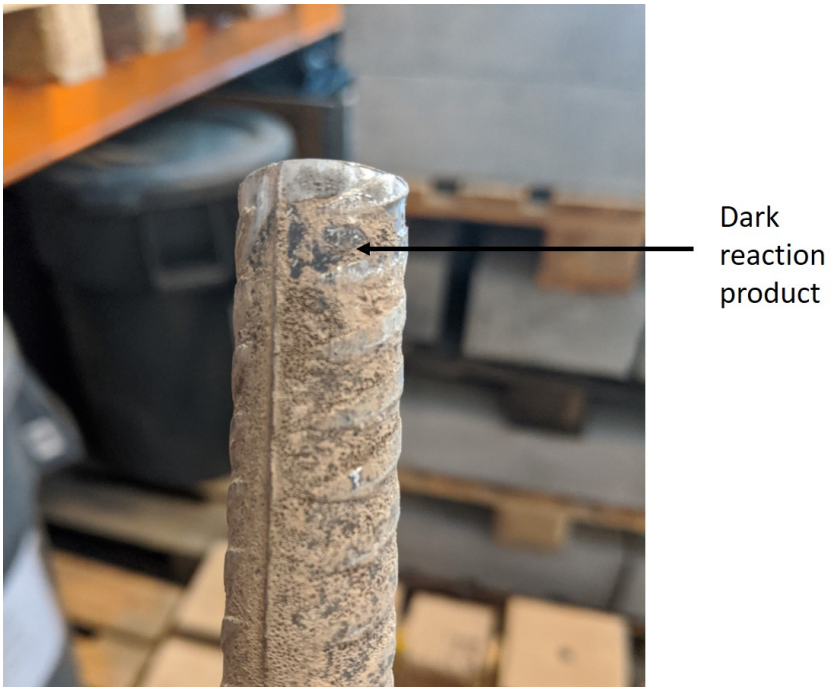

Fig. 4.4.8. T6-6082 reinforcement bar after bond strength test. A dark reaction product can be seen under the concrete residue.

5 Discussion

5.1 Microstructural Observations Through LOM and SEM Examinations

This thesis aims to investigate the possibility of aluminium reinforcement and recycled automotive aluminium in concrete. The reinforcement was extruded and heat treated as well as rolled and cast in concrete, and the effect of the two first processes are briefly discussed in this section.

As was mentioned in Section 2.6.1, the deformation and heat will be largest at the edges of the extruded product. The cooling rate will also be highest at the edges. In general, this divides the structure into three sections: (1) Edge: The grains have recrystallized and been quickly cooled. Fine and small grains can be found here. (2) Intermediate: Recrystallization has initiated, but the cooling rate is slower than at the edges. The grains are larger here than at the edges. (3) Center: The largest grains are found here. The center will have the slowest cooling rate and the least deformation and recrystallization. The different sections are illustrated in Figure (5.1.1).

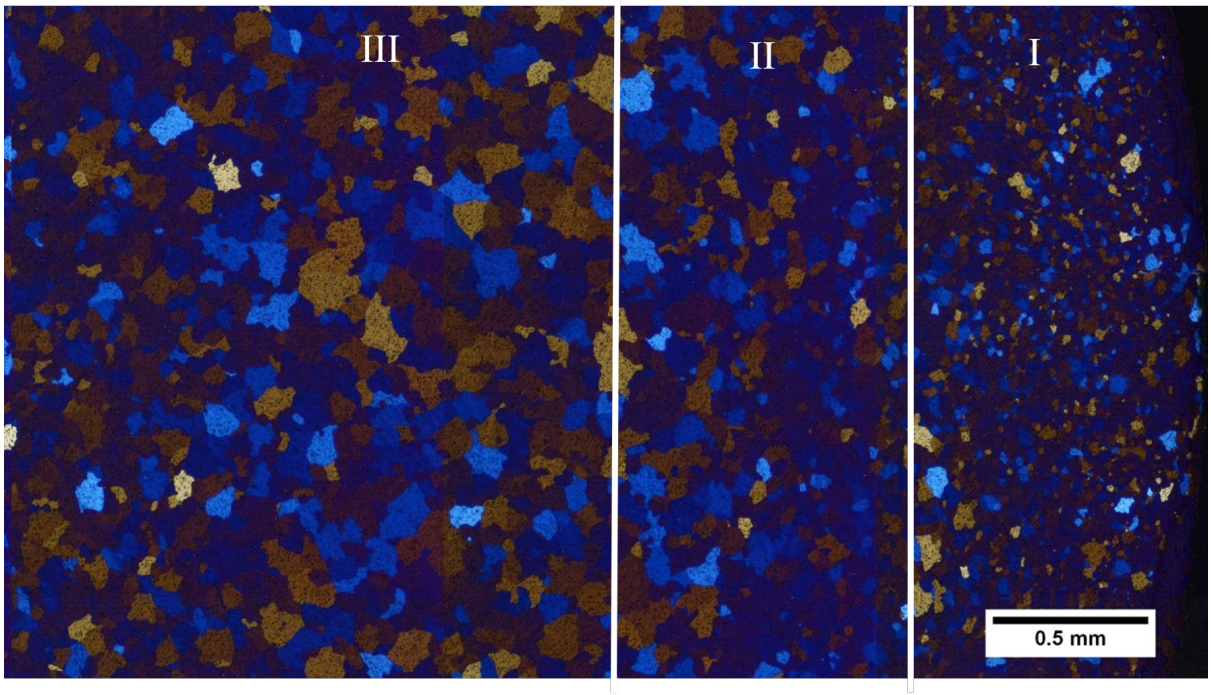

Fig. 5.1.1. Sections of grain structure after extrusion.

The hardness of the Ø20mm profiles was higher than the Ø10mm profiles. This was most likely caused by a difference in extrusion ratio (highest for Ø10mm), cooling rate (lowest for Ø10mm), and ram speed. All of these will lead to more recrystallization and consequent grain growth. Excessive grain growth will lower the strength of a material, as shown by equation (2.5.1). There is little difference in UTS and elongation between as-extruded Ø10mm and

Ø20mm profiles.

The different grain structure seen in 6082 (both as-extruded and T6) is because the grains have aligned in the same direction. In some alloys, recrystallization leads to a equiaxed grain structure, while for others, the direction of the recrystallized grains reflect the type of working (here: extrusion) [57]. This can be seen in Figure (4.1.5), Figure (4.1.9), and Figure (4.3.8). In the as-extruded 6082, recrystallization has occurred on the edges of Ø10mm but not Ø20mm. This was caused by the reasons that were discussed in the previous paragraph.

In Table (4.1.1) and Table (4.3.1) the measured tensile properties of the as-extruded and heat-treated samples are given. The two tables show that the strength increased after heat treatment, as was expected. However, the total extension at maximum force was almost halved. The EDS results for Al-9Si-2Cu and Al-9Si-0.3Mg, given in Table (4.3.3) and Table (4.3.4), reveal that the precipitates contain iron. In Section 2.5.3, the precipitation in Al-Si alloys was introduced along with the fact that β-Al_5FeSi and π-AlFeMgSi often precipitates. Both of these will cause an increase in strength and brittleness. This most likely caused the trend seen after heat treatment. The EDS result of T6-6082 is given in Table (4.3.2). The table gives little insight into what caused the decrease in ductility. As this was not the main focus of the thesis, it was not further investigated.

The grain structure of the heat-treated aluminium samples was similar to the as-extruded profiles; the edges had the smallest grain size and the center the largest (except for T6-6082). The difference in grain structure was caused by the difference in cooling rate from edge to center. Compared to the as-extruded structure, the grains are more homogeneous.

In Section 4.3.2, it was briefly mentioned that Ø20mm T6-6082 had significantly lower strength than Ø10mm T6-6082. What caused this difference has not been determined. However, it is possible that residual stress was introduced during quenching. Cold deformation, such as rolling, will relieve some of this stress [57]. Because of this, the tensile strength of the Ø20mm T6-6082 tensile specimens is not necessarily representative of the T6-6082 Ø20mm profiles that were rolled and cast in concrete.

5.2 Development of Rolling Method for Aluminium Reinforcement

Rolling introduces strain and strain hardening, as described in Section 2.7.1. The amount of strain will determine the strength contribution. The hardness before and after rolling is given in Figure (4.2.3) and Figure (4.2.4) for Ø10mm and Ø20mm, respectively. The hardness of the Ø10mm profiles have increased more than the Ø20mm profiles. This indicates that the strain was greater in the Ø10mm roller track than the Ø20mm track.

The theoretical rib values after rolling are given in Table (3.5.1), and the measured values are given in Table (4.2.1). Compared to theoretical values, the rolling of Ø20mm was more successful than the rolling of Ø10mm. The roller tracks were originally designed for Ø10.4mm and Ø20mm. The Ø10mm profiles were extruded with a diameter of 10.5mm, i.e. 0.1mm larger. This has probably not had a large impact on the result, but it might have forced more of the metal to the sides instead of up in the tracks. It would also increase the strain and explain why Ø10mm showed a larger increase in hardness after rolling.

Images from simulations conducted by SINTEF of the roller process are given in Appendix D. Figure (D.0.1) and Figure (D.0.4) show the simulated strain on the outside of the Ø10mm profile and Ø20mm profile, respectively. Most of the strain is concentrated on the edge of the profile and not on the ribs. The most difficult part of designing the roller tracks was achieving enough pressure to press the metal into the roller tracks. This is illustrated in Figure (D.0.2) and (D.0.5). Here, it is clear that the metal does not fill the roller tracks.

Because the metal does not completely fill the roller tracks, the shape of the ribs are not correct. According to NS-EN 10080:2005, the ribs shall have a crescent shape [54]. After rolling, the ribs were flat and not crescent. This could be harmful to the mechanical adhesion between the aluminium and concrete. Usually, the geometry of steel reinforcement is produced through several rolling steps [53]. Each step further reducing the thickness. For aluminium reinforcement to achieve the same geometry, more rolling steps needs to be applied. With only one set of rolls this is hard to achieve. There is a severe synchronization issue with adding more tracks to the same set of roles. Having several sets of rolls is therefore the easiest solution to the problem.

The result of the bond strength tests, given in Table (4.4.1), indicates that mechanical adhesion has not played a significant role. If it did, the results of the different alloys would be more similar. Therefore, the ribs need to be improved. It might be necessary to have even larger rib height for aluminium reinforcement than steel reinforcement. Still, it bodes well for aluminium reinforcement that the Al-Si-alloys are so close to steel in bond strength with such shallow ribs.

Another way to improve the geometry of the ribs is to use a different rolling set-up. Because the roller method used was two-high rolling (illustrated in Figure (2.7.2)), the rollers will be pushed apart as the pressure between them increases. Using a different roller method where more force is applied to the rollers, for example four-high rolling, could improve the outcome. However, the maximum rib height that is possible to achieve with the current roller tracks barely fulfills the minimum requirement described in Table (2.8.1).

5.3 The Durability and Performance of Aluminum Reinforcement

Hydrogen gas evolution and bond strength of aluminium in concrete were measured to evaluate the performance of aluminium reinforcement. The result of these were presented in Section 4.4.

In Figure (4.4.4) the hydrogen evolution of heat-treated and not heat-treated samples is given. The samples that were heat treated resulted in less hydrogen gas evolution than the not heat-treated samples. When the samples were heat-treated, it is likely that the thickness of the oxide surface layer increased. A study by L.P.H Jeurgens et al. (2002) concluded that the growth kinetics of Al oxide layer could be separated into two stages [61]. The first is fast and limited by a rate-limiting energy, and occurs at temperatures below 300°C. The limited thickness increases with increasing temperature. The second stages is at high temperatures (T≥ 400 °C), and is slow but only limited by diffusion. Heat treatment will thus increase the thickness of the oxide layer. The thickness will also increase with increasing time at high temperature. Because the Al-Si-alloys had a significant higher SSHT time, there will be a difference in thickness between T6-6082 and T6-Al-9Si-2Cu/T6-Al-9Si-0.3Mg.

The reaction between Al_2O_3 and hydroxides in cement does not release hydrogen gas, as shown in equation (2.3.1). A thick Al_2O_3-layer will for that reason result in less hydrogen gas evolution. The thickness of the layer before and after heat treatment is difficult to measure due to its nm-scale. The thickness was not measured here. Previous studies have successfully measured the Al_2O_3-layer thickness by X-ray photoelectron spectroscopy (XPS) [61, 62].

The hydrogen evolution of samples with and without ribs is given in Figure (4.4.3). The difference between the samples is not large, but ribs generally lead to more hydrogen evolution. The surface area of the sample will slightly increase when ribs are rolled into the profile, which is probably the reason for the increase in hydrogen evolution. All hydrogen measurements indicate that the aluminium initially reacts with the cement, producing hydrogen gas, with a decreasing production rate over time

The results of the bond strength tests given in Table (4.4.1) show that 5052 and T6-6082 had significantly lower bond strength than T6-Al-9Si-2Cu and T6-Al-9Si-0.3Mg. The surface of the aluminium reinforcement after testing had some concrete residue, which can be seen in Figure (4.4.5) and Figure (4.4.6). 5052 and T6-6082 had a layer of concrete residue on the surface, while T6-Al-9Si-2Cu and T6-Al-9Si-0.3Mg had small areas with concrete residue inbetween the ribs. A side by side image of T6-6082 and T6-Al-9Si-0.3Mg after the tests is given in Figure (5.3.1). This indicates that the concrete, and not the bond between Al and concrete, failed during testing.

Fig. 5.3.1. Aluminium reinforcement after bond strength test. 6082 is covered in more concrete residue than Al-9Si-0.3Mg.

The visual inspection of the split concrete samples showed more pores in the concrete of T6-6082/5052 than T6-Al-9Si-2Cu (Figure (4.4.7a) - Figure (4.4.7c)). Such pores will decrease the strength of both the concrete, and the bond between the reinforcement and the concrete. The pores could have been the result of one of two things: (1) air bubbles mixed into the concrete during casting, or (2) hydrogen evolution. Because the low bond strength is directly related to the alloys with the highest hydrogen gas evolution, the latter is the more likely option.

Not only hydrogen evolution, but the nature of the hydrogen evolution could affect the outcome of bond-strength testing. Al-9Si-2Cu is prone to localized microgalvanic corrosion [29]. Wet cement could work as an electrolyte during galvanic corrosion between the Al-matrix and Fe-/Cu-rich precipitates. This reaction will release hydrogen gas, but in smaller amounts in certain areas. Consequently, small pores will be incorporated into the concrete. On the other hand, 6082 and 5052 have low alloying content and there are few precipitates on the surface. Instead of corroding in small areas, corrosion is uniform. Therefore, hydrogen gas will evolve all over the profile and larger pores will be visible in the hardened concrete. In Figure (4.4.5) and Figure (4.4.6), the profiles after bond strength testing are found. Looking closely at the T6-6082 and 5052 samples, pores can be observed in the residue concrete. This is highlighted in Figure (5.3.2). The same structure could not be found on the other two alloys.

However, this is just a hypothesis and no experimental work has been conducted to support it. Electrochemical investigations of the different aluminium alloys in concrete could provide more answers.

(a) 5052 **(b)** 6082

Fig. 5.3.2. Highlighted area showing pores on Ø20mm aluminium reinforcement after bond strength testing. Adapted from Figure (4.4.6).

Pores in the concrete, caused by hydrogen gas evolution, is a possible reason for the low bond strength of T6-6082 and 5052, but it is not the only reason. T6-6082 led to more hydrogen evolution, but the difference between the T6-Al-Si-alloys and T6-6082 is small. Therefore, based on the hydrogen measurements, the bond strength between these three alloys should

not be that different. A dark reaction product was also discovered on the surface of T6-6082. If this product expands upon formation, it will lead to cracking and harm the bond strength. This is the same effect that is seen when steel reinforcement corrodes. The reaction product between T6-6082 and concrete could be characterized through X-ray diffraction, TEM, and/or SEM.

Another possible reason for the difference in bond strength could be the coefficient of linear thermal expansion (CTE). The CTE of 6082 and 5052 is considerable higher than Al-Si-alloys, which can be interpreted from Figure (2.9.2). If the temperature of the aluminium reinforced concrete increases (i.e. during curing), then T6-6082 and 5052 will expand more than Al-Si. Expansion will lead to microcracking in the concrete surrounding the reinforcement. However, it is unlikely that this had a significant impact on the results observed in this thesis, as the temperature of the concrete only changed 2-4 °C during curing (according to SINTEF who was responsible for the concrete casting).

The ultimate tensile strength of the heat-treated profiles and 5052 is significantly lower than the requirements given in Table (2.8.2). The standard requires σ_{UTS} = 600 MPa, while the aluminium profile with the highest UTS value was Ø20mm T6-Al-9Si-2Cu with σ_{UTS} = 393 MPa. However, this does not mean that aluminium can not be used as reinforcement. Steel and aluminium are two different metals with widely different properties. For example, the density of aluminium is approximately one third of the density of steel (2.7 g/cm^3 vs 7.7 g/cm^3 [35]). This entails that an aluminium reinforced concrete structure will be much lighter than a steel reinforced structure. Because of this, the strength of aluminium rebars does not need to be as high as steel reinforcement. In addition, due to the increase in corrosion resistance, the cover thickness of the reinforcement does not need to be as high, which decreases the mass even further. Therefore, it is necessary to develop a new standard concerning aluminium reinforcement and the uses of it.

Even though CTE probably had little impact on the samples in this thesis, it may cause problems for the future application of aluminium reinforced concrete. Under normal operating conditions, large variations in temperature is not expected. However, during the event of a fire, the temperature will rise. The Al reinforcement will expand at a higher rate than concrete and cause significant cracking in the structure. If the integrity of the structure is weakened too quickly, there won't be enough time to evacuate the building. This poses a potentially large safety risk. Therefore, Al-alloys with CTE as close as possible to concrete should be used. Alternatively, aluminium reinforcement could be used in areas with low risk of fire (e.g. docks).

In Section 2.3, it was mentioned that aluminium alloys containing copper suffer from localized corrosion when exposed to seawater. One of the main intentions behind using aluminium as reinforcement, is to apply it in areas where steel reinforcement performs poorly. This is mostly in areas with high concentration of chloride ions (e.g. near seawater). Therefore, it is unfortunate that the alloy that performs best in bond-strength tests and hydrogen measurements is difficult to apply in such conditions. However, it is possible to design structures with more than one alloy. For example, a corrosion resistant alloy (6082 or 5052) is

placed nearest to the water (the edges) and Al-9Si-2Cu is placed in the center of the structure where there is little risk of seawater ingress.

5.4 Prospect of Recycled Automotive Aluminium as Reinforcement in Concrete

Aluminium production is responsible for significantly more GHG-emissions than steel due to the energy-consuming electrolysis process (see Figure (2.1.4)). For aluminium reinforcement to be more sustainable than steel reinforcement, recycled aluminium should be used. Recycled automotive aluminium has been proposed here as reinforcing material. Although no material was recycled in this thesis, some conclusions can be drawn from the results of the two Al-Si-alloys.

The Al-9Si-2Cu-alloy has the composition of a typical engine block and Al-9Si-0.3Mg is similar to a wheel/rim alloy. Compared to the other Al-alloys, the Al-Si-alloys have better bond strength in concrete and the least hydrogen evolution. T6-Al-9Si-2Cu have the highest strength. The ductility of these alloys are not as great as the other Al-alloys, but they are still within the requirements given in Table (2.8.3).

Based on the results obtained in this thesis, the use of recycled automotive aluminium as reinforcement is promising. Especially if the ribs are improved. One challenge is that engine block aluminium is secondary aluminium and contains a lot of impurities. Thus, the properties of each individual engine block will be harder to predict. In addition, the composition varies between different car brands and car models.

Aluminium is not as heat and wear resistant as steel, and because of this, certain parts of aluminium engine blocks has to be coated. For example, the piston cylinders are often coated with iron or electrodeposited coatings [63]. These have to be removed before recycling or accepted as a significant impurity. The effect of the impurities can be mitigated by diluting with an aluminium alloy with less impurities.

6 Conclusion

This master's thesis investigated the possibilities of using aluminium as reinforcement in concrete and the prospect of recycled automotive aluminium as reinforcement. The key findings are as follows:

- The rolling method for aluminum rebars has to be further developed. The method used in this thesis did not provide satisfactory results. Further developments could be using multiple roller steps and/or a different rolling setup (e.g. four-high rolling).
- T6-Al-9Si-2Cu and T6-Al-9Si-0.3Mg performs better in concrete than T6-6082 and 5052, based on bond strength testing and hydrogen evolution measurements.
- The average bond strength of standard steel reinforcement was measured as 12.2 and 13.7 MPa (Ø10mm and Ø20mm). For T6-Al-9Si-2Cu it was measured to be 9.3 and 9.2 MPa (Ø10mm and Ø20mm). This was a promising result, considering the quality of the ribs was much poorer for the aluminium reinforcement.
- No experimental work was conducted to investigate the reasons behind the difference in bond strength between the alloys, but three hypotheses were presented: (1) the increase in hydrogen gas evolution for T6-6082 and 5052 damaged the bond strength due to formation of pores in the hardened concrete, (2) the formation of an expansive reaction product between T6-6082 and concrete resulted in microcracking, and (3) the coefficient of linear thermal expansion of T6-6082 and 5052 is higher than for Al-Si-alloys which means that T6-6082 and 5052 will cause more cracking as it expands during the curing process.
- The results acquired from the bond strength tests and hydrogen measurements of Al-9Si-2Cu and Al-9Si-0.3Mg, provide answers on whether automotive aluminum could be used as reinforcement. According to the results found in this thesis, it is possible but further testing is needed.

7 Further Work

To further explore the possibilities of aluminium reinforcement, the author suggest the following work:

- Testing of aluminium alloys in concrete in different electrolytes (e.g. NaCl), with short time and long time exposure.
- XRD, SEM, and/or TEM of reaction product between 6082 and concrete.
- Research into the coefficient of linear thermal expansion of different aluminium alloys compared to the DARE2C concrete mix.
- Bond strength testing and hydrogen evolution measuring of recycled automotive aluminium in concrete.

References

[1] The Architect's Newspaper. *Concrete production produces eight percent of the world's carbon dioxide emissions*. Available on: https://archpaper.com/2019/01/concrete-production-eight-percent-co2-emissions/. Retrieved 13-06-2020.

[2] Statistisk sentralbyrå [Statistics Norway]. Bilparken [car population]. https://www.ssb.no/bilreg. Retrieved 19-05-2020.

[3] M. M Fagermo. *Screw Extrusion of Aluminium for Use in Sustainable Concrete Structures*. NTNU, Trondheim, 2019. unpublished.

[4] J.R. Davis. *ASM Speciality Handbook: Aluminium and Aluminium alloys*. ASM International, 1993.

[5] J.K. Solberg. *Teknologiske metaller og legeringer (Norwegian) [Technological metals and alloys]*. Tapir Forlag, 2014.

[6] F. King. Aluminium and its alloys, 1987.

[7] E.L Huskins, B Cao, and K.T Ramesh. Strengthening mechanisms in an Al–Mg alloy. *Materials Science Engineering A*, 527(6):1292–1298, 2010.

[8] R Jones, J Vetrano, and C Windisch. Stress corrosion cracking of Al-Mg and Mg-Al alloys. *Corrosion*, 60(12):1144–1154, 2004.

[9] Al (Aluminum) Binary Alloy Phase Diagrams. In *Alloy Phase Diagrams*. ASM International, 2016.

[10] K. G. Skorpen. *Screw extrusion of light metals : development of materials, characterization and process analysis*, volume 2018:218 of *Doctoral Theses at NTNU*. 2018.

[11] United Nations. Climate change. Available on: https://www.un.org/en/sections/issues-depth/climate-change/. Retrieved 17-04-2020.

[12] American Chemical Society. Production of aluminum: The hall-héroult process. Available on: https://www.acs.org/content/acs/en/education/whatischemistry/landmarks/aluminumprocess.html. Retrieved 30-04-2020.

[13] J. M Allwood. Sustainable materials : with both eyes open, 2012.

[14] International Aluminium institute (IAI). Life cycle inventory data and environmental metrics for the primary aluminium industry. 2017. Available on:http://www.world-aluminium.org/publications/tagged/life%20cycle/. Retrieved 05-06-2020.

[15] The Global Aluminium Recycling Committee (GARC). Global aluminium recycling: A cornerstone of sustainable development, 2009. Available on: http://www.world-aluminium.org/media/filer_public/2013/01/15/fl0000181.pdf. Retrieved 30-04-2020.

[16] M. E Schlesinger. *Aluminum recycling*. CRC Press, 2007.

[17] J. R Duflou, A. E. Tekkaya, M. Haase, T. Welo, K. Vanmeensel, K. Kellens, W. Dewulf, and D. Paraskevas. Environmental assessment of solid state recycling routes for aluminium alloys: Can solid state processes significantly reduce the environmental impact of aluminium recycling? *CIRP Annals - Manufacturing Technology*, 64(1):37–40, 2015.

[18] P. K. Mehta and P. J. M Monteiro. *Concrete : microstructure, properties, and materials*. McGraw-Hill, 3rd edition, 2006.

[19] P.K. Mehta. Natural pozzolans: Supplementary cementing materials in concrete. *CANMET Special Publications*, 86:1–33, 1987.

[20] Portland Cement Association. How cement is made. Available on: `https://www.cement.org/cement-concrete-applications/how-cement-is-made`. Retrieved 02-04-2020.

[21] A. Al-Tabbaa. *The concrete that heals its own cracks* (2016). Published in World Economic Forum. Available on: `https://www.weforum.org/agenda/2016/01/the-concrete-that-heals-its-own-cracks/`. Retrieved 16-04-2020.

[22] P.J.M Monteiro. Chemical attacks on concrete, 2019. University lecture in *CIVENG 241 Concrete Technology* at UC Berkeley.

[23] H Chen, J.A Soles, and V.M Malhotra. Investigations of supplementary cementing materials for reducing alkali-aggregate reactions. *Cement and Concrete Composites*, 15(1):75–84, 1993.

[24] H. Justnes. How SCMs improve concrete durability–a fundamental view. In *4th Int. Conf. Sustain. Constr. Mater. Technol., Proceedings, Las Vegas*, 2016.

[25] Ø. Vennesland. An introduction to corrosion in concrete, 2019. University lecture in *TMT4255 - Corrosion and Corrosion Protection* at NTNU.

[26] L. Rodgers. Climate change: The massive co2 emitter you may not know about. `https://www.bbc.com/news/science-environment-46455844`. Retrieved 04-11-2019.

[27] Food and Agriculture Organization of the United Nations. *Water scarcity is one of the greatest challenges of our time*. Available on: `https://www.weforum.org/agenda/2019/03/water-scarcity-one-of-the-greatest-challenges-of-our-time/`. Retrieved 14-03-2020.

[28] U. Nürnberger. Corrosion of metals in contact with mineral building materials. *Otto-Graf-Journal*, 12:69, 2001.

[29] Kemal Nişancıoğlu. Corrosion basics and engineering : lecture notes for the course 53523 korrosjonslære, 1994.

[30] H. Justnes. Concrete reinforced with aluminium metal - principles and implications. 2018. Unpublished.

[31] V. G. Bliksvær, J. S. Bjørklund, and H. Reiersen. *Aluminiumslegeringer som armering i betong - et eksperimentelt studie. (Norwegian) [Aluminium alloys as reinforcement in concrete - an experimental study]*. 2019.

[32] H. S. Amundsen. *The Applicability of Aluminium Alloys as Reinforcement Material in Concrete Constructions*. NTNU, Trondheim, 2018.

[33] E. M. Kolberg, Å. T. Eide, and E. Østbye. *The possibility of using reinforcement bars of aluminium in concrete structures*. NTNU, 2018.

[34] A. Rollett, F.J Humphreys, G.S Rohrer, and M. Hatherly. *Recrystallization and Related Annealing Phenomena*. Elsevier Science, 2 edition, 2004.

[35] W. D Callister. *Materials science and engineering*. Wiley, 9th ed., si version. edition, 2015.

[36] G.A. Edwards, K. Stiller, G.L. Dunlop, and M.J. Couper. The precipitation sequence in Al–Mg–Si alloys. *Acta Materialia*, 46(11):3893 – 3904, 1998.

[37] S.J. Andersen, H.W. Zandbergen, J. Jansen, C. TrÆholt, U. Tundal, and O. Reiso. The crystal structure of the β'' phase in Al–Mg–Si alloys. *Acta Materialia*, 46(9):3283 – 3298, 1998.

[38] H. W. Zandbergen, S. J. Andersen, and J. Jansen. Structure determination of Mg5Si6 particles in Al by dynamic electron diffraction studies. *Science*, 277(5330):1221–1225, 1997.

[39] H. S. Hasting, A. G. Frøseth, S. J. Andersen, R. Vissers, J.C. Walmsley, C. D. Marioara, F. Danoix, W. Lefebvre, and R. Holmestad. Composition of β'' precipitates in Al–Mg–Si alloys by atom probe tomography and first principles calculations. *Journal of Applied Physics*, 106(12):123527, 2009.

[40] Q.G. Wang and C.J. Davidson. Solidification and precipitation behaviour of Al-Si-Mg casting alloys. *Journal of materials science*, 36(3):739–750, 2001.

[41] E. Sjölander and S. Seifeddine. The heat treatment of Al–Si–Cu–Mg casting alloys. *Journal of Materials Processing Technology*, 210(10):1249 – 1259, 2010.

[42] Y.J. Li, S. Brusethaug, and A. Olsen. Influence of Cu on the mechanical properties and precipitation behavior of AlSi7Mg0.5 alloy during aging treatment. *Scripta Materialia*, 54(1):99 – 103, 2006.

[43] G. Wang, Q. Sun, L. Feng, L. Hui, and C. Jing. Influence of Cu content on ageing behavior of AlSiMgCu cast alloys. *Materials Design*, 28(3):1001 – 1005, 2007.

[44] J. A Taylor, D. H St John, J. Barresi, and M. J. Couper. Influence of Mg content on the microstructure and solid solution chemistry of Al-7% Si-Mg casting alloys during solution treatment. In *Materials science forum*, volume 331, pages 277–282. Trans Tech Publ, 2000.

[45] A Samuel, F Samuel, C Ravindran, and S Valtierra. Effect of alloying elements on the segregation and dissolution of CuAl2 phase in Al-Si-Cu 319 alloys. *Journal of Materials Science*, 38(6):1203–1218, 2003.

[46] J. Beddoes. *Principles of metal manufacturing processes*. London, 1999.

[47] F. F. Kraft and J. S. Gunasekera. Conventional Hot Extrusion. In *Metalworking: Bulk Forming*. ASM International, 2005.

[48] P. Saha. Extrusion and Drawing of Aluminum Alloys. In *Aluminum Science and Technology*. ASM International, 2018.

[49] O Reiso. Extrusion of AlMgSi alloys. In *Materials Forum*, volume 28, pages 32–46, 2004.

[50] P. Saha. *Aluminum Extrusion Technology*. ASM International, 2000.

[51] Kumar, Kaushik, Kalita, Hridayjit, Zindani, Divya, Davim, and J. Paulo. *Materials and Manufacturing Processes*. Springer, Cham, 2019.

[52] Manufacturing Guide. Cold rolling of sheets. Available on: `https://www.manufacturingguide.com/en/cold-rolling-sheets`. Retrieved 24-06-2020.

[53] CARES. Manufacturing process routes, 2011. Available on: `https://www.ukcares.com/downloads/guides/PART2.pdf`. Retrieved 23-05-2020.

[54] Standard Norge. NS-EN 10080: Steel for the reinforcement of concrete - weldable reinforcing steel - general, 2005.

[55] Standard Norge. NS 3576-1: Steel for the reinforcement of concrete - dimensions and properties - part 1: ribbed bars B500NA, 2005.

[56] George E. Dieter. Mechanical Behavior Under Tensile and Compressive Loads. In *Mechanical Testing and Evaluation*. ASM International, 2000.

[57] Aluminum : 1 : Properties, physical metallurgy and phase diagrams, 1967.

[58] Vlastimil Bilek, Sabina Bonczková, Jan Hurta, David Pytlík, and Martin Mrovec. Bond strength between reinforcing steel and different types of concrete. *Procedia Engineering*, 190:243 – 247, 2017. Structural and Physical Aspects of Construction Engineering.

[59] L. Bjerregaard, K. Geels, B. Ottesen, and M. Rückert. Metalog guide. 2002. Available on: `https://www.struers.com/-/media/Library/Brochures/English/Metalog-Guide.pdf`.

[60] K. H. Kristiansen. *Characterization of extruded aluminium alloys from ram extrusion and screw extrusion*. NTNU, Trondheim, 2020. unpublished.

[61] L. P. H. Jeurgens, W. G. Sloof, F. D. Tichelaar, and E. J. Mittemeijer. Growth kinetics and mechanisms of aluminum-oxide films formed by thermal oxidation of aluminum. *Journal of Applied Physics*, 92(3):1649–1656, 2002.

[62] J. Zähr, S. Oswald, M. Türpe, H.J. Ullrich, and U. Füssel. Characterisation of oxide and hydroxide layers on technical aluminum materials using XPS. *Vacuum*, 86(9):1216 – 1219, 2012. 5th International Symposium on Vacuumbased Science and Technology SVST5 held at Kaiserslautern, Germany, 28th to 30th September 2010.

[63] J. Goodman. Nikasil® and Alusil. *Engine Professional*, OCT - DES 2008.

A Recycling of Old Engine Block

An old engine block from a Volvo was supposed to be used as feedstock for screw extrusion in this thesis. The year and model of the engine it came from is unknown. It was identified as a Volvo engine block by a small marking on the block, see Figure (A.0.1). A semi-complete motor was supplied by Trondheim Metallco and dissembled at NTNU. The engine as it arrived and after disassembly are shown in Figure (A.0.2) and (A.0.3), respectively. The engine block was washed with a pressure washer and a degreasing agent. The engine block was chosen as it is the largest aluminium component in an engine.

Fig. A.0.1. Volvo logo on engine block

Fig. A.0.2. Engine as it arrived from Trondheim Metallco.

Fig. A.0.3. Disassembled engine. The engine block can be seen in the top right corner.

The engine block feedstock were made in two ways; (1) by machining into chips, and (2) by melt spinning. The chips were machined by Finmekanisk verksted at NTNU, Trondheim. These are shown in Figure (A.0.4). The engine block was not melt-spun, but some material was cast into billets. A billet is shown in Figure (A.0.5). The chemical composition was not analysed, but two discs for analysis was casted.

Fig. A.0.4. Machined engine block chips.

Fig. A.0.5. Engine block billet cast for melt spinning.

B Overview of Material Located at NTNU

The leftover ram extruded material is located in room E-S018 at Bergbygget, NTNU, Trondheim. A summary of the material is given in Table (B.1). 3x120cm profiles of Ø20mm Al-9Si-2Cu is amongst the material, but this was not cooled properly and is therefore not included in the Table. An image of the material is given in Figure (B.0.1). The profiles are sorted by alloy. In addition, each profile/coil is marked with a number that corresponds with the extrusion logs given in Appendix C.

Tab. B.1. Overview of leftover material.

Alloy	Extruded material [m]	Leftover material [m]
Ø10mm		
6082	13.2	7.2
5052	7.2	4.6
Al-9Si-2Cu	3.6	-
Al-9Si-0.3Mg	7.2	2.4
Ø20mm		
6082	~ 85	~ 80
5052	~ 85	~ 80
Al-9Si-2Cu	~ 85	~ 80
Al-9Si-0.3Mg	~ 85	~ 80

Fig. B.0.1. Leftover ram extruded material.

The engine block chips, engine block pieces, and engine block billet are located in room E-S008 at Bergbygget, NTNU, Trondheim. They are in a transparent box. The discs for chemical analysis are there as well.

C Extrusion Logs from SINTEF

The extrusion log provided by SINTEF is given in this section. The extruded material used in this thesis is highlighted, and the associated extrusion graphs (force vs position) are given.

Prosjektnummer / navn :
Container / matrise / bolster: Ø100mm / 10mm stang D5 / vinge
Kommentarer:

Dato: 2020-02-14

Log	Forsøk Nr	Material e	Målte parametre											Kommentarer
			$v_{STEMPEL}$ (mm/s)		ut av T_{BOLT} (°C)			T_{CONT}	T_{STEM}	$T_{BÆREFLATE}$		Kraft (kN)		
			innstilt	ok	ovn	foran	Bak			$T1_{MAX}$	$T2_{MAX}$	Max	Min	
	1	6000	6	6.1	550	502	498	431	~50	-	-	4035	3053	
	2	~	~	6.0	550	503	495	431	~100			3996	2940	
	3	~	~	6.1	551	502	496	431	~180			3996	2897	
	4	5000	3	2.9	415	449	442	431	96	-	-	5708	3663	
	5	~	~	2.9	"	448	441	431	96			5672	3669	
	6	~	~	2.9	"	446	440	431	98			5821	3789	
	7	4000-2	3	2.9	440	466	462	431	129			3682	2780	
	8	~	~	2.9	~	470	463	431	184			3701	2696	
	9	~	2.8	2.7	"	468	461	431	192			3692	2658	
	10	4000-1	1.5	1.4	499	457	451	431	186			4582	3260	Overheat 500
	11	~	1.0	0,9	497	452	447	431	112			4621	3169	
	12	~	1.0	0,9	487	442	433	432	176			4829	3234	Ventet 2-4min for å redusere temp
	13	6000	6	6.1	482	500	496	431	128			3880	2836	
	14	6005-40	6	6.1	"	500	497	431	176			3543	2546	
	15	6060.35	6	6.1	"	497	490	431	136			3171	2479	

Luftsirk 60Hz til ~450 for å redusere
Ind. agg. 482°C

1→3: Ind. agg. 525°C
Luftsirk ovn 500

4000-1 Overhet 500 ned til 450 60Hz
4000-2 Overheat 500, ned til ~450, 60 Hz, luftsirk. ovn 482

SINTEF

Date: 14.02.2002 21:39:55

Exp nr: 10 Ekstrud av 10 mm stang

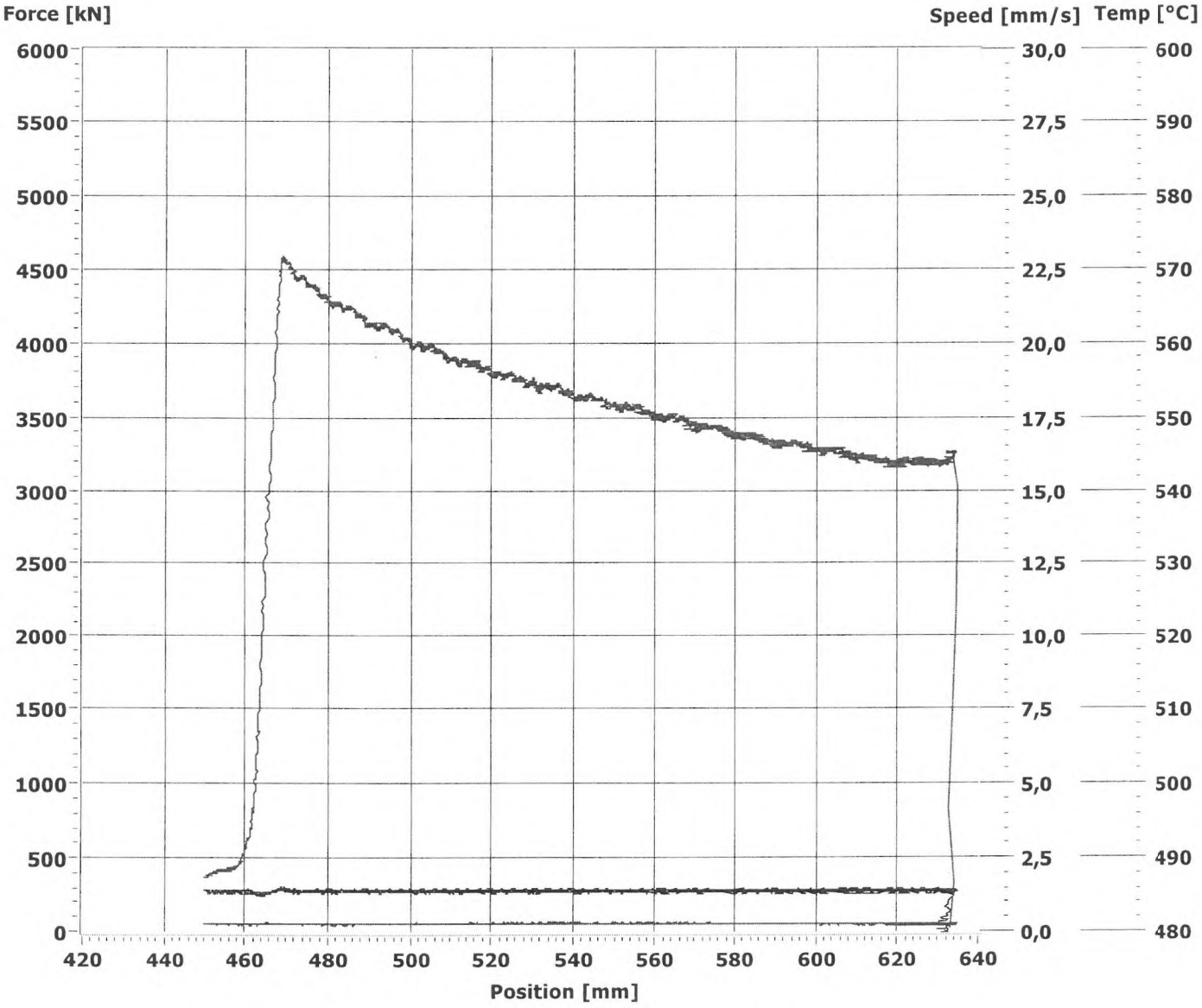

Position [mm]
Force [kN]
Speed [mm/s]
Temp Die [°C]
Temp Container [°C]
Temp 1 [°C]
Temp 2 [°C]
Temp 3 [°C]
Temp 4 [°C]
Temp 5 [°C]
Temp 6 [°C]
Voltage 1 [V]
Voltage 2 [V]
Voltage 3 [V]
Kraft smiverktøy [kN]

Matrix: A11, Ø9mm stang med 2 vinger

Max Force = 4582
Min Force = 3260
Avr Speed = 1,4
Max Temp Die = 481
Max Temp Cont = 432
Max Temp 1 = -90000

SINTEF

Date: 14.02.2002 20:44:00

Exp nr: 8 Ekstrud av 10 mm stang

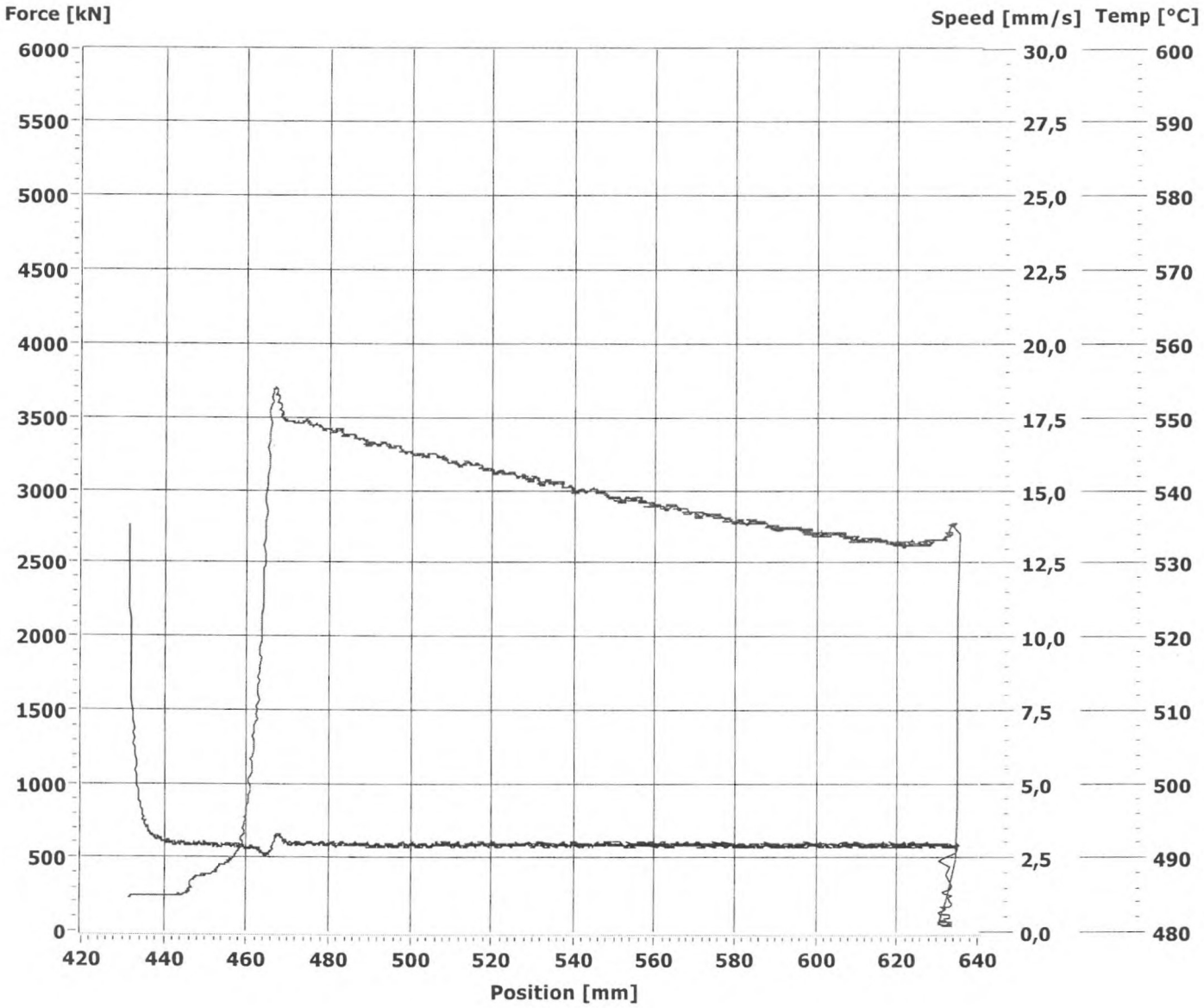

Position [mm]
Force [kN]
Speed [mm/s]
Temp Die [°C]
Temp Container [°C]
Temp 1 [°C]
Temp 2 [°C]
Temp 3 [°C]
Temp 4 [°C]
Temp 5 [°C]
Temp 6 [°C]
Voltage 1 [V]
Voltage 2 [V]
Voltage 3 [V]
Kraft smiverktøy [kN]

Matrix: A11, Ø9mm stang med 2 vinger

Max Force = 3701
Min Force = 2696
Avr Speed = 2,9
Max Temp Die = 478
Max Temp Cont = 432
Max Temp 1 = -90000

SINTEF

Date: 14.02.2002 19:07:47

Exp nr: 4

Ekstrud av 10 mm stang

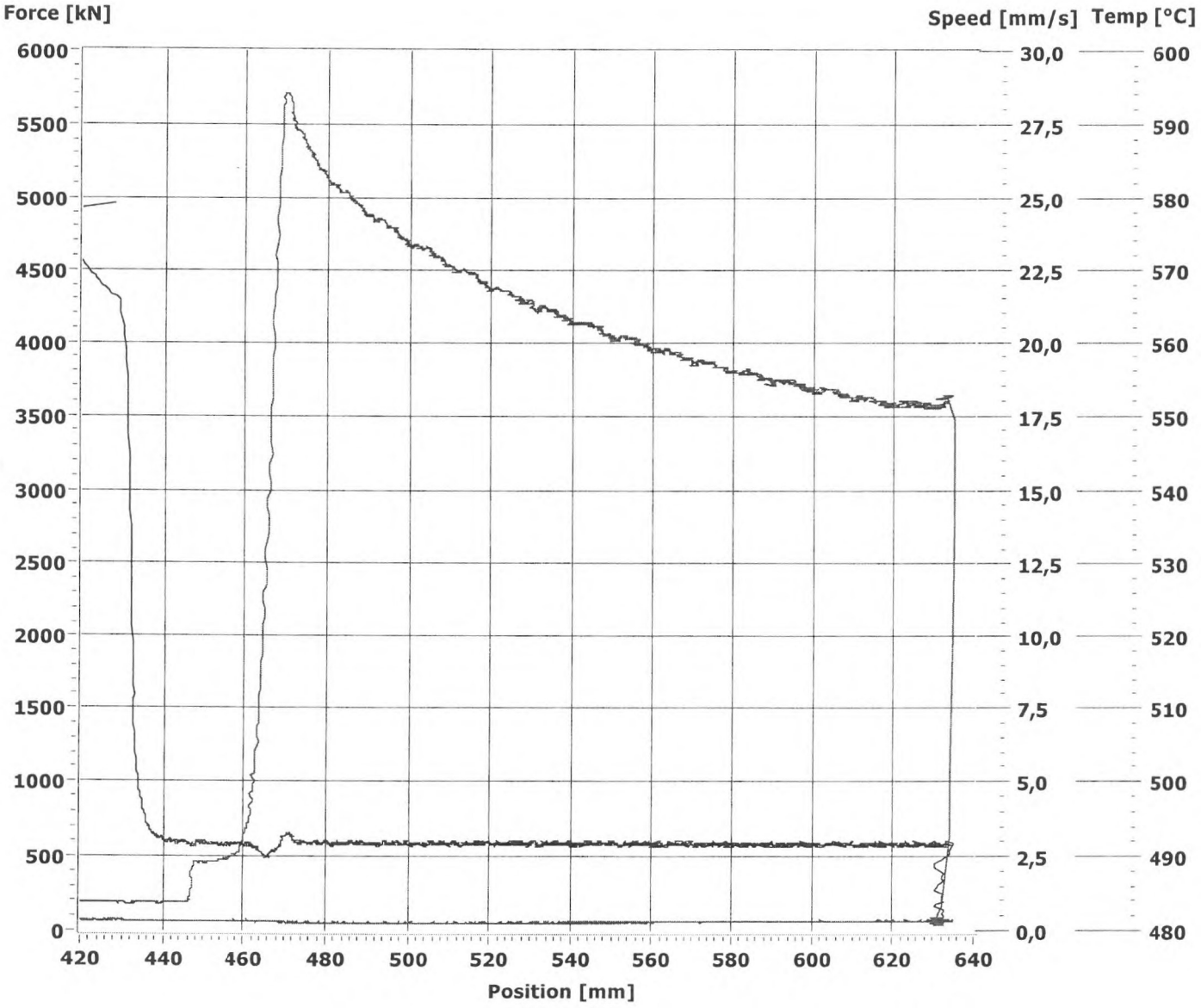

Position [mm]
Force [kN]
Speed [mm/s]
Temp Die [°C]
Temp Container [°C]
Temp 1 [°C]
Temp 2 [°C]
Temp 3 [°C]
Temp 4 [°C]
Temp 5 [°C]
Temp 6 [°C]
Voltage 1 [V]
Voltage 2 [V]
Voltage 3 [V]
Kraft smiverktøy [kN]

Matrix: A11, Ø9mm stang med 2 vinger

Max Force = 5708
Min Force = 3663
Avr Speed = 2,9
Max Temp Die = 481
Max Temp Cont = 432
Max Temp 1 = -90000

SINTEF

Date: 14.02.2002 18:57:24

Exp nr: 3

Ekstrud av 10 mm stang

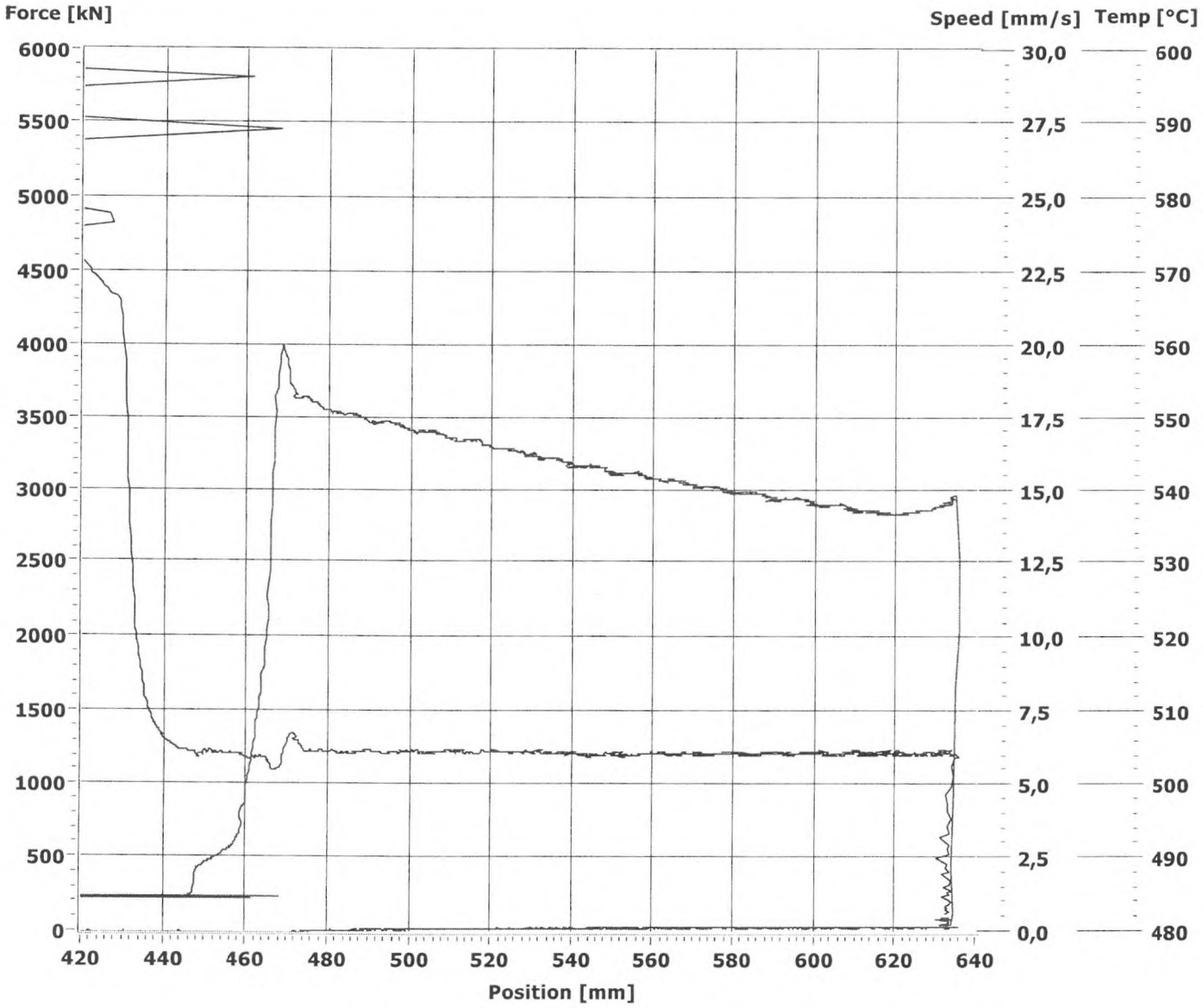

Position [mm]
Force [kN]
Speed [mm/s]
Temp Die [°C]
Temp Container [°C]
Temp 1 [°C]
Temp 2 [°C]
Temp 3 [°C]
Temp 4 [°C]
Temp 5 [°C]
Temp 6 [°C]
Voltage 1 [V]
Voltage 2 [V]
Voltage 3 [V]
Kraft smiverktøy [kN]

Matrix: A11, Ø9mm stang med 2 vinger

Max Force = 3996
Min Force = 2897
Avr Speed = 6,1
Max Temp Die = 481
Max Temp Cont = 432
Max Temp 1 = -90000

Prosjektnummer / navn : xx / Oddvin R → C12H
Container / matrise / bolster: Ø100 mm / 20mm stang / vinge
Kommentarer:

Dato: 2020-02-13

Viktig å presse til 620 mm, dvs. kort prøvestav så den ikke blir mast opp

Log	Forsøk Nr	Material e	Målte parametre											Kommentarer
			$v_{STEMPEL}$ (mm/s)		ut av T_{BOLT} (°C)			T_{CONT}	T_{STEM}	$T_{BÆREFLATE}$		Kraft (kN)		
			innstilt	ok	ovn	foran	Bak			$T1_{MAX}$	$T2_{MAX}$	Max	Min	
1		6xxx	3	2.9	490	510	509	429	~50	–	–	2866	–	Plugging i tør manuelt
2		6xxx	3	"	"	515	510	429	~50					luftkjølinge
3		6xxx	3	2.9	"	512	509	386	~50			3210	2384	o.k. luftkjøling
4		"	3	2.9	"	510	508	398	"			3041	2233	delvis vannkjøling foran
5		"	3	2.9	545	508	500	406	~50			3086	2175	Overheting 64Hz
6		5xxx	3	2.9	415	442	440	408	~50			4695	2729	
7		"	3	2,9	415	441	439	408	~100			4937	2687	
8		"	3	2.9	415	442	441	411	~100			4923	2836	
9		4xxx 2	3	3.2	452	481	477	413	~120			3151	2052	
10		"	3	3.2	"	482	476	415	90			2897	2072	
11		"	3	3.3	"	479	473	418	96			2917	2045	
12		4xxx-1	3	4.6	496	450	447	422	126			4152	2536	Overheting ind ovn 500°C
13		"	3	4.7	498	454	445	423	186			4203	2549	" bjeler 60Hz
14		"	2	4.9	492	446	438	426	115			4275	2547	"

18.00

fo 1 : varmet direkte innstilt 490°C på ind. ovn
fo 1 plugging ved entring av bjeleror
fo 2: plugging som over, stoppet & tok ut bjeleror, kunne da presse ut profilet, buppet i bjeller

SINTEF

Date: 14.02.2002 03:42:57

Exp nr: 14 Ekstrud av 20 mm stang

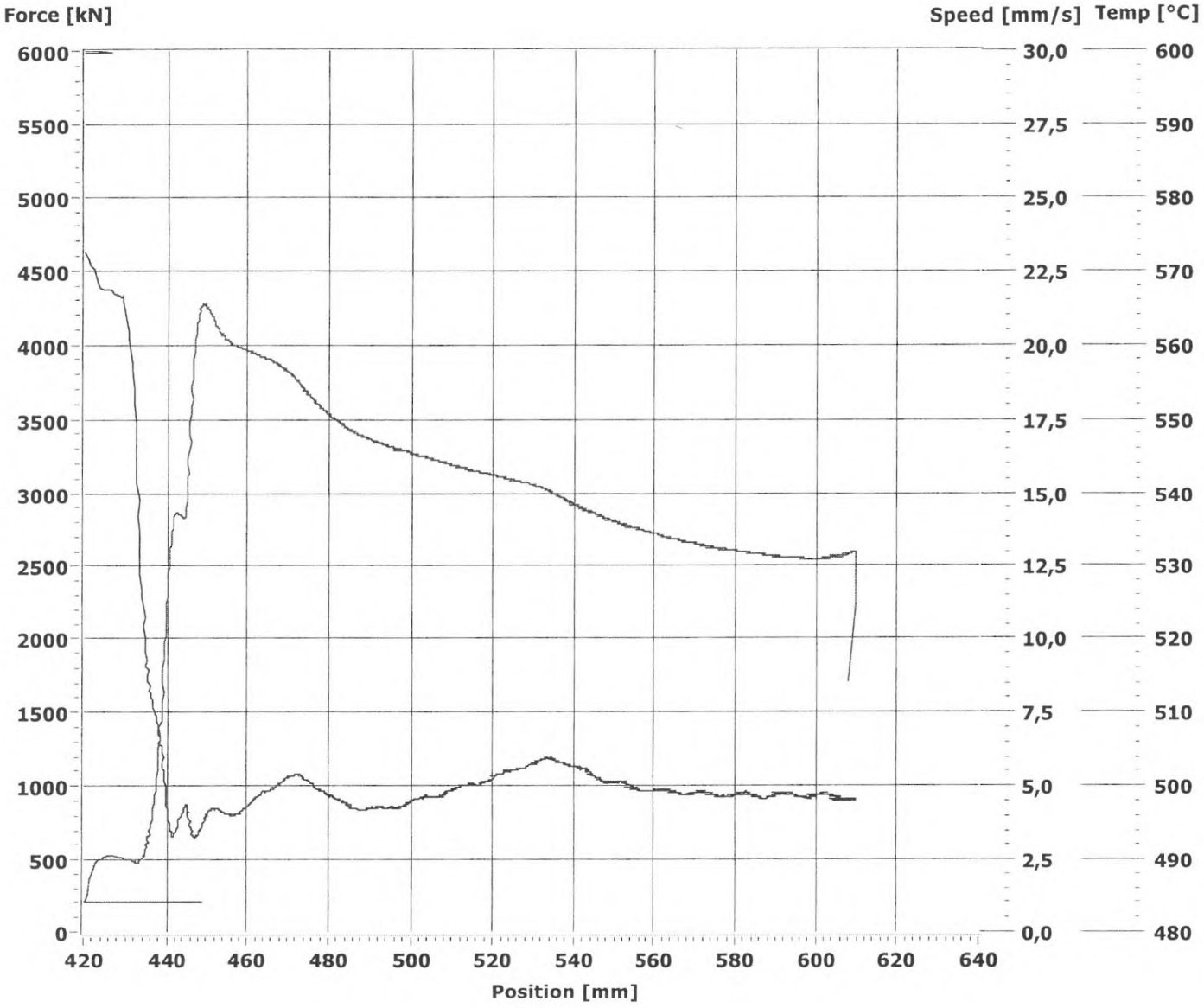

Position [mm]
Force [kN]
Speed [mm/s]
Temp Die [°C]
Temp Container [°C]
Temp 1 [°C]
Temp 2 [°C]
Temp 3 [°C]
Temp 4 [°C]
Temp 5 [°C]
Temp 6 [°C]
Voltage 1 [V]
Voltage 2 [V]
Voltage 3 [V]
Kraft smiverktøy [kN]

Matrix: A11, Ø9mm stang med 2 vinger

Max Force = 4275
Min Force = 2547
Avr Speed = 4,9
Max Temp Die = 466
Max Temp Cont = 426
Max Temp 1 = -90000

SINTEF

Date: 14.02.2002 02:47:54

Exp nr: 11 Ekstrud av 20 mm stang

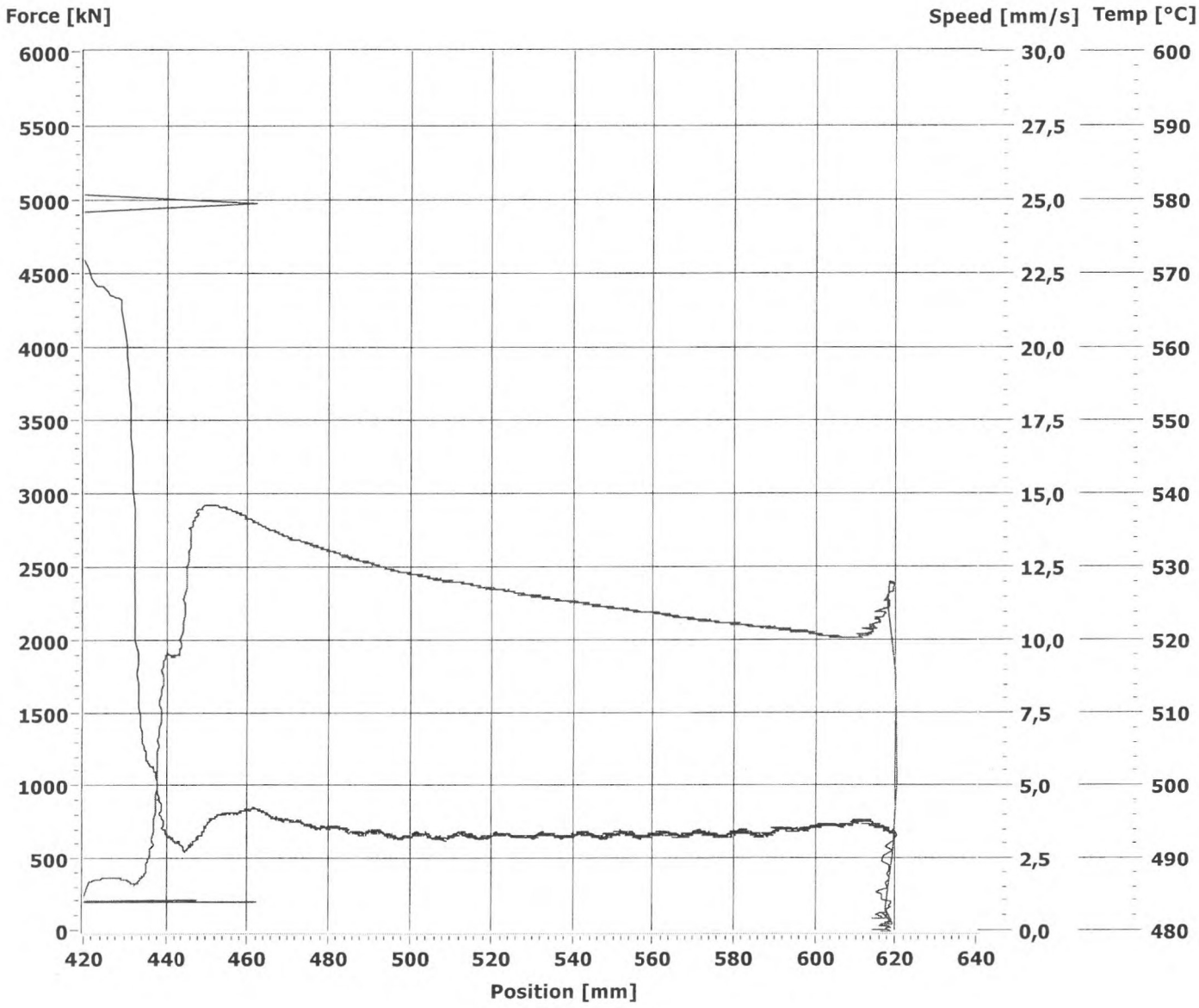

Position [mm]
Force [kN]
Speed [mm/s]
Temp Die [°C]
Temp Container [°C]
Temp 1 [°C]
Temp 2 [°C]
Temp 3 [°C]
Temp 4 [°C]
Temp 5 [°C]
Temp 6 [°C]
Voltage 1 [V]
Voltage 2 [V]
Voltage 3 [V]
Kraft smiverktøy [kN]

Matrix: A11, Ø9mm stang med 2 vinger

Max Force = 2917
Min Force = 2045
Avr Speed = 3,3
Max Temp Die = 460
Max Temp Cont = 417
Max Temp 1 = -90000

SINTEF

Date: 14.02.2002 02:10:32

Exp nr: 8 Ekstrud av 20 mm stang

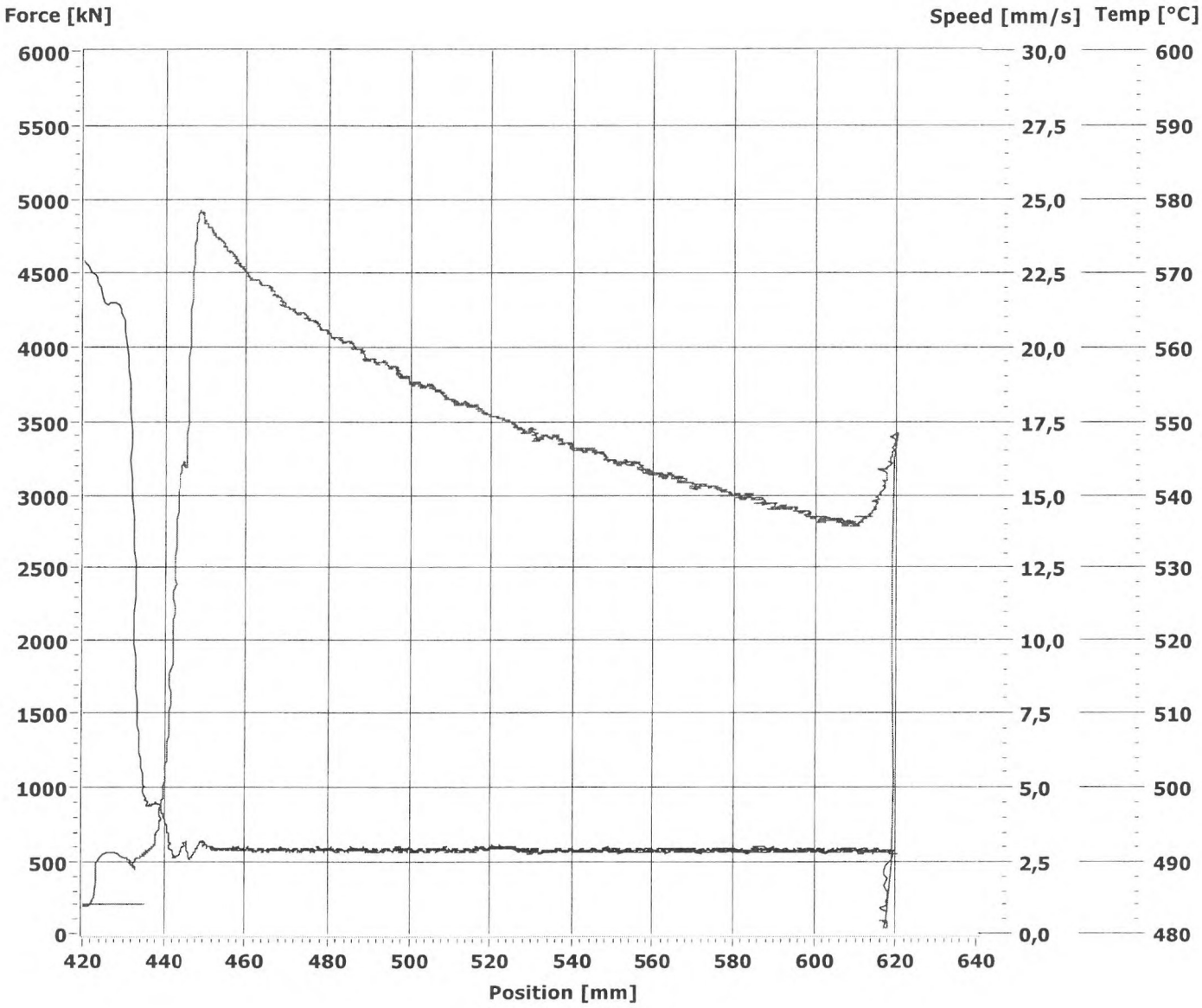

Position [mm]
Force [kN]
Speed [mm/s]
Temp Die [°C]
Temp Container [°C]
Temp 1 [°C]
Temp 2 [°C]
Temp 3 [°C]
Temp 4 [°C]
Temp 5 [°C]
Temp 6 [°C]
Voltage 1 [V]
Voltage 2 [V]
Voltage 3 [V]
Kraft smiverktøy [kN]

Matrix: A11, Ø9mm stang med 2 vinger

Max Force = 4923
Min Force = 2838
Avr Speed = 2,9
Max Temp Die = 458
Max Temp Cont = 411
Max Temp 1 = -90000

SINTEF

Date: 14.02.2002 01:40:21

Exp nr: 5 Ekstrud av 20 mm stang

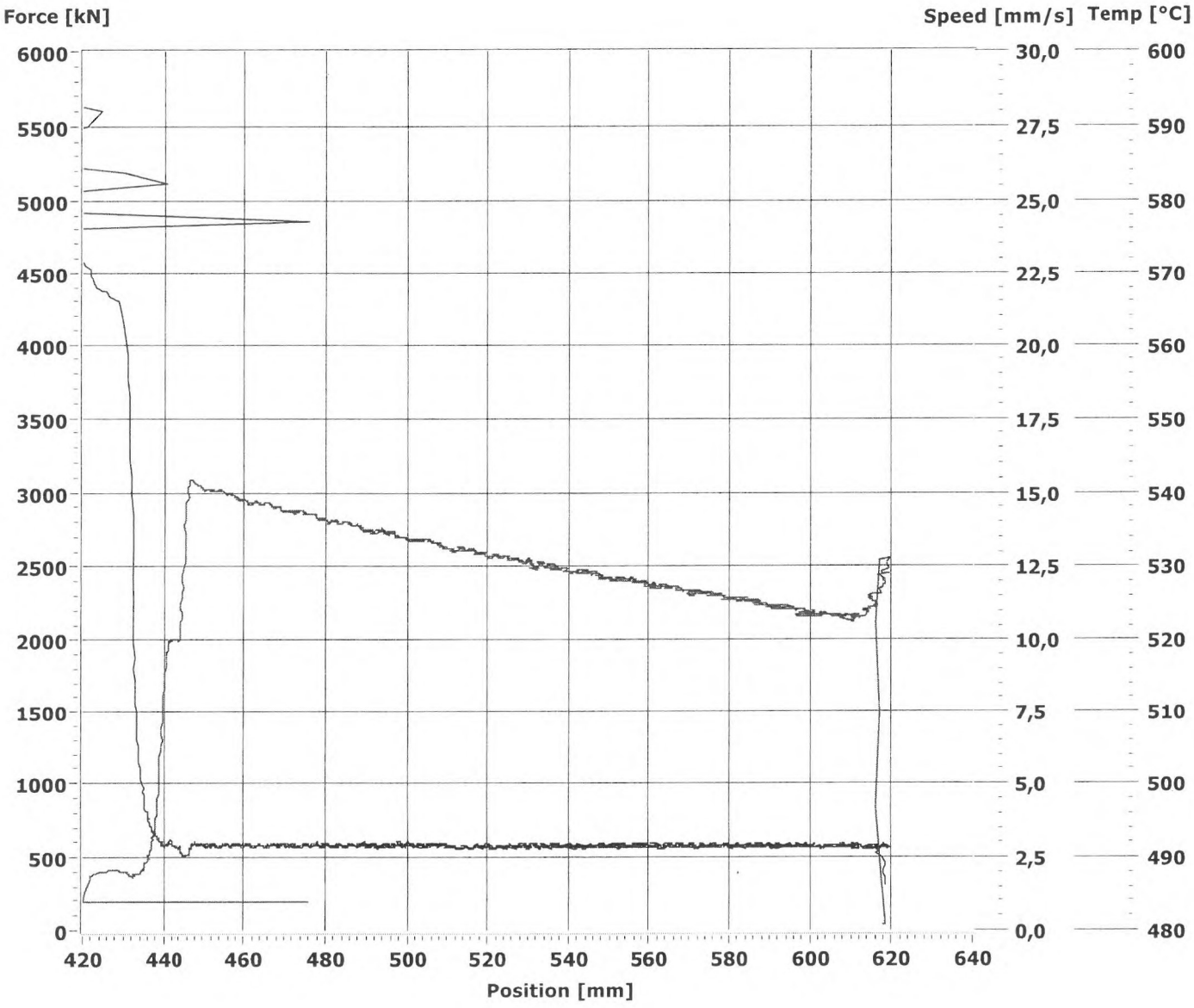

Position [mm]
Force [kN]
Speed [mm/s]
Temp Die [°C]
Temp Container [°C]
Temp 1 [°C]
Temp 2 [°C]
Temp 3 [°C]
Temp 4 [°C]
Temp 5 [°C]
Temp 6 [°C]
Voltage 1 [V]
Voltage 2 [V]
Voltage 3 [V]
Kraft smiverktøy [kN]

Matrix: A11, Ø9mm stang med 2 vinger

Max Force = 3086
Min Force = 2175
Avr Speed = 2,9
Max Temp Die = 450
Max Temp Cont = 406
Max Temp 1 = -90000

D Images from Simulation of Rolling Process Conducted by SINTEF

In this appendix, images from simulations of the rollings process conducted by SINTEF is provided. The images were supplied by Rune Østhus at SINTEF through e-mail correspondence.

Ø10mm

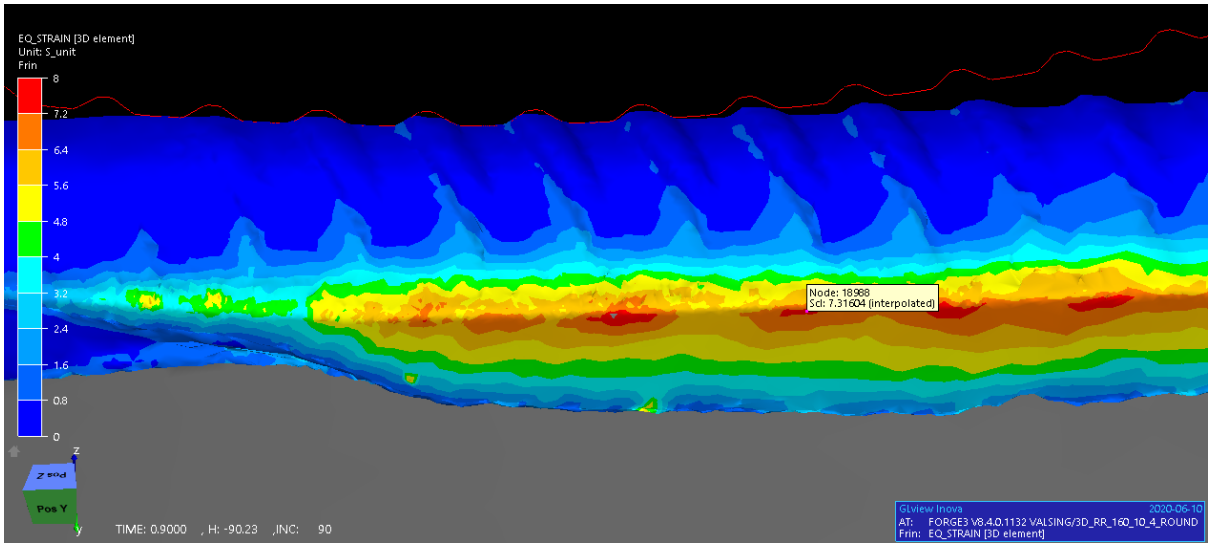

Fig. D.0.1. Simulated strain on the outside of the Ø10mm profile. Scale: 0% to 800% strain.

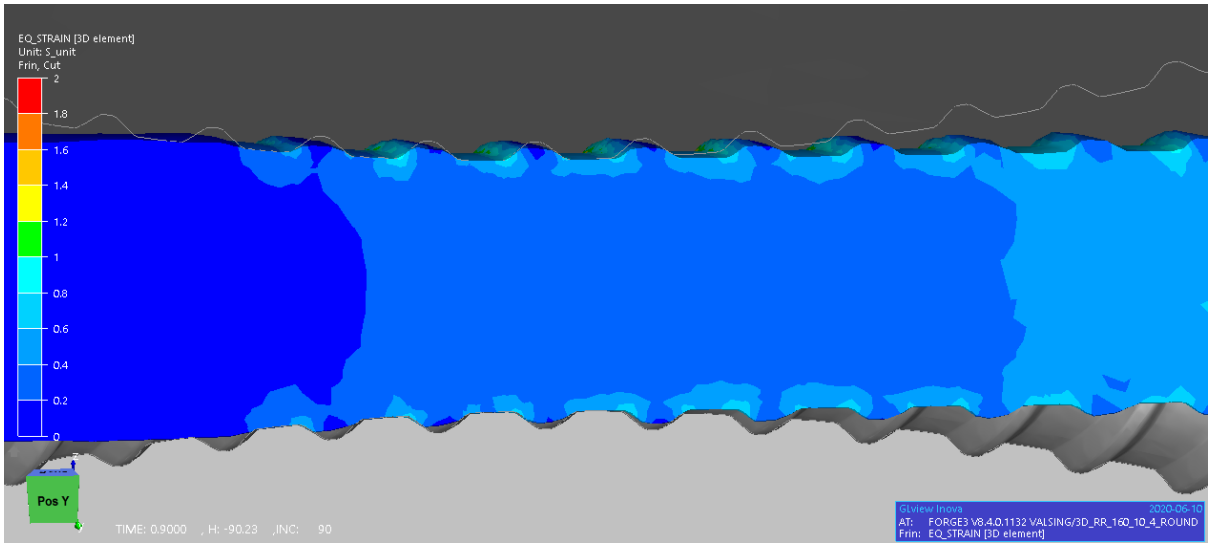

Fig. D.0.2. Simulated strain on the longitudinal cross-section of the Ø10mm profile. Scale: 0% to 200% strain.

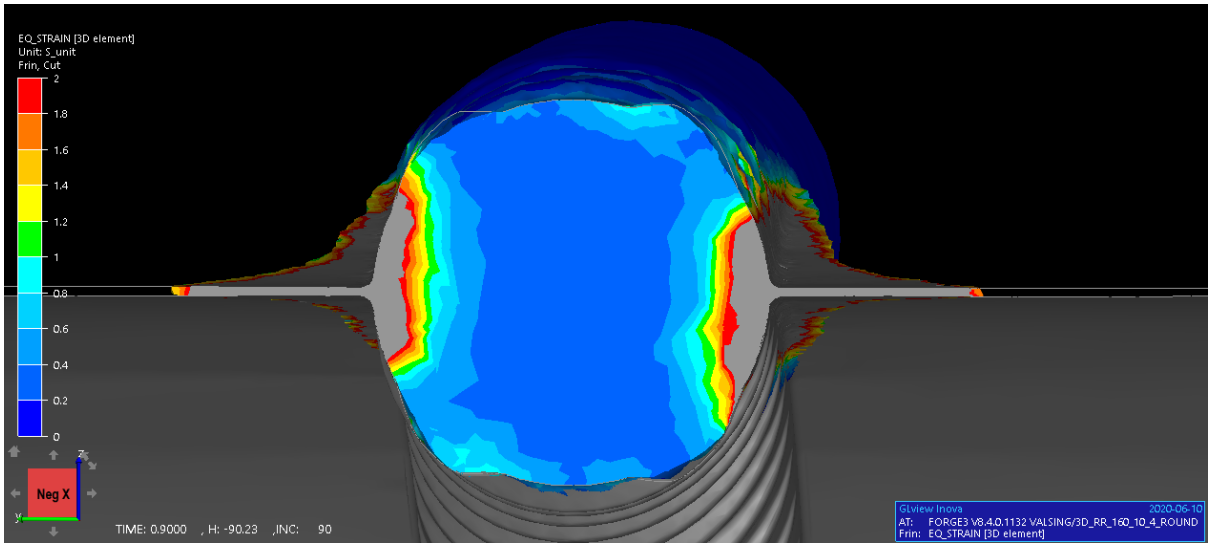

Fig. D.0.3. Simulated strain on the transverse cross-section of the Ø10mm profile. Scale: 0% to 200% strain.

Ø20mm

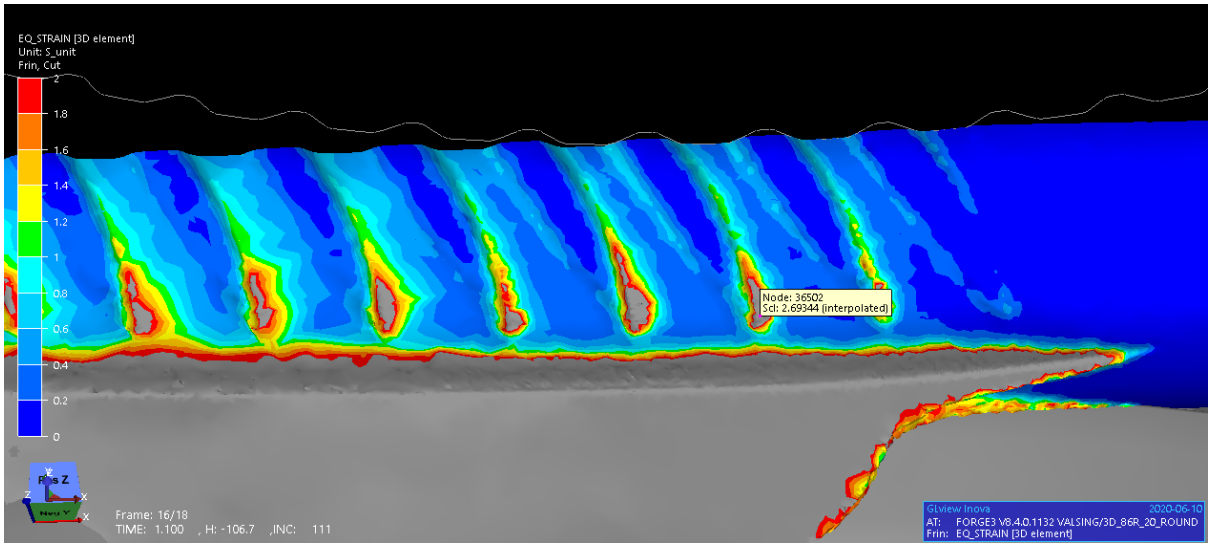

Fig. D.0.4. Simulated strain on the outside of the Ø20mm profile. Scale: 0% to 200% strain.

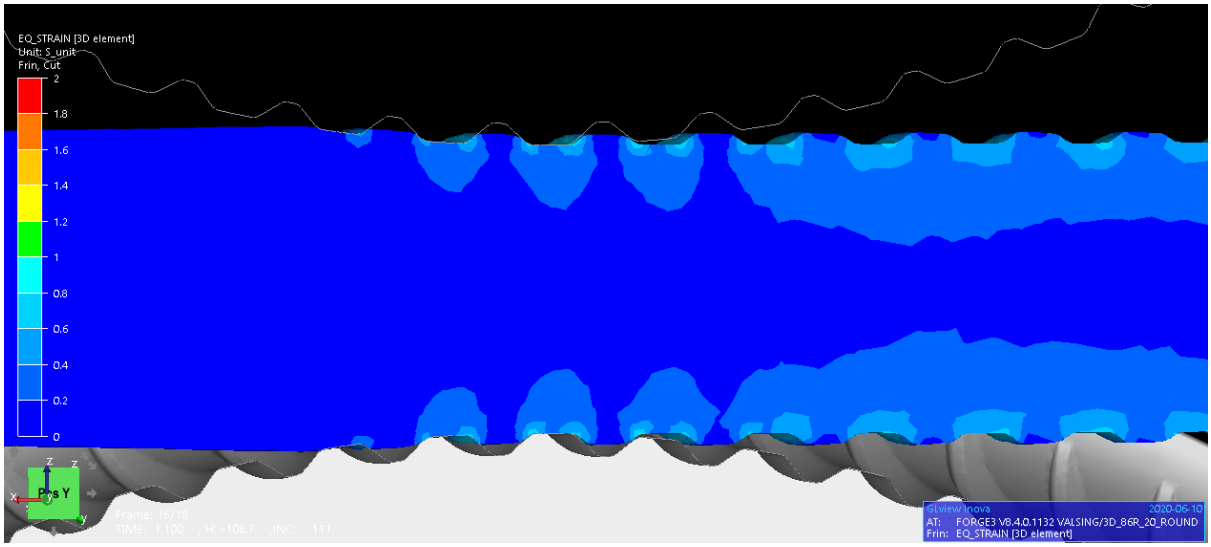

Fig. D.0.5. Simulated strain on the longitudinal cross-section of the Ø20mm profile. Scale: 0% to 200% strain.

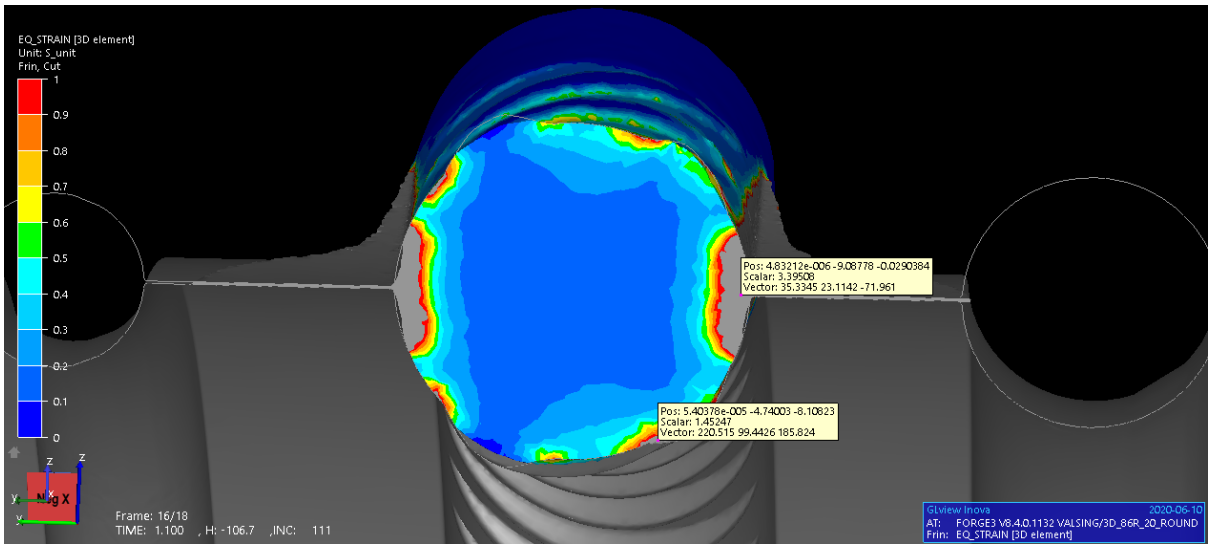

Fig. D.0.6. Simulated strain on the transverse cross-section of the Ø20mm profile. Scale: 1% to 100% strain.

E Hardness Profile of Rolled Profiles

The hardness profiles of the transverse and longitudinal cross-section of the Ø10mm and Ø20mm rolled profiles are given in Figure (E.0.1) - Figure (E.0.4).

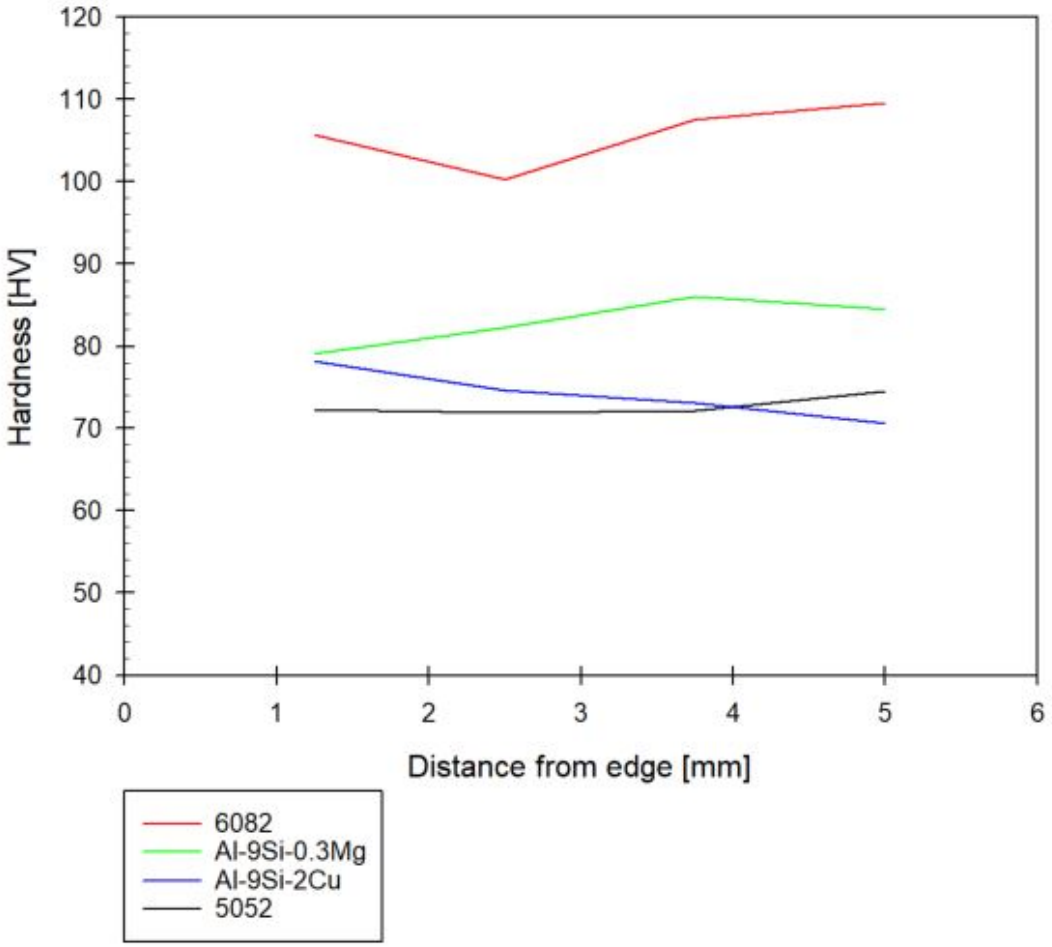

Fig. E.0.1. Hardness profile of rolled Ø10mm longitudinal cross-sections.

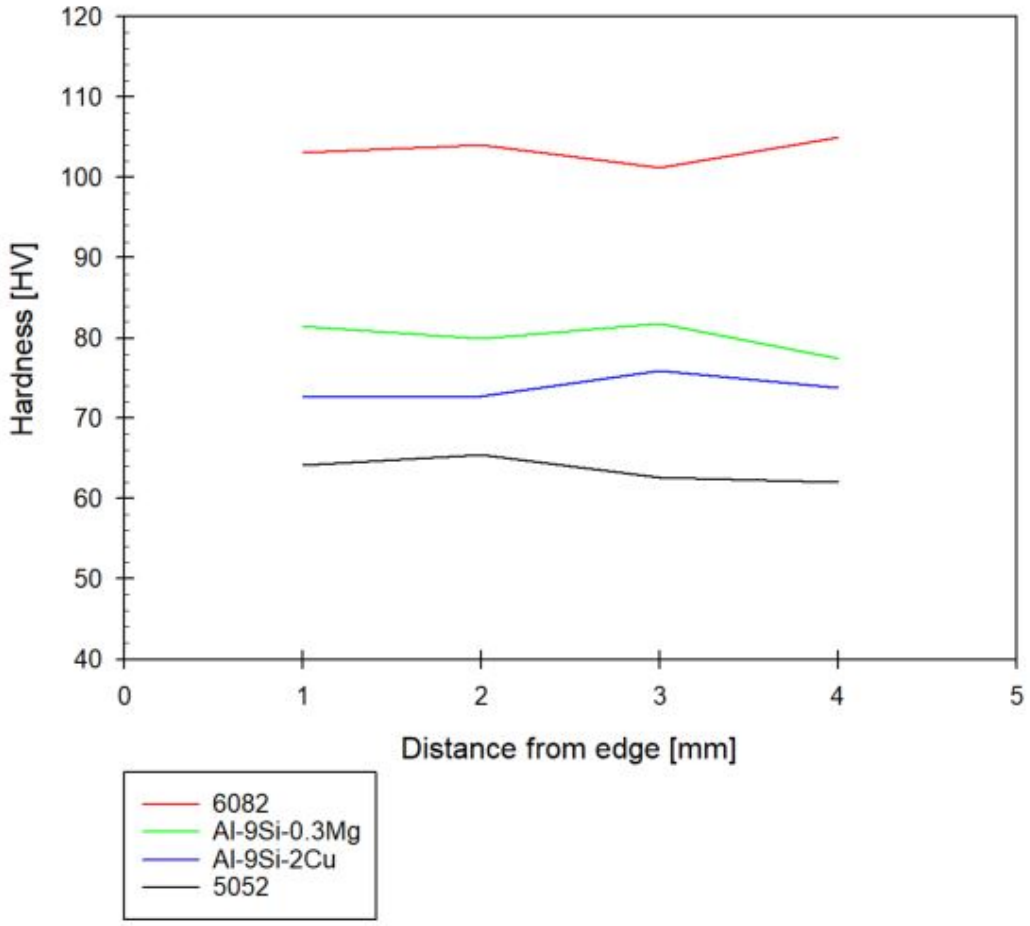

Fig. E.0.2. Hardness profile of rolled Ø10mm transverse cross-sections.

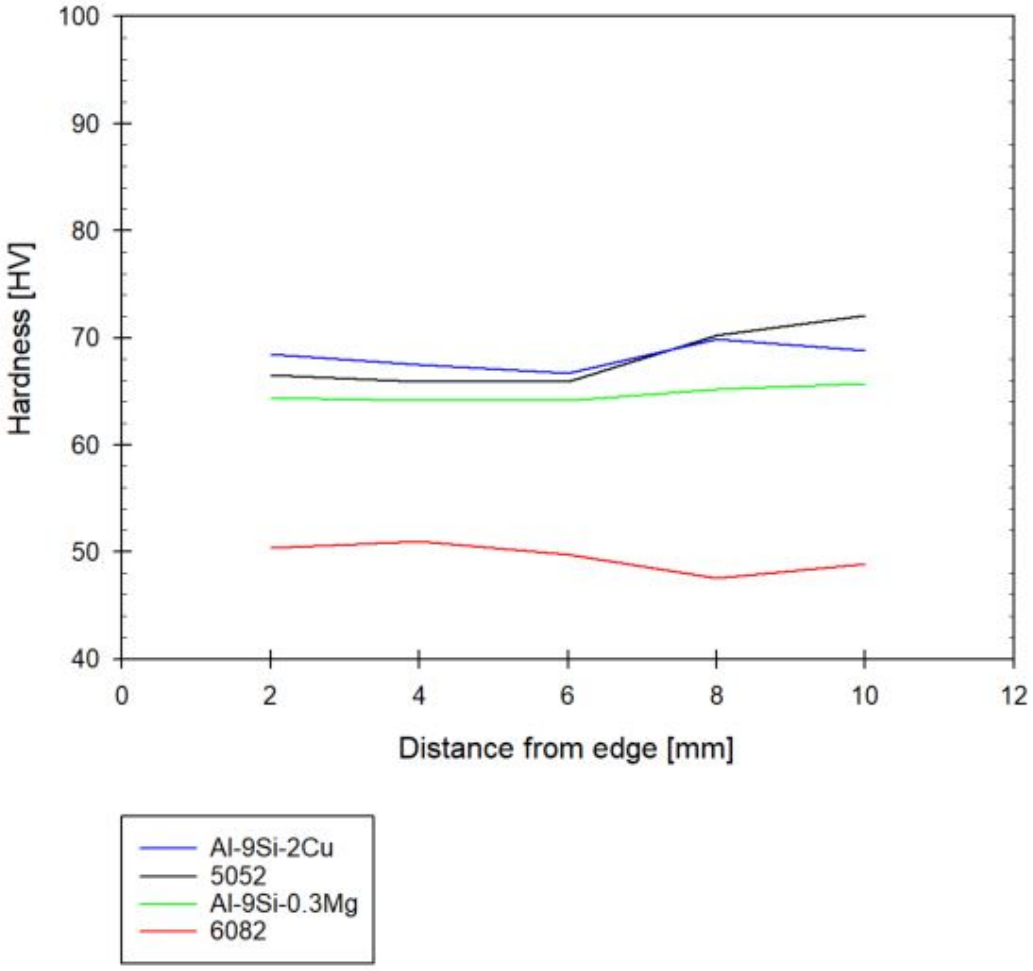

Fig. E.0.3. Hardness profile of rolled Ø20mm longitudinal cross-sections.

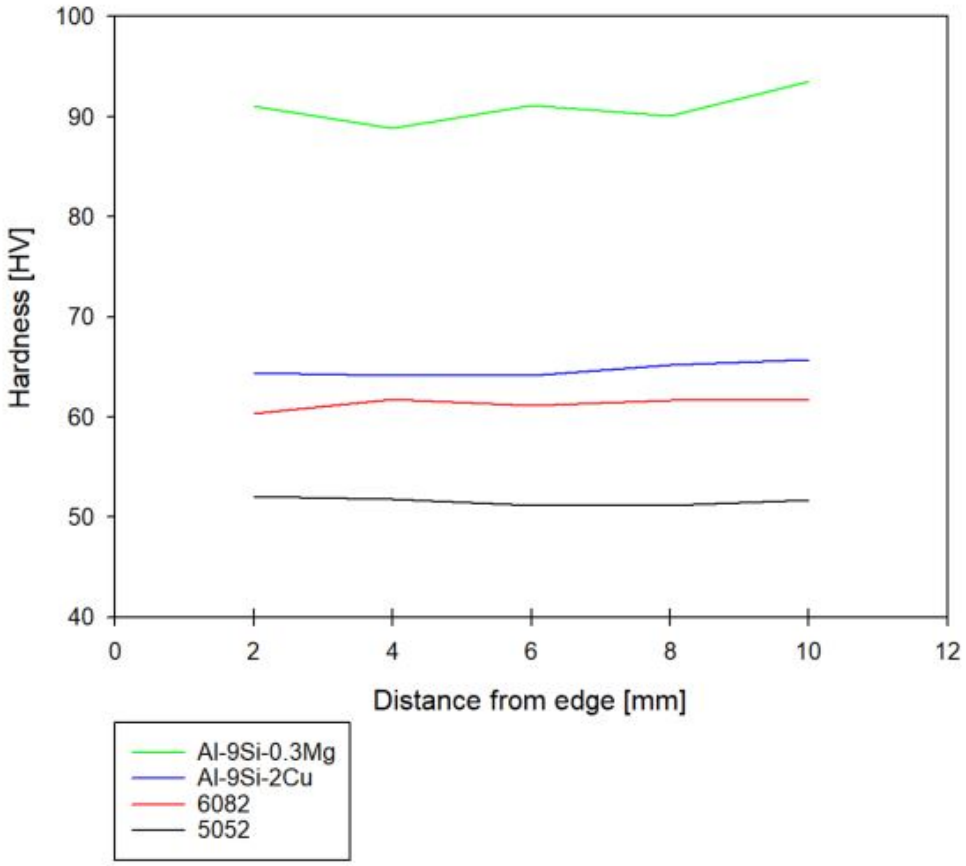

Fig. E.0.4. Hardness profile of rolled Ø20mm transverse cross-sections.

Moa Madeleine Fagermo

The Use Of Aluminium in Sustainable Concrete Structures

NTNU
Norwegian University of
Science and Technology